

ABSTRACT

Title of dissertation: DETAILED PIV MEASUREMENTS ON
PARTICLE-TURBULENCE INTERACTION IN
OSCILLATORY SHEET FLOW: IN DILUTE REGIME

Chang Liu
Doctor of Philosophy, 2022

Dissertation directed by: Dr. Kenneth Kiger
Department of Mechanical Engineering

An experimental investigation of sediment transport mechanisms under oscillatory sheet flow condition is conducted. Focus is placed upon the dilute regime of solid-liquid transport with volume concentrations $C \leq 0.01$, where significant fluid turbulence is present, strong particle-turbulence interaction occurs and inter-particle collisions can be neglected. Understanding the coupling dynamics between phases is critical for the validation and improve of the existing numerical models. Simultaneous determination of the dynamics of each phase is often prohibitively expensive to acquire by direct numerical simulation and poses significant challenges to experimental measurements. In our experiment, a U-shaped water tunnel is used to create highly repeatable oscillatory sheet flow conditions over a mobile bed. The test section of the tunnel is 375 cm in length, with a cross-sectional area of $30 \times 45\text{ cm}^2$. The sediment is modeled using narrowly sorted spherical soda lime glass beads with a mean diameter of $d = 240\ \mu\text{m}$ and a specific gravity of $s = 2.5$.

The efforts have been made in two directions: the measurement technique

development and the application of the developed technique to an oscillatory sheet flow. First, a novel measurement technique, based upon Particle Image Velocimetry (PIV), was developed and validated, that aims for a simultaneous measurement of both phases. For the sediment phase measurement, the multi-camera single-plane (MCSP) method was developed to reconstruct particle's instantaneous 3D positions towards a higher concentration. This was followed by Lagrangian particle tracking (LPT) to link the reconstructed particles over successive frames, with an in-house developed algorithm based upon shake-the-box (STB, Schanz et al. [1]). For the carrier phase measurement, stereoscopic PIV (SPIV) was implemented. In order to reduce the cross-talk errors due to the presence of sediment particles, the apertured filter method was developed to produce adequate image quality of both phases allowing for a reliable extraction of each phase independently.

Second, the developed measurement technique was applied in a sinusoidal oscillatory sheet flow (period, $T = 5\text{ s}$, and peak free stream velocity, $U_{o,p} = 1\text{ m/s}$) to provide a whole field, phase-locked time-resolved, particle-resolved and concurrent measurement of both the fluid and the sediment phase in the dilute regime ($C \leq 0.01$). Such detailed measurements in sheet flow have never been reported before to the author's best knowledge. The analysis of the acquired data focused upon three phase angles when the external flow is reversing the direction. It has been found that during flow reversal, 1) distinct particle suspension mechanisms are identified in the upper dilute regime ($y > 11\text{ mm}$) and the lower dilute regime ($2 < y < 4\text{ mm}$), where y represents the vertical distance from the static sediment bed; 2) sediment particles show strong preferential sampling in flow regions with ejection events (Q2)

and high turbulent fluctuations for $y > 11 \text{ mm}$, while the over-sampling diminishes towards the bed; and 3) the particle velocity and their ambient fluid velocity show a strong correlation for $y > 11 \text{ mm}$ and the correlation becomes weaker as approaching the bed.

DETAILED PIV MEASUREMENTS ON
TURBULENCE-PARTICLE INTERACTION
IN OSCILLATORY SHEET FLOW: IN DILUTE REGIME

by

Chang Liu

Dissertation submitted to the Faculty of the Graduate School of the
University of Maryland, College Park in partial fulfillment
of the requirements for the degree of
Doctor of Philosophy
2022

Advisory Committee:
Professor Kenneth Kiger, Chair/Advisor
Professor James Duncan
Professor Johan Larsson
Professor Amir Riaz
Professor James Baeder

© Copyright by
Chang Liu
2022

Chapter 1: Introduction

1.1 Motivation of sediment transport

Multiphase flow has remained one of the most interesting and challenging problems in fluid mechanics due to its ubiquity and complexity in nature. Multiphase flow problems (especially dispersed flow) are encountered in many industrial applications, such as heat exchangers, spray drying, pollution control, fluidized beds, manufacturing and material processing, rocket propulsion and many more. They are also frequently confronted in geophysical phenomena, such as sediment transport, soil erosion, physics of clouds etc. and biological systems, such as respiratory and blood flow. In general, the source of complexity can originate from many aspects, for instance the mass, momentum and energy transfer among different phases, the inhomogeneity of the concentration of the dispersed phase, turbulence, new length scales introduced at the scale of the particles, surface tension effects, the transition of flow regimes and so on. The scope of this thesis concerns only liquid-solid sediment transport, which limits the phases to only sand and water, instantly eliminating many of the complexities listed above. Even with this constraint on the parameters, there exists a significant lack of understanding on the coupled behavior of phases that hinders the existence of a comprehensive model capable of accurately

describing the phenomena.

Sediment transport is one of the main issues pertinent to coastal and fluvial management. According to the United Nations, approximately 44% of the global population lives within 150 *km* of the coast (<http://www.oceansatlas.org/subtopic/en/c/114/>, 2010), with a continually increasing trend of greater coastal density over the past several decades. Appropriate development and maintenance of coastal social infrastructure requires an ability to accurately predict coastal morphology evolution due to both erosion and deposition of sediment. Important problems such as sand eroding, expedited due to the rise of sea level, and bed form evolution can potentially affect the environment and ecology in the coastal zones. Another example that motivates the study of sediment transport is related to the phenomena turbidity currents (Meiburg and Kneller [2]), defined as particle-laden, gravity-driven underflows in which the particles are largely or wholly suspended by fluid turbulence. They are characterized by their ability to transport a large amount of sediment over long distances, ranging from a few hundreds of meters to thousands of kilometers along the ocean floor. They not only play a significant role in the global sediment cycle, triggering the formation of submarine canyons and hydrocarbon deposits, but also are capable of causing the destruction of seafloor equipment and instrumentation. The benthic boundary layer between the turbidity current and the outer turbulent flow plays a key role in determining both the suspension of sediment into the bulk flow, as well as determining the effective drag, and hence is a key factor in predicting their evolution.

In nature, sediment transport can be very complicated due to the complex the

bottom boundary layer flow that is caused by waves, currents and their associated turbulence, in conjunction with the diversity of the sand particle properties, such as density, size and shape. Even under well controlled laboratory flow conditions, it has still proved to be very challenging to accurately model the sediment transport process. The difficulty lies in the strongly coupled particle-turbulence interaction and inter-particle interaction occurring in a wide range of volume concentrations (denoted by C or ϕ_v interchangeably) varying from $\phi_v \approx 0.6$ (random close packing) to $\phi_v < 10^{-5}$ in dilute regime. The mechanisms of particle-turbulence interaction and inter-particle interaction are diverse over this nearly five orders of magnitude. In moderate to high concentrations, the transport is dominated by inter-particle interactions, ranging from intermittent collisions to enduring contacts; while as the particle concentration decreases, the motions of the particles become increasingly dominated by the turbulent eddies and inversely the eddies are also strongly modulated by the presence of the particles.

1.2 Dimensionless numbers in sediment transport

Sediment transport in general is an extremely broad and complicated topic due to the wide range of bottom boundary flow conditions and sediment properties ubiquitously encountered in nature. Early studies on sediment transport relied heavily on empirical observations and dimensional analysis in order to categorize different sediment transport regimes and formulate sediment transport rate models. In this section, some dimensionless numbers frequently referenced in sediment

transport literature are reviewed and their physical meanings are explained. The dimensionless numbers presented below are formulated under significantly simplified assumptions, where the transport of non-cohesive mono-dispersed spherical particles are considered under conditions of steady or periodic, homogeneous and fully developed flow. More complicated flow conditions or sediment properties are beyond the scope of this thesis, thus will not be discussed.

In steady flows, there are three dimensionless parameters most widely used to parametrize the transport processes: 1) the specific gravity of sediment particles, defined as $s = \rho_s/\rho_f$, with ρ_s and ρ_f being the mass density of the sediment material and the fluid respectively; 2) the Shields parameter, which is expressed as:

$$\theta = \frac{u_\tau^2}{(s-1)gD_{50}} = \frac{\tau_b}{\rho_f(s-1)gD_{50}} \quad (1.1)$$

where τ_b represents the bed shear stress, $u_\tau = \sqrt{\tau_b/\rho_f}$ is the friction velocity, $g = 9.8m/s^2$ denotes the gravitational force, and D_{50} is the median sediment diameter for poly-dispersed particles; and 3) the particle Reynolds number defined by the friction velocity, written as $Re_p = u_\tau D_{50}/\nu$, where ν is the molecular kinematic viscosity of the fluid. The fall parameter, R_p , represents a dependent fourth parameter that can be expressed as a combination of the Shields parameter and the particle Reynolds number:

$$R_p = \frac{Re_p}{\sqrt{\theta}} = \frac{D_{50}\sqrt{(s-1)gD_{50}}}{\nu}, \quad (1.2)$$

This parameter is frequently adopted due to its independence of the friction velocity

and can be easily evaluated.

Several sediment transport modes and bed form regimes under steady flow can be identified on a plot of R_p as a function of θ , as shown in Figure 1.1 (Amoudry [3]). The shields parameter, θ , represents the ratio of the bed shear stress exerted on the sediment particles ($\tau_b D_{50}^2$) to their submerged weight ($\rho_f (s - 1) g D_{50}^3$). It characterizes the strength of the flow in the bottom boundary layer and is the dominating parameter when predicting the incipient motion of sediment particles and the formation of various bed forms. Figure 1.1 shows that different bed forms are generated under different flow intensities. When θ is smaller than some critical values (mildly depending upon R_p), the flow in the bottom boundary layer is too weak to induce sediment motion; when θ is increased while keeping $\theta < 0.8$, small vortex ripples (2D or 3D) can form on the bed; while when $\theta > 0.8$, the flow becomes strong enough to wash off the small ripples resulting in a dense moving granular flow and a flat bed surface (“sheet flow”). The particle Reynolds number, Re_τ , accounts for the effect of fluid viscosity on the sediment transport, which is an important parameter when studying sediment suspensions by turbulent eddies.

The mobilized sediment particles can be further distinguished according to two different types of transport mechanisms: the bed load and the suspended load, as shown in Figure 1.1. The bed load often occurs within a few millimeters above the immobile sediment layer and is characterized by the hopping, rolling and sliding motions occurred with sediment particles. The concentration within the bed load layer typically varies from close-packed sediment concentration ($\sim 60\%$) down to 10% and the particle’s motion is dominated by the inter-particle friction and col-

lision forces. As the flow becomes stronger and the vertical velocity of turbulent eddies (approximated by u_τ) exceeds the sediment particles fall velocity, W_s , some of the sediment particles can be entrained in the water column and transported by the turbulent flow over much longer distances as suspended load before returning to the bed. Within the suspended load layer (from several millimeters to several centimeters above the immobile sediment layer), strong particle-turbulence interactions are anticipated and the inter-particle collisions can be often neglected. In most sediment transport, the two transport mechanism coexist and a sharp interface between the two transport layers cannot be clearly defined.

In oscillatory (periodic) flows, an additional parameter is introduced to account for the acceleration in the external flow, which is known as the Sleath parameter:

$$S = \frac{U_{o,p}\omega}{(s-1)g} \quad (1.3)$$

The Sleath parameter can be viewed as a relative measure of the pressure gradient in comparison to the gravitational force. In Equation 1.3, $U_{o,p}$ is the amplitude of the oscillatory free stream velocity and ω is the angular frequency. Large values of the Sleath parameter can induce instabilities in the near-bed transport layer, which can lead to intermittent bed failure or plug flow, resulting in increases of erosion depth, billows of sediment being suspended and an overall large sediment transport rate. Cheng et al. [4] found that the criterion for the onset of momentary bed failure in oscillatory sheet flow is a function of both the Shields parameter and Sleath parameter according to the multi-dimensional Eulerian two-phase model

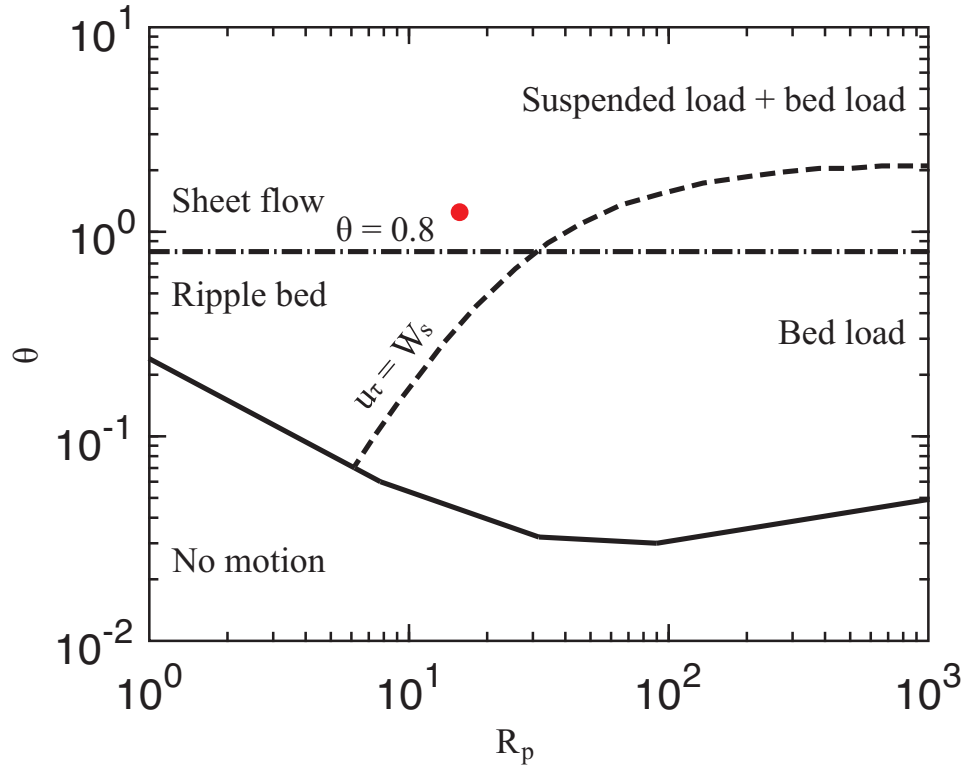


Figure 1.1: Different sediment transport regimes, demarcated by the threshold for different transport modes and bed form regimes. The red dot represents the Shields parameter, θ , and the fall parameter, R_p , computed with our experimental condition during peak flow.

(SedFoam) the author developed.

In addition to classifying sediment transport regimes, the above non-dimensional parameters can also be used to empirically model the sediment transport rate through parameterization especially within the bed load layer for steady flows (Meyer-Peter and Müller [5], Wilson [6]) and for oscillatory flows (Ribberink [7]). Such empirical models were mainly developed under simple flow conditions and have a limited range of applicability, and they provide no description of the the dynamical behavior involved in either phase. Due to the rapid increase in computational power, more advanced numerical models were developed to resolve sediment transport dynamics at different scales, which will be discussed in the following section.

1.3 Computational models for sediment transport

In this section, several commonly used computational approaches for multiphase flows are reviewed (Balachandar and Eaton [8]) with an emphasis of their applications in sediment transport, which includes fully resolved Direct Numerical Simulation (DNS) and four different modeling methods, as shown in Figure 1.2. Under extremely dilute concentrations, $\phi_v < 10^{-5}$, the interaction between the dispersed phase and the carrier phase can be treated as one-way coupled, meaning that the motion of the dispersed phase is governed by the carrier flow, while the inverse influence is negligible; under moderate dilute conditions, $10^{-5} < \phi_v < 0.001$, the interaction between the two phases is “two-way coupled”, indicating that the back action of the dispersed phase on the carrier phase flow cannot be neglected

and plays a critical role in modifying the turbulence statistics; further increasing the volume concentration, $\phi_v > 0.001$, the inter-particle and particle-wall collisions become more and more frequent and thus have to be accounted for, in which the interaction among entities is “four-way coupled”. In sediment transport, the bulk of the suspended load layer should be described by two-way coupled models; while the bed load layer requires additional inter-particle interactions to be accounted for.

The vertical axis in Figure 1.2 denotes the particle-to-fluid length scale ratio, d/η , and time scale ratio, τ_p/τ_k (also known as the particle Stokes number St). In the previous, d is the particle diameter, η is the Kolmogorov length scale in the flow, τ_p is the particle response time and τ_k is the Kolmogorov time scale. The evaluation of each term in the current study is introduced below. The particle response time, τ_p , is defined as the time required for a particle to reach the terminal settling velocity when released in a quiescent fluid, which can be theoretically computed by solving an ordinary differential equation governing the particle’s motion (see Chapter 4.3.1 for details). The Kolmogorov scales (time or length) are defined by the turbulent dissipation rate, ϵ , whose determination requires the measurement of the full velocity gradient tensor. In the current study, stereoscopic PIV was implemented in the carrier phase measurement, in which three dimensional velocity components were calculated only on a two dimensional plane coinciding the light sheet center (referred to as “2D3C” measurement), so the velocity gradient in the out-of-plane direction couldn’t be obtained. As a result, the dissipation rate could not be directly measured and the required Kolmogorov scales were estimated as the following. We assumed the Kolmogorov velocity scale is of the same order as the friction velocity (u_τ) and

approximated the Kolmogorov length and time scales as the viscous scales, written as ν/u_τ and ν/u_τ^2 respectively. The particle Stokes number defined in this way can be expressed as, $\tau_p u_\tau^2/\nu$, and is often referred to as the wall Stokes number. Such approximations tend to overestimate the values of the length scale ratio and the particle Stokes number computed with true Kolmogorov scales, but are at least good representatives of the order of magnitude.

In Figure 1.2, with extremely low Stokes numbers ($St \ll 1$), the particles act as “tracers” that can faithfully follow the motion of the ambient flow, which is the assumption made by the dusty gas models. For slightly higher Stokes numbers, i.e. $St < 0.2$, the slip velocity between phases cannot be ignored, however the Stokes number is still low enough that an equilibrium can be reached between the motion of the two phases and the dispersed phase velocities are completely dictated by the local flow. The slip velocity can be theoretically derived and often expressed as the particle fall velocity plus an asymptotic expansion term with respect to the Stokes number (Ferry and Balachandar [9]), which forms the fundamental idea used in the equilibrium Eulerian method. For even higher Stokes numbers, more sophisticated models, such as Eulerian and Lagrangian point-particle models and even fully resolved DNS are demanded to resolve the behavior of both phases reliably. It should be noted that in Figure 1.2, the small length ratio constraint ($d/\eta < 0.1$) is imposed on all the computational modelings unless fully resolved DNS is conducted.

Sediment transport models can be generally categorized into single-phase models and two-phase models, which are similar to the one-way coupled and two(or three)-way coupled concepts stated above respectively. The single-phase models are

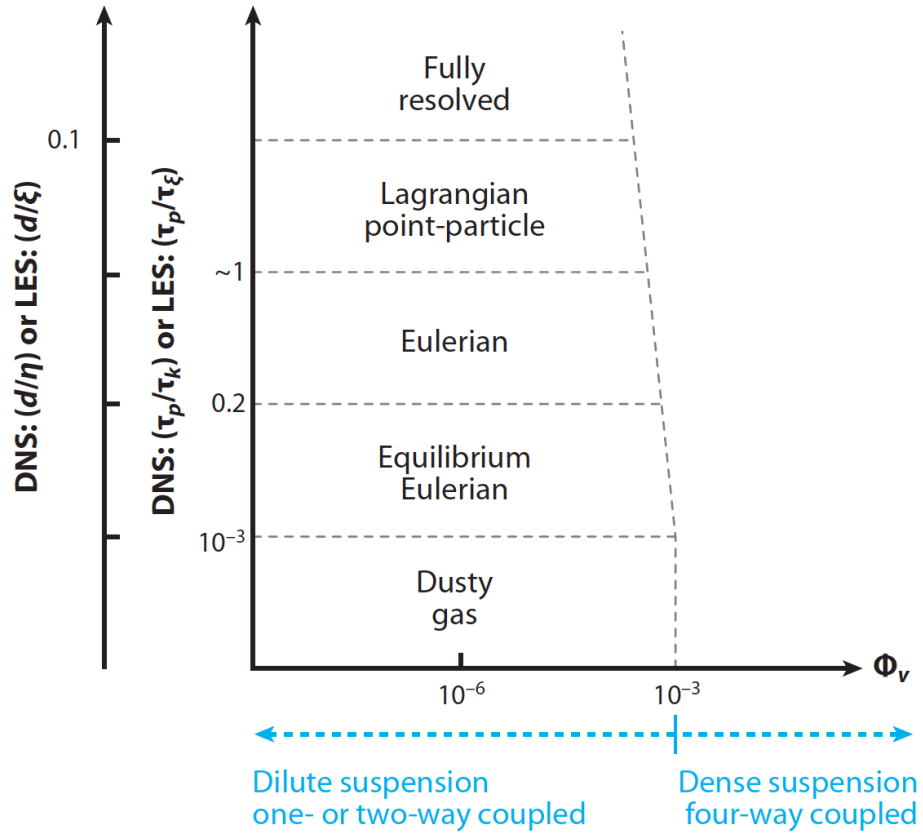


Figure 1.2: Recommended computational approaches under different multiphase flow conditions parameterized by the volume fraction, ϕ_v , the length ratio d/η and the particle Stokes number, defined as the time ratio $St = \tau_p/\tau_k$, where η is the Kolmogorov time scale, τ_p is the particle response time and τ_k is the Kolmogorov time scale. (cited from Balachandar and Eaton [8])

formulated based upon the dusty gas or the equilibrium Eulerian approach. With the dusty gas approach, the sediment particles are assumed to be passively transported by the bottom boundary layer flow and no or only very simplified back reactions of particles on the flow is considered. The bottom boundary layer flow can be solved either via the single phase Navier-Stokes equations or by some wave-current models. The dispersed phase concentration field can then be solved via an advection-diffusion equation once the carrier phase flow is solved. The influence of the dispersed phase on fluid turbulence can be accounted for simply through a sediment-induced density stratification term. Compared to the dusty gas approach, the equilibrium Eulerian approach allows a theoretically derived slip velocity between phases, which is often used to model the transport of fine sediment particles ($d < 0.15 \text{ mm}$, Cheng et al. [10] and Cheng et al. [11]) in order to satisfy the particle Stokes number criteria ($St < 0.2$, Ferry and Balachandar [9]). This approach outperforms the former one due to its more accurate representation of the particle velocities by accounting for particle's inertia, enabling the study of preferential concentration and the resultant modification of turbulence. The solution of single phase models is only valid within dilute concentrations (due to the one-way coupling assumption) and thus is typically used to model only the suspended load transport. The computational domain is often above the immobile sediment bed layer and thus its bottom boundary condition has to be cautiously imposed, either by applying a reference concentration or specifying an empirical sediment flux (representing the net result of erosion and deposition). The transport in the bed-load layer can be solved separately and parameterized with the dimensionless parameters introduced in Section 1.2 (Bagnold

[12], Van Rijn [13]).

The advantage of single phase models are their low computational cost that enables their applications in large-scale and even field-scale simulations (Lesser et al. [14], Hagatun and Eidsvik [15], Zhang et al. [16], Harris and Wiberg [17]), however they are only valid for significantly small particles ($d/\eta < 0.1$), small particle Stokes numbers ($St < 0.2$) and low concentrations ($\phi_v < 0.001$). In a typical sheet flow with water and spherical Quartz sand particles of medium size ($\rho_{s,qz} = 2.56 \text{ g/cc}$, $0.15 < d < 0.50 \text{ mm}$), the particle response time, τ_p , can be computed as varying from 3 ms to 13 ms ; for the flow scales in a typical turbulent boundary layer, the friction velocity is often on the order of $\mathcal{O}(1 \sim 10 \text{ cm/s})$, which corresponds to an estimated $\eta \approx \nu/u_\tau$ on the order of $\mathcal{O}(0.1 \text{ mm})$ and τ_k on the order of $\mathcal{O}(1 \text{ ms})$. Under the above flow conditions, the associated particle-to-fluid length scale ratio and particle Stokes number are both on the order of $\mathcal{O}(1 \sim 10)$, which apparently cannot satisfy the assumptions made by single-phase models. Moreover, the bottom boundary conditions have to be specified in single-phase models via simplified parametric/empirical models, whose validity is often questionable especially in unsteady flows.

More advanced two-phase sediment transport models were developed in the past two decades, built under the framework of the Eulerian approach, the Lagrangian point-particle approach or fully resolved DNS (Figure 1.2), in which the mass and momentum equations of each phase are coupled together by the interaction force terms between the phases. In this dissertation, focus will be placed on studying the particle-turbulence interaction occurred in dilute regime ($10^{-5} < \phi_v < 0.01$)

under oscillatory sheet flow conditions, where the inter-particle collisions can be neglected and an intense particle-turbulence interaction is guaranteed. The particle-to-fluid length scale ratio and the particle (wall) Stokes number obtained under our experimental condition are estimated as $d/\eta = 16.3$ and $St_w = 27.1$ respectively, both of which exceed the criteria required by all of the four computational models proposed in Figure 1.2 (except for DNS). Despite of the questionable formulation of the Eulerian and Lagrangian point-particle models, they still represent the state-of-the-art and have generated valuable insights on sediment transport mechanisms. Both of them, along with full resolved DNS, will be discussed in detail below, with their advantages and possible improvements pointed out when applied to sheet flows.

1.3.1 Fully resolved DNS

Fully resolved DNS completely solves the rigid/deformable body motion of every particle and resolves all the scales of ambient turbulence and particle-induced turbulence. The governing equations (Breugem [18], assuming rigid spherical particles) describing the carrier phase flow are the single phase Navier-Stokes equations; while for the dispersed phase, a set of ordinary differential equations that governs both the translational velocity and the angular velocity of each particle needs to be solved, generating a complete description of rigid particle motion. The force and torque acting on each particle by the ambient flow can be computed by directly integrating the local pressure and shear stress acting on the surface and the collisional/frictional forces exerted between particles or against solid walls can also be

accounted for. The back reaction of particles on the flow enters the Navier-Stokes equations via the no-slip and no-penetration boundary conditions imposed on the surface of each solid particle.

Different numerical schemes, such as the Immersed Boundary Method (IBM, Uhlmann [19], Breugem [18], Picano et al. [20]), Volume of Fluid (VOF), structured grid, Lattice Boltzmann etc. can be implemented to solve the above partial differential equations and ordinary differential equations that are strongly coupled together. The advantage of fully resolved DNS resides in its ability to provide an accurate, high-fidelity and high-resolution delineation of both phases without introducing any closure models. However, it is computationally expensive. To date, researchers have been able to apply fully resolved DNS to approximately 10,000 solid particles in turbulent channel flows and isotropic/homogeneous turbulent flows both in the absence of sediment bed (Picano et al. [20], de Motta et al. [21] and Peng et al. [22]). However, a typical sheet flow simulation requires at least tens of millions of sediment particles, estimated with 10 *cm* thick bottom boundary layer, 2 *mm* thick sheet flow layer and 0.2 *mm* grain size (Cheng et al. [23]). Due to the overwhelmingly expensive computational efforts required, fully resolved DNS of sheet flows is out of the question in the foreseeable future.

1.3.2 Lagrangian point-particle approach

In sediment transport, the Lagrangian point-particle approach (also known as “Eulerian-Lagrangian model”) treats each individual sediment particle as “point

mass” and uses a Lagrangian description to track their positions, momentum and angular momentum etc. Since the particle-fluid interface is not resolved, the inter-phase and inter-particle forces have to be modeled. The carrier phase equations, on the other hand, are formulated via the volume averaged Navier-Stokes equations, closed with constitutive relations required for the residual stresses due to spatial filtering and the reaction particle forces (Zhou et al. [24], Anderson and Jackson [25]). The equations governing the linear momentum of sediment particles and the continuous carrier phase flow are summarized in Equations 1.4~1.6 and Equations 1.7~1.9 respectively (Zhou et al. [24], Anderson and Jackson [25], Finn et al. [26]). In these equations, \vec{u} , ρ and P represent velocity, density and pressure, which are accompanied by subscript f or p referring to the corresponding phase (fluid or particle). The equations of the two phases are coupled via sediment volumetric concentration, C , and the inter-phase momentum transfer term, \vec{f}_{fp} or \vec{F}_{pf} .

The sediment particle motion is described by the Newton’s equation, which is written as,

$$m_p \frac{d\vec{u}_p}{dt} = m_p \vec{g} + \vec{f}_{fp} + \vec{f}_c \quad (1.4)$$

$$\begin{aligned}
\vec{f}_{fp} = & \underbrace{-V_p \nabla P_f|_p}_{\text{Pressure}} + \underbrace{C_d \frac{1}{2} A_p \rho_f |(\vec{u}_f|_p - \vec{u}_p)|(\vec{u}_f|_p - \vec{u}_p)}_{\text{Drag}} \\
& + \underbrace{C_l V_p \rho_f (\vec{u}_f|_p - \vec{u}_p) \times (\nabla \times \vec{u}_f)|_p}_{\text{Lift}} + \underbrace{C_{AM} V_p \rho_f \left(\frac{D\vec{u}_f|_p}{Dt} - \frac{d\vec{u}_p}{dt} \right)}_{\text{Added mass}} \\
& + \underbrace{\frac{3}{2} d^2 \sqrt{\pi \rho_f \mu} \int_{-\infty}^t K(t, \tau) \frac{d(\vec{u}_f|_p - \vec{u}_p)}{d\tau} d\tau}_{\text{Basset history}}
\end{aligned} \tag{1.5}$$

$$\phi_f|_p = \sum_{\text{CV}} \mathcal{I}(\vec{x}, \vec{x}_p) \phi_f \tag{1.6}$$

Each sediment particle is subjected to the gravitational force, $m_p \vec{g}$, the hydrodynamic force, \vec{f}_{fp} , and the particle collision force, \vec{f}_c . The mutual hydrodynamic force, \vec{f}_{fp} , can be further decomposed into pressure, drag, lift, added mass and Basset history forces, as expressed in sequence in Equation 1.5 (Maxey and Riley [27]), in which μ is the molecular dynamic viscosity of the fluid, m_p , V_p and A_p denote the mass, volume and projected area associated with each single sediment particle, C_d , C_l and C_{AM} are the coefficients of drag, lift and added mass respectively and $\frac{D}{Dt}$ represents the material derivative. The subscript $|_p$ represents the undisturbed fluid property evaluated at the particle centroid location, \vec{x}_p , which is often defined via some interpolant function denoted by $\mathcal{I}(\vec{x}, \vec{x}_p)$ as shown in equation 1.6. The Basset history force quantifies the accumulative effect of the diffused vorticities originated from the particle surfaces, and in the above equation, $K(t, \tau)$ is the kernel that weighs the past history of relative acceleration. \vec{f}_c is formulated by means of

discrete element method (DEM), accounting for the collisional and frictional forces occurred among the particles and only plays a crucial role in concentrated regions.

The volume averaged Navier-Stokes equations that governs the carrier phase flow can be written as,

$$\frac{\partial}{\partial t} [\rho_f(1 - C)] + \nabla \cdot [\rho_f(1 - C)\vec{u}_f] = 0 \quad (1.7)$$

$$\begin{aligned} \frac{\partial}{\partial t} [\rho_f(1 - C)\vec{u}_f] + \nabla \cdot [\rho_f(1 - C)\vec{u}_f\vec{u}_f] = & -\nabla P_f - (1 - C)\rho_f\vec{g} \\ & + \nabla \cdot \left[\mu_{eff} \left(\nabla\vec{u}_f + (\nabla\vec{u}_f)^T - \frac{2}{3}\nabla \cdot \vec{u}_f \right) \right] + \vec{F}_{pf} \end{aligned} \quad (1.8)$$

$$\phi_f(\vec{x}) = \sum_{i_p=1}^{n_p} \mathcal{F}(\vec{x}, \vec{x}_p)\phi_p \quad (1.9)$$

in which the definition of the reaction force, \vec{F}_{pf} , exerted from the particle surface back to the flow (opposite to \vec{f}_{fp}), and the local sediment concentration, C , both rely on the filter function as shown in Equation 1.9. $\mathcal{F}(\vec{x}, \vec{x}_p)$ distributes a point particle property (the reaction particle force, $-\vec{f}_{fp}$, or particle volume, $\pi d^3/6$), ϕ_p , to the continuous field, ϕ_f , located at the Eulerian grid points, \vec{x} . The effective viscosity of sediment-fluid suspension, μ_{eff} , can be modeled to account for the molecular dynamic viscosity of the fluid, particle concentration, particle polydispersity, and the unresolved subgrid-scale turbulence stresses due to volume averaging. It should be pointed out that there is not yet a universal agreement on the design of the

interpolant function, $\mathcal{I}(\vec{x}, \vec{x}_p)$, or the filter function, $\mathcal{F}(\vec{x}, \vec{x}_p)$, that should be used in the above Eulerian-Lagrangian models (Brandt and Coletti [28], Deen et al. [29], Delnoij et al. [30], Zhao and Shan [31]).

The resultant carrier phase equations (Equations 1.7~1.9) can be solved via direct numerical simulation (DNS), large eddy simulation (LES, Finn et al. [26], Schmeckle [32]), or further averaged and solved under the framework of Reynolds averaged Navier-Stokes model (RANS, Cheng et al. [23], Rafati et al. [33], Shi and Yu [34]) (Kuerten [35]). The Eulerian-Lagrangian RANS model, in which the RANS equations are solved for the carrier phase and individual sediment particles are still tracked according to Equations 1.4~1.6, is motivated by its much less required computational cost. In dilute regions, where the sediment particles are mostly driven by the ambient turbulent (and unresolved) flow, the dispersion of the sediment particles has to be modeled via some type of stochastic Lagrangian model, such as the random-walk model (RMW) and eddy interaction model (EIM). These stochastic Lagrangian models still lack experimental validation, especially when applied in oscillatory sheet flows. The Lagrangian statistics of the sediment particles, the turbulent statistics along particle trajectories and their correlations are vital for the improvement of these models, which motivates the whole field, particle-resolved, time-resolved and simultaneous measurements on both phases in the dilute regions in sheet flow.

1.3.3 Eulerian approach

The Eulerian approach (also known as “Eulerian-Eulerian model”) is based upon a two-fluid model, which treats the carrier phase and the dispersed phases as two interpenetrating continua and gives the particulate phase properties field representation. The two-fluid formulation requires the conservation of mass and momentum equations for both phases, with momentum exchange between the phases taken into account as source and sink terms. When applied in sediment transport, the Eulerian approach has demonstrated its capabilities of both predicting bulk quantities such as the sediment transport rate (Amoudry et al. [36]), and resolving fine structures in the flow such as the intermittent bed failure (Cheng et al. [37]), under various flow conditions. It also requires typically less computational cost than the Lagrangian point-particle approach, in which millions of particles have to be tracked. In this section, the mathematical equations of the Eulerian approach are formulated first under the context of sediment transport with mono-dispersed spherical particles, which is then followed by a discussion of the resultant closure models frequently occurred in this approach.

1.3.3.1 Mathematical formations of FANS model

The starting point for the two-fluid model begins with the exact and fully-resolved representation of the conservation laws for the two media, which are defined in disconnected regions with jump boundary conditions specified on their interfaces. The above equations are then transformed into a globally defined mass and mo-

momentum equations for both phases through some type of “grain-scale” averaging. Different grain-scale averaging operators can be used, such as the ensemble averaging (Drew [38], Drew and Lahey [39], Zhang and Prosperetti [40]) and the spatial averaging (Jackson [41], Brennen [42]). The resulting governing equations can be considered as the counterpart of the single-phase fluid Navier–Stokes equations. However, unlike the Navier–Stokes equations, the two-fluid governing equations are not closed and several terms require closure models as a result of “grain-scale” averaging, such as the sediment and fluid stress tensor terms (Gonzalez-Ondina et al. [43]). Especially when dealing with large particles that have finite to large particle Reynolds number ($Re = du_\tau/\nu \gg 1$), the details within the boundary layer and wakes generated by the particles are smoothed out and modeled in the fluid stress tensor term, whose validity needs to be carefully examined. The sediment stress term characterizes the interaction between particles and only needs to be accounted for in concentrated regions. The inter-phase momentum transfer terms would also need to be modeled based upon the particle force equations as shown in Equations 1.5 (Maxey and Riley [27]).

To solve these equations, LES and multi-dimensional Reynolds/Favre Averaged Navier-Stokes (RANS or FANS) equations are commonly used in a wide range of applications, such as steady flow (Cheng et al. [37], Gonzalez-Ondina et al. [43], Hsu et al. [44], Hsu et al. [45] etc.), oscillatory flow (Amoudry et al. [46], Amoudry et al. [36], Amoudry [47], Hsu et al. [45], Yu et al. [48] etc.), scouring (Cheng et al. [4], Amoudry and Liu [49] etc.) etc. The mathematical formulation of RANS/FANS two-fluid model is derived by applying a second average to the grain-scale governing

equations over a scale much larger than the particle size to further smooth out the turbulence fluctuations (termed as “large scale averaging” analogous to Reynolds average). The resultant turbulence-averaged two-fluid model (FANS, Amoudry et al. [36]) is demonstrated below, where Favre averaging (concentration weighted average, denoted by “ \sim ”) is applied to velocities and traditional averaging (ensemble, spatial or temporal, denoted by “ $\bar{}$ ”) is applied to all the other quantities. The Favre averaged velocities for both phases are defined as,

$$\tilde{u}_i^f = \frac{\overline{(1-C)u_i^f}}{1-\bar{C}} \quad (1.10)$$

$$\tilde{u}_i^s = \frac{\overline{Cu_i^s}}{\bar{C}} \quad (1.11)$$

$$C' = C - \bar{C}, \quad \Delta u_i^f = u_i^f - \tilde{u}_i^f, \quad \Delta u_i^s = u_i^s - \tilde{u}_i^s$$

where C is the volume fraction of sediment particles and u_i represents the velocity components with superscript denoting the corresponding phase. Based upon Favre averaging defined above, the mass conservation equations of the carrier phase and sediment phase are written as the following:

$$\frac{\partial \rho_f(1-\bar{C})}{\partial t} + \frac{\partial \rho_f(1-\bar{C})\tilde{u}_i^f}{\partial x_i} = 0 \quad (1.12)$$

$$\frac{\partial \rho_s \bar{C}}{\partial t} + \frac{\partial \rho_s \bar{C} \tilde{u}_i^s}{\partial x_i} = 0 \quad (1.13)$$

The momentum equations for the carrier phase and the sediment phase are expressed as the following:

$$\begin{aligned}
\frac{\partial \rho_f (1 - \bar{C}) \tilde{u}_i^f}{\partial t} + \frac{\partial \rho_f (1 - \bar{C}) \tilde{u}_i^f \tilde{u}_j^f}{\partial x_j} &= \rho_f (1 - \bar{C}) g_i - (1 - \bar{C}) \frac{\partial \bar{P}_f}{\partial x_i} + \underbrace{\overline{C' \frac{\partial P_f'}{\partial x_i}}}_{\text{Pressure fluctuation}} \\
&\quad - \beta \bar{C} (\tilde{u}_i^f - \tilde{u}_i^s) - \underbrace{\overline{\beta C \Delta u_i^f}}_{\text{Turbulent suspension}} + \underbrace{\frac{\partial}{\partial x_j} (R_{ji}^f + \overline{(1 - C) T_{ji}^f})}_{\tau_{ij}^f, \text{ total fluid phase stress}}
\end{aligned} \tag{1.14}$$

$$\begin{aligned}
\frac{\partial \rho_s \bar{C} \tilde{u}_i^s}{\partial t} + \frac{\partial \rho_s \bar{C} \tilde{u}_i^s \tilde{u}_j^s}{\partial x_j} &= \rho_s \bar{C} g_i - \bar{C} \frac{\partial \bar{P}_f}{\partial x_i} + \underbrace{\overline{C' \frac{\partial P_f'}{\partial x_i}}}_{\text{Pressure fluctuation}} + \beta \bar{C} (\tilde{u}_i^f - \tilde{u}_i^s) \\
&\quad + \underbrace{\overline{\beta C \Delta u_i^f}}_{\text{Turbulent suspension}} + \underbrace{\frac{\partial}{\partial x_j} (R_{ji}^s + \overline{C(P_s - P_f)} \delta_{ij} + \overline{C T_{ji}^s})}_{\tau_{ij}^s, \text{ total sediment phase stress}}
\end{aligned} \tag{1.15}$$

where β is the averaged drag coefficient, P_f and P_s denote the fluid and sediment pressure, T_{ji}^f and T_{ji}^s are the stress tensors for the fluid phase and the sediment phase, containing the viscous stress and the small-scale Reynolds stress as a result of grain-scale averaging, and R_{ji}^f and R_{ji}^s represent the large-scale Reynolds stresses, obtained when averaging the non-linear convective terms (analogous to the Reynolds stress terms in single-phase fluid RANS model),

$$R_{ji}^f = -\rho_f \overline{(1 - C) \Delta u_i^f \Delta u_j^f} \tag{1.16}$$

$$R_{ji}^s = -\rho_s \overline{C \Delta u_i^s \Delta u_j^s} \quad (1.17)$$

For the inter-phase coupling term, only the drag force is considered in Equations 1.14~1.15, and all the other force terms are comparatively small and thus neglected, which can be justified under most sediment transport conditions with scale analysis (Amoudry et al. [36]).

Of all the terms contained in the above Favre Averaged Navier-Stokes model (FANS, Equations 1.12~1.15), the ones needed to be further evaluated by closure models due to both the “grain scale” and “large scale” averaging are labeled with brackets beneath them. They are crucial to the performance of FANS model and will be discussed next.

1.3.3.2 Problems with closure models

In this dissertation, we refrain from discussing the pressure fluctuation and the total sediment phase stress terms. The measurement of the former is exceedingly difficult, and the neglect of the latter is because it captures the effect of inter-particle collisions, which is only dominant in concentrated regions ($c > 0.08$) exceeding the range of concentrations of our interest ($c = 10^{-5} \sim 10^{-1}$). The drag coefficient, β , has been heavily studied in the past decades (Ding and Gidaspow [50], Richardson and Zaki [51] etc.), and both theoretical and empirical models were developed that have been able to produce reasonable drag force predictions. We will restrict our attention to the modeling of the remaining two terms, $\overline{C \Delta u_i^f}$ and τ_{ij}^f as shown

in Equations 1.14~1.15. The unsteady effects observed in oscillatory sheet flow experiments, which are only crudely captured by two-fluid model closures at present, are also discussed.

1. Turbulent suspension term, $\overline{C\Delta u_i^f}$. The turbulent suspension term denotes the correlation between the concentration and the large-scale fluid velocity fluctuations and is commonly modeled using the gradient diffusion hypothesis, $\overline{C\Delta u_i^f} = -\frac{\nu_T}{\sigma_c} \frac{\partial \bar{C}}{\partial x_i}$, where σ_c , is the Schmidt number, defined as the ratio of the sediment diffusivity over the turbulent eddy viscosity, ν_T . The value of the Schmidt number, σ_c , may vary both spatially and temporally in an oscillatory sheet flow, and there is not a universal agreement yet on how much it should be used. Cheng et al. [37] developed an LES two-fluid model and used it in a steady sheet flow with coarse sediment particles. The grid size was selected to be small enough such that the uncertainties associated with subgrid closure is minimized. The Schmidt number predicted by the model ($\sigma_c = 0.55$) in dilute regime is larger than the experimentally determined value ($\sigma_c = 0.44$ by Revil-Baudard et al. [52]) by about 25%, indicating that some physical mechanisms of the turbulent-sediment interactions were still not properly accounted for.

Along with the turbulent suspension term, some other terms are also generated when (Favre) averaging the inter-phase momentum transfer term, expressed as $\overline{\beta' C'(\tilde{u}_i^f - \tilde{u}_i^s)} + \overline{\beta' C(\Delta u_i^f - \Delta u_i^s)}$. These terms are often neglected in two-fluids models mainly for simplicity, lacking of physical reasoning. Thus, their evaluation could also be important for improving the FANS model, which requires the calculation of concentration-velocity covariance and even triple correlations.

2. The total fluid phase stress, τ_{ij}^f . The total fluid phase stress consists of three parts, the large-scale Reynolds stress, the grain-scale Reynolds stress and the molecular viscous stress. The grain-scale Reynolds stress and the molecular viscous stress are combined in the term T_{ji}^f and the former one is usually neglected mainly for simplicity. However, Gonzalez-Ondina et al. [43] developed a two-level, two-phase FANS model, where the grain-scale and large-scale fluctuations in both phases were modeled independently. The author claims that the grain-scale fluid fluctuations have a large impact in the flow and should not be overlooked. The large-scale Reynolds stress, R_{ji}^f , is often modeled using the eddy viscosity hypothesis, where the turbulent eddy viscosity, ν_T , has to be further specified. Candidate models for determining the value of ν_T consists of mixing length model, one-equation model, two-equation model etc., built upon the same framework used for single-fluid turbulence models. Model parameters can be adjusted to account for the additional effects of sediment concentration and particle forces, which are exceedingly difficult to be predicted and normally have to be empirically calibrated. A further understanding of the turbulence modulation mechanisms due to the presence of sediment particles would allow the determination of the parameters in a more rational manner.

3. Unsteady effects in oscillatory sheet flow. Some unique unsteady phenomena have been experimentally observed in oscillatory sheet flow, such as concentration peaks occurred at flow reversal (O'Donoghue and Wright [54], Ribberink and Al-Salem [53]) and phase lag effects (O'Donoghue and Wright [54], O'Donoghue and Wright [55], Ribberink and Al-Salem [53]). However, the two-fluid FANS model doesn't seem to be able to capture these phenomena, indicating that some physics

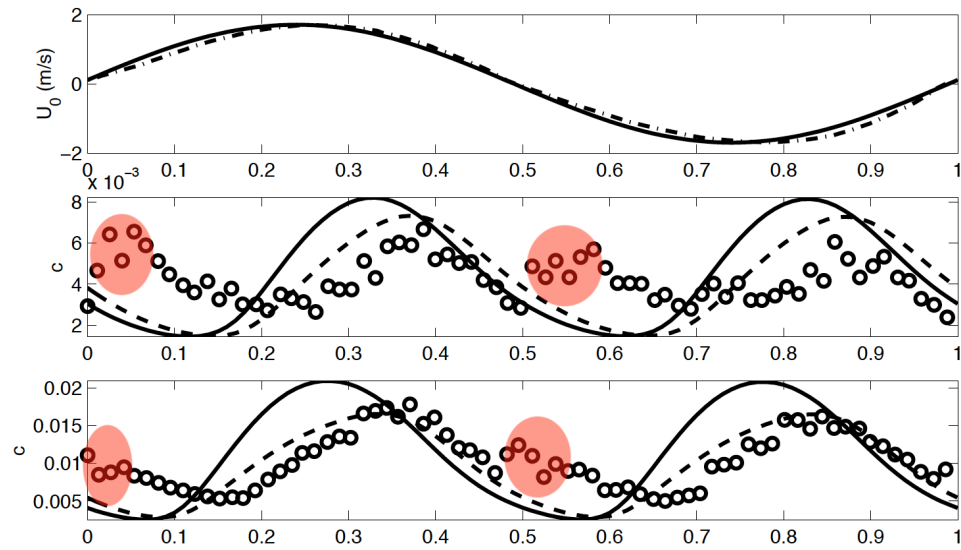


Figure 1.3: The top figure shows the periodic free stream velocity in one cycle. The bottom two figures show the concentration time histories at two different elevations (at $z/D_{50} = 100$ and $z/D_{50} = 52$ respectively, with $D_{50} = 0.21 \text{ mm}$), using van Rijn's pick-up (solid line) and the reference concentration approach (dashed line) for bottom boundary conditions, superimposed by the measured data of Ribberink and Al-Salem [53] (symbols). (cited from Amoudry [3])

related to the unsteady motion must have been ignored in the model. Amoudry [3] implemented a one-dimensional FANS model in only the dilute regime, where the intergranular stress was neglected and the bottom bed effects were accounted for via boundary conditions. The numerical results compared with the measured data (Ribberink and Al-Salem [53]) is shown in Figure 1.3, where the concentration time histories at two select elevations are presented. At these two elevations, the range of concentration matches the concentration range of our interests ($C = 10^{-5} \sim 10^{-1}$). It is shown in the figure that right after the flow reverses the direction, an increase of concentration is observed in experiments (see shaded regions), which is completely absent in the simulation. Another oscillatory sheet flow simulation done by Chen et al. [56] was compared with the measured data obtained by O’Donoghue and Wright ([54] and [55]), as shown in Figure 1.4. Chen et al. [56] used a one-dimensional RANS averaged two-fluid model, accounting for the turbulence modification under different volume concentrations by introducing a slightly modified $k - \varepsilon$ model. It is shown in this figure that the phase lag predicted by the model (solid line in the bottom figure) is apparently inconsistent with the measured data (solid dot symbols), implying something inherent in the oscillatory nature of the external flow must have been omitted. The slightly better prediction of the phase lag denoted by the dotted line is given by Li et al. [57], in which the authors had to include several empirical formulas in their two-fluid RANS model. To the author’s best knowledge, the particle suspension mechanisms and turbulence modulation under adverse pressure gradient (during flow deceleration) is still poorly understood, which is, however, believed to be critical for the improvement of the current oscillatory sheet

flow models.

1.4 Experimental studies in sediment transport

It has been shown in the previous section that all of the equations (even the most fundamental ones) used in the Eulerian-Lagrangian and the Eulerian-Eulerian models have been averaged to some extent and contain closure models. In the Eulerian-Lagrangian models, the evaluation/improvement of the interpolant function, \mathcal{I} , and the filter function, \mathcal{F} , depends on knowing each individual particle's locations and the associated hydrodynamic force, the latter of which can be only indirectly acquired by measuring each particle's instantaneous velocity and acceleration and the flow field around it; the improvement of stochastic Lagrangian models would require measuring the Lagrangian statistics of both phases, which involves tracking each individual particle's positions and its surrounding flow over consecutive frames. In the Eulerian-Eulerian models, all the closure terms associated with grain-scale averaging must be evaluated by extremely detailed measurement with each individual particle resolved for the sediment phase and Kolmogorov scale resolved for the carrier phase.

The measurement goals set by this thesis is to produce whole field, time-resolved, particle-resolved and concurrent measurements of both phases up to a volume concentration of 1% in an oscillatory sheet flow. In this section, some commonly used sheet flow measurement techniques are summarized, followed by a literature review of the most detailed sheet flow measurements conducted recently. It will

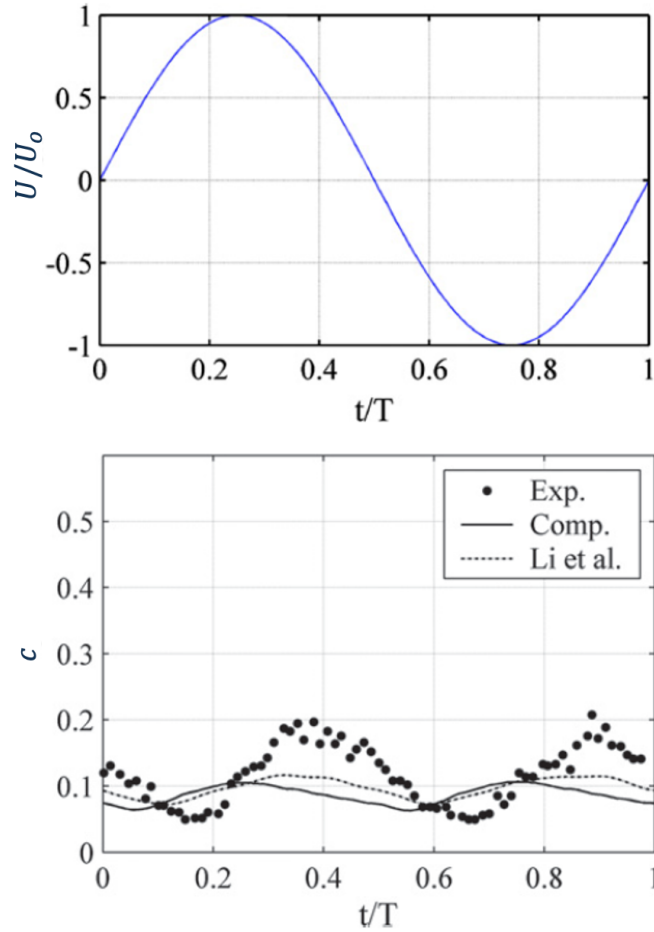


Figure 1.4: The top figure shows the periodic free stream velocity in one cycle. The bottom figure shows the concentration time histories at $y = 2.5 \text{ mm}$, using one-dimensional two-fluid RANS model by Chen et al. [56] (solid line) and by Li et al. [57] (dotted line), superimposed by the measured data of O'Donoghue and Wright ([54] and [55], symbols). (cited from Chen et al. [56])

be shown that none of the existing measurement could satisfy all the measurement goals set by the thesis.

The earliest recorded measurements of sheet flow conditions utilized suction sampler and pitot tube to measure the sediment concentration and velocity respectively (Bosman et al. [58]). The shortcomings of such instrumentation are manifold: they are physically intrusive, measure only at a single point, have poor spatial and temporal resolution, and cannot discriminate the velocity signals between the two phases. In the past two decades, Concentration Conductivity Meters/Profilers (CCM/CCP) were developed and widely used in both laboratory and field measurements, which is able to acquire a full sediment concentration profile from random close-packed sand to moderately dilute region after a careful calibration of the conductivity of known sand/fluid mixture concentrations. The CCM/CCP is intrusive and only accurate for moderate-to-high volume fractions $C > 5\%$. In more dilute regimes ($C < 5\%$), concentration can be measured separately by the Acoustic Back Scattering (ABS) system instead. Utilizing two CCMs/CCPs placed in a row along the streamwise direction and by correlating the upstream and downstream concentration signals, one can obtain the sediment velocity in the streamwise direction. The resolution of such velocity measurement is limited due to the flow disturbance caused by the upstream CCM/CCP probe. Instead, an Ultrasonic Velocity Profiler (UVP) is usually employed for sediment velocity measurement, though UVP cannot distinguish independent measurements of the sediment particles and their ambient flow. Some measurement techniques that can register the instantaneous velocities of both phases include Laser Doppler Velocimetry (LDA), Phase Doppler Velocimetry

(PDA), and Particle Image Velocimetry (PIV). LDA and PDA are both point measurements and the signals from the two phases (reflections from tracer and sediment particles) need to be discriminated. The size of sediment particles are typically much greater than that of tracer particles and therefore they tend to produce a brighter intensity signal. In LDA, the distinct intensities of the bursts reflected by the two phases can be used for phase separation (Stock et al. [59], Muste et al. [60]); while for PDA, the particle sizes can be directly measured, which can be used for phase identification. One limitation of single-point measurements, however, is the difficulty associated with interpreting the data into meaningful physical mechanisms that control the dynamics between the phases. PIV, on the other hand, has the potential of achieving the measurement goals set for this dissertation (whole field, particle-resolved and concurrent) and thus is used. A detailed review of PIV/PIV-based measurement techniques is presented in Section 2.1.1.

Some most detailed measurements conducted recently in sheet flows are listed below. Revil-Baudard et al. [52] used acoustic concentration and velocity profiler (ACVP), which allowed the measurement of the co-located streamwise and vertical particle velocity components as well as the particle volumetric concentration over a vertical profile extending from the bed interface to the water free surface. However, some major problems associated with this technique are 1) it cannot discriminate the velocities between the two phases, therefore the inter-phase momentum transfer term cannot be directly evaluated; 2) the measurement was conducted along a vertical line, which precludes the study of coherent structures exhibited by the particles and the flow. In another experiment, Capart and Fraccarollo [61] used two

high-speed cameras and a laser light sheet to simultaneously measure the detailed profiles of sediment velocity and concentration near the sidewall. The first camera, viewing perpendicular to the side wall, registers the motion of each sediment particle adjacent to the sidewall, from which instantaneous in-plane velocities of each individual particle can be computed by particle tracking velocimetry. The second camera, oriented obliquely, records the deformation of a laser stripe projected onto the near-wall particles by a transverse laser light sheet, from which the near-wall sediment concentration can be calculated (Spinewine et al. [62]). Two major shortcomings of this measurement are its reliance on the sidewall where the boundary layer effects cannot be ruled out, and the lack of measurement of the carrier phase flow.

It is worth mentioning that numerous detailed concurrent PIV/PTV measurements of particulate flows do exist, however they were mostly conducted in turbulent channels without the presence of sediment bed and the particle concentration encountered is typically very small, varying from only a few particles (Tee et al. [63] etc.) to $C \sim \mathcal{O}(0.1\%)$ (Muste et al. [64], Kiger and Pan [65], Tanaka and Eaton [66], Petersen et al. [67], Berk and Coletti [68] etc.). In sheet flow measurements, the existence of the sediment bed, the requirement of making measurements away from the side walls and the measurement goals set by this thesis (whole field, particle-resolved and concurrent measurements of both phases for $C \leq 1\%$) combined define an extremely challenging measurement problem. In fact, to the author's best knowledge, such measurements has never been conducted before, which motivates the author to take on this challenging task.

1.5 Scope of this thesis

It has been shown in previous sections that further improvement of the state-of-the-art sheet flow models (Lagrangian point-particle and Eulerian two-fluid models) would require at least whole field, particle-resolved and concurrent measurements of the dynamical behavior of both phases to gain more insight on the particle suspension mechanisms and turbulence modifications. The Lagrangian statistics of both phases are crucial for the validation and improvement of existing stochastic Lagrangian models, so time-resolved measurements are also highly recommended. This dissertation aims to provide such measurements in a precisely-controlled and highly-repeatable oscillatory sheet flow with a focus upon dilute concentration regions ($C = 10^{-5} \sim 10^{-1}$), where significant particle-turbulence interaction can be observed and inter-particle collisions can reasonably be neglected. Focus will also be placed upon a time during flow reversal, when the greatest adverse pressure gradient is encountered in the flow and the resulting instabilities and unsteadiness are evident enough to influence both the particle and the turbulence statistics.

In this dissertation, a sheet flow is generated in the UMD U-shaped water tunnel, which is driven by a piston in one of the end tanks connected by a test section of dimensions 375 cm (L) $\times 45\text{ cm}$ (H) $\times 30\text{ cm}$ (W). The bottom 15 cm is packed with well-sorted sand particles ($d = 240\ \mu\text{m}$), leaving the rest 30 cm for the flow. Sinusoidal external flow, with a nominal velocity profile of $U_f(t) = \sin(2\pi t/5)$, m/s , is prescribed to induce the effect of weak favorable/adverse pressure gradient (Sleath parameter, $S = 0.085$). Measurements are conducted near the static sediment bed

in the middle of the test-section (streamwise and spanwise directions). The cross-section of the test section is sufficiently large to contain a full spectrum of turbulence eddies encountered in the oscillatory sheet flow even after removing the boundary layer effects from the side walls. The thickness of the boundary layers generated on the smooth side walls, can be estimated as $40 \delta_s = 40 \sqrt{\nu T / \pi} = 5 \text{ cm}$ according to Salon et al. [69], beyond which the wall effects can be neglected, where δ_s is the Stokes layer thickness. The estimated boundary layer thickness on side walls is close to the measured value provided by Knowles [70] under a similar flow condition. The largest eddies encountered within the mobile bed layer under oscillatory sheet flows can be estimated as the thickness of the bottom boundary layer, which is around 10 cm under current experimental conditions. The length of the test section (375 cm) is also adequately long, more than twice of the full excursion length of the prescribed oscillatory flow (1.60 m), such that end effects can be avoided, i.e. the flow forced out of the end tanks can never get into the measurement location in the middle of the test section.

The proposed high-resolution, high-fidelity and concurrent PIV/PTV based measurement of both phases in sheet flows is very challenging. The degradation of lighting conditions caused by the scatter induced by the high-concentrations near the bed, in addition to the the obscuration among sediment particles and the huge disparity of signal intensities between phases cause significant troubles when directly applying the existing PIV/PTV based techniques to sheet flows, so a series of modifications based upon the existing PIV/PTV techniques have to be developed first. Chapters 2 and 3 are devoted to development of a novel measurement technique

to achieve these measurement goals, with a focus on the measurement of sediment particles and carrier phase flow respectively. In Chapter 2, a novel measurement technique was developed that is able to reliably reconstruct each sediment particle's 3D positions near the light sheet center based upon single snapshots recorded by multiple cameras from different perspectives. Based upon the reconstructed results, concentration profiles can be computed by specifying suitable measurement volume thickness. A Lagrangian particle tracking algorithm adapted from "shake-the-box" (Schanz et al. [1]) was also developed to compute the trajectories of each reconstructed sediment particle, enabling the study of sediment Lagrangian statistics. In Chapter 3, a novel apertured filter method was developed to enable the simultaneous measurement of the ambient carrier phase flow with a resolution of twice of particle's mean distance in the highest concentration of our interest ($C = 0.01$ corresponding to a particle mean distance of $\lambda_p = 3.7 d$). The cross-talk errors were evaluated and proved to be insignificant.

In Chapter 4, facilitated by the measurement techniques developed in Chapters 2 and 3, the whole field, phase-locked time-resolved, particle-resolved and concurrent measurements of both phases up to a concentration of 1% were conducted in the sinusoidal oscillatory sheet flow as prescribed above. Only the results obtained near flow reversal are demonstrated and analyzed.

At last in Chapter 5, possible contributions made by this dissertation is summarized, both in the measurement technique advancement and in the sediment transport studies, and future work is proposed.

Chapter 2: Measurement technique: sediment phase

In order to provide a whole-field, time-resolved, particle resolved and concurrent measurements of both the fluid and the sediment phase in dilute regime ($C \leq 1\%$) under oscillatory sheet flow conditions, PIV/PTV-based measurement is the most suitable choice that can satisfy all of the above requirements. In the time-resolved measurement, Lagrangian particle tracking (LPT) is naturally implemented to the sediment particles, which requires the following steps: 1) particle identification in each camera, 2) the establishment of stereoscopic correspondence and 3D reconstruction, and 3) particle tracking between consecutive frames. For the continuous carrier phase measurement, both LPT and PIV methods can be applied. In this thesis, laser light sheet is used for illumination, so only the sediment particles located close to the light sheet center are reconstructed and tracked and stereoscopic PIV is used for the measurement of carrier phase due to its superior reliability.

In a traditional PIV-based concurrent two-phase flow measurement, both the sediment particles and their surrounding flow (seeded with tracers) are illuminated by single or multiple light source(s) and together or separately filmed by multiple cameras. The simultaneously registered two phases are then discriminated either optically or digitally. The traditional PIV-based measurements confront many chal-

lenges when directly applied to sheet flows, such as the obscuration among sediment particles, the uncertainties associated with particle centroid determination, the reliable extraction of carrier phase velocities, to name a few. So innovative measurement techniques have to be developed to address the problems encountered by the measurement of each phase.

This chapter focus upon the measurement of sediment particles, which can be divided by two major parts. Part one (Section 2.1) deals with the 3D reconstruction of sediment particle locations based upon single snapshots of multiple cameras viewing from different perspectives, while part two (Section 2.2) introduces the Lagrangian particle tracking (LPT) algorithm, which tracks the temporal evolution of the 3D reconstructed positions associated with each target sediment particle given that the time-resolved multi-camera measurement is available.

2.1 3D reconstruction and concentration measurement

Section 2.1 presents a multi-camera method to reconstruct the instantaneous position of large dispersed phase particles in systems where the optical depth is of order $O(1)$, with a specific emphasis on problems in sediment transport. Although much work has been performed in multi-camera three-dimensional reconstruction methods, the majority of prior work has been focused on small tracer particles appropriate for single-phase PIV. The large ratio of the diameter of sediment particles to typical tracer particles (usually 10 to 100 times) gives sediment particles distinct image characteristics, which violates the assumptions made by most 3D reconstruc-

tion techniques in current use, and thus motivates us to develop a technique to accommodate the unique image signature of sediment particles. Inspired by the work of Maas et al. [71], Khalitov and Longmire [72], Spinewine et al. [73], Knowles and Kiger [74], this section of the dissertation introduces a multi-camera thin light sheet imaging method to accurately measure the dispersed phase concentration up to optical densities of close to $O(1)$. The work is an extension of a prior single camera method [74] that utilizes particle image characteristics to identify particles and, when appropriately calibrated, provide a measure of the effective measurement volume thickness. By introducing multiple camera perspectives, stereo photogrammetry methods [71, 73] can be combined with the particle image characteristics to provide 1) increased accuracy in determining individual particle locations, and 2) increased reliability in identifying all of the dispersed phase objects in the face of larger increased volume fraction. The method is calibrated through the use of a fixed solid/gel suspension test cell that mimics the optical properties of a solid/water suspension. The static arrangements of the particles allows for a repeatable volume scan of the cell. This is subsequently used to produce an accurate mapping of the particle locations within the test volume, which serves as the reference set for evaluating the performance of the new method. Comparisons are made over a range of volume fractions from $C = 1 \times 10^{-4}$ to $C = 1.2 \times 10^{-2}$ for a fixed spherical particle size of $D = 240 \mu m$. The new method is able to provide an accuracy of 2% up to a volume fraction of $C \approx 8 \times 10^{-3}$, which is an order of magnitude greater than the single-camera method used previously. Finally the proposed technique is applied to an oscillatory sheet flow to demonstrate its advantage over the standard 3D-PTV

and single camera methods.

2.1.1 Literature review and problem statement

One of the most challenging tasks confronted by multi-phase PIV/PTV measurements is to resolve the motion for each discrete dispersed phase particle, especially in high concentration regions. The ideal method would provide complete kinematics, including the three-dimensional (3D) position, velocity, acceleration and trajectory of the dispersed phase. This section focuses upon a methodology to reconstruct the instantaneous positions of sediment particles in the face of increased concentration, which serves as a pre-requisite step for successful concentration calculation and 3D kinematic statistics. In what follows, an overview of existing 3D particle tracking techniques is first reviewed, and then the proposed technique is introduced.

Three-dimensional tracking of tracer particles has been extensively studied in the past several decades due to the increased demands for improved spatial resolution and accuracy that can be provided by improved imaging systems[75]. The most critical procedure for robust 3D particle tracking is to reconstruct the instantaneous 3D location of every particle, utilizing the particle images viewed from different perspectives. This is a significant challenge for high seeding-density due to problems such as overlapping particles, occlusions and matching ambiguities (ghost occurrences) etc. In order to tackle these problems, additional information is typically incorporated and cross-referenced to achieve an optimized 3D particle reconstruc-

tion that is consistent with all independent inputs, such as the apparent position of the particle within images, their image characteristics on different cameras, as well as spatial and temporal coherence exhibited by the particles' motion.

One of the most popular early 3D PTV methods [71] used the particles' 2D positions within each image as input, and then constructed epipolar lines to establish stereoscopic correspondences. This method can generate accurate 3D particle positions under conditions of low seeding densities, on the order of 0.001 particles per pixel (ppp) using a four-camera configuration. Iterative particle reconstruction (IPR, Wieneke [76]) incorporated particle image characteristics to inspect the reconstructed results by iteratively comparing the original image with the back-projected image of the 3D reconstructed particles based upon a calibrated optical transfer function (OTF, Schanz et al. [77]). During each iteration, the intensity and position of each 3D reconstructed particle is adjusted independently and successively such that a minimal local residual is achieved. IPR is capable of resolving flows with seeding densities up to 0.05 ppp. Other examples that successfully incorporated particle image characteristics (particle size and intensity) into PTV technique can be found in the work of Mikheev and Zubtsov [78] and Cardwell et al. [79].

If a time-resolved image set is acquired, the temporal information can also be incorporated into the IPR process, which forms the fundamental idea of the "shake-the-box" (STB) method [1]. As an additional step in STB, long temporal particle tracks are searched and identified facilitating the 3D reconstruction process in two ways: 1) they serve as an additional inspection for validating the reconstructed particles and rejecting the ghost ones; and 2) the particle distribution in the subsequent

step can be predicted via extrapolation of the known trajectories, providing a largely pre-solved system *a priori* to application of the 3D reconstruction technique (IPR) and thus significantly reducing the required computational effort. With a 4-camera imaging system, particles with image density up to 0.125 ppp can be accurately reconstructed from noise-free synthetic images, while this number drops down to 0.075 ppp if synthetic noise is introduced. Other particle tracking algorithms that take into account the temporal coherence of the particle's motion include Nishino et al. [80], Malik et al. [81], Ouellette et al. [82] and Cierpka et al. [83]. Spatial coherence is another indicator that can be inspected when tracking the particles in the subsequent time step, which means that the pattern formed by a cluster of particles should only deform in a gradual way. Many particle tracking algorithms [73, 84, 85, 86, 87, 88] based upon cluster matching exist, which can also be potentially incorporated into the 3D reconstruction process and provide verification or correction for the reconstruction results.

The above 3D reconstruction techniques assume object images typical of tracer particles, which are characterized by their small size (often diffraction-limited images of sub-pixel light scatters, typically no more than 5 pixels on an image) and relatively small volume fraction (usually less than 10^{-6}). This section, however, is interested in dispersed multiphase flows and focuses upon the 3D reconstruction of sediment particles. In contrast to tracer particles, dispersed sediment particles are characterized by their large apparent sizes (100's of pixels of image area for centimeter-scale field of view) and large volumetric fraction (3 to 4 orders of magnitude higher than that of the tracers).

Extreme caution should be used when applying any of the preceding 3D reconstruction techniques directly to the sediment particles. First, large volume concentration in sediment flows implies that obscuration by neighboring particles would become more frequent. In order to guarantee the optical access to each sediment particle despite a high volume fraction, most of the optical-based granular flow measurements reported in the literature have been conducted in either a narrow channel [89, 90] or adjacent to a transparent solid wall [73]. Our interests, however, concern sediment transport under sheet flow condition with measurements performed in the middle of a 30 *cm* wide water tunnel, where these prior techniques will not function.

Second, most particle tracking methods, such as IPR or STB, rely heavily on the optical transfer function (OTF) to back-project the 3D reconstructed particles onto each camera. Unfortunately, the OTF is difficult to even roughly estimate for sediment particles. Tracers are normally diffraction-limited and can be represented by a Gaussian ellipse without loss of generality, so only a few parameters locally varying with space are sufficient to fit the OTF for each camera [77]. In contrast, the larger size of sediment particles, the internal inhomogeneities within sediment particles and variability in the local illumination conditions create a highly variable OTF under even moderate concentrations. As a consequence, in order to accurately calibrate the OTF for each sediment particle, the unique particle properties and the instantaneous volumetric concentration distribution in the flow have to be known *a priori*, which therefore renders the use of an OTF in sediment particle reconstruction impractical.

Third, the determination of a particle's true centroid location on each camera

is subjective and involves unavoidable uncertainties due to its large apparent size, irregular intensity distribution and sometimes incomplete imaging due to obscuration by its surrounding particles. As a result, a larger triangulation error has to be allowed during reconstruction, which would inevitably introduce an increased amount of ghost particles that need to be screened out carefully. This motivates us to develop a 3D particle reconstruction technique that is more readily adapted to larger particles at high volume fractions.

A brief review of the PIV/PTV techniques that specifically target multiphase flows is summarized below. The first challenge to conducting an accurate two-phase PIV measurement is being able to appropriately discriminate between dispersed phase objects (sediment particles for the current application) and other material suspended in the fluid (tracer particles, sediment fragments or other contaminants). Although many methods exist, they commonly can be categorized as separating the information optically, such as with fluorescently tagged particles: Poelma et al. [91]; from details of the particle image characteristics: Gui et al. [92], Kiger and Pan [93], Khalitov and Longmire [72], Knowles and Kiger [74]; or in the correlation plane/vector post-processing stage: Delnoij et al. [94], Deen et al. [95], Seol and Socolofsky [96]. After the dispersed phase is identified on each camera, 3D photogrammetry can be performed to reconstruct the particle 3D locations. Spinewine et al. [73] introduced Voronoi diagrams as a means to assist in both reducing the search area for stereoscopic matches and establishing a pattern-based tracking algorithm for each reconstructed particle. This method however, ignored each particle's unique image characteristics and only the particles' apparent positions are used

when establishing stereoscopic correspondences. Knowles and Kiger [74] used single camera (thus no 3D triangulation) and applied particle image characteristics (particle size and characteristic brightness) to estimate the particle’s relative position to the laser light sheet center, based upon which an effective measurement volume can be deduced, and the volumetric concentration calculated. This method can only work appropriately when the dispersed phase volume concentration is less than 0.1%. At higher concentrations, light scattering from dense sediment particles is so intense and irregular that the measurement volume can no longer be accurately correlated with the particles size and brightness criteria. Obscuration and overlapping of particles under high volumetric concentration represent additional problems that a single camera method cannot cope with.

To extend the work of Knowles and Kiger [74], we introduce a Multi-Camera Single-Plane imaging method (referred to as “MCSP method” below) as a means to provide a more precise and reliable determination of the dispersed phase 3D locations in the face of increased concentration. In this method, the particle image characteristics are incorporated into the 3D reconstruction process, though without having to calibrate an optical transfer function. In this work, a thin light sheet comparable to the one used in planar PIV (Gaussian intensity distribution with a thickness of $1 \sim 2\text{ mm}$) is used to illuminate the flow, constraining the imaging volume and alleviating the problem of both overlapping and obscuration in high concentration regions.

The new method is outlined in Sect. 2.1.2, describing the algorithm for a three-camera setup. In Sect. 2.1.3, details of a calibration method is described

that uses a static suspension test cell as a reference in order to validate the multi-camera discrimination algorithm. The study concludes with the application of the proposed technique to an oscillatory sheet flow. The measurement of the sediment concentration profile in the normal-to-bed direction is discussed and assessed.

2.1.2 Multi-camera, Single-plane method

The position of the cameras and the laser light sheet for the current work is shown in Figure 2.1, in which a randomly selected particle within the sediment-gel suspension is used as an example to schematically illustrate how a typical sediment particle behaves in terms of its characteristic brightness (defined as the average of the camera intensity reading over the region identified as a particle object) and apparent positions when it is translated through a laser light sheet. Camera 1 is looking perpendicular to the light sheet plane, while the other two cameras are placed with viewing angles approximately $\pm 150^\circ$ apart from camera 1, minimizing the chance that two neighboring particles would cause obscuration effects in all three camera images simultaneously. Though three cameras are used, the method could be readily generalized to four or more. All the cameras are calibrated first by registering the points on a planar calibration target translated to different lateral positions in the z -direction and then self-calibrated to coincide their $z = 0\text{ mm}$ planes to the light sheet center [97]. When reconstructing the 3D positions of the sediment particles, the phase separation algorithm developed by Khalitov and Longmire [72] is employed to separate the sediment particles from other non-sediment objects. The

2D locations, size and characteristic brightness of individual sediment particle identified on each camera are determined and recorded. Then a unique 3D triangulation procedure is implemented to reconstruct the 3D positions of the sediment particles described as follows. The raw images are dewarped onto the $z = 0\text{ mm}$ plane (light sheet center), and the resultant disparity in the particle's projected positions ("disparity vector") from different perspectives indicates its lateral offset relative to the light sheet center. Since the particle's image characteristics, including its size and characteristic brightness, are also correlated with its distance to the light sheet center (as explored by Knowles and Kiger [74]), this additional information is incorporated to effectively reduce the ambiguity when establishing the stereoscopic correspondences as confronted by standard 3D-PTV and increase the capability of resolving particles under much higher concentration. The obscuration problem can be further alleviated by successively utilizing different pairs of cameras during 3D reconstruction, since there is a greater chance that a particle being blocked in one camera can be detected by other cameras looking from different perspectives. Once all the sediment particle positions are determined, the concentration can be acquired directly by computing the volume (or number) of particles occupied within a prescribed measurement volume. More details in Figure 2.1, such as the particle image patterns at different depth locations and the secondary peak presented in the brightness curve in camera 3, will be discussed in Sect. 2.1.3.

To reliably identify particles and provide an estimate of their 3D positions, a multi-step particle-pairing algorithm based upon particle image cross-correlation is developed using the information from all three cameras, as outlined in Figure 2.2.

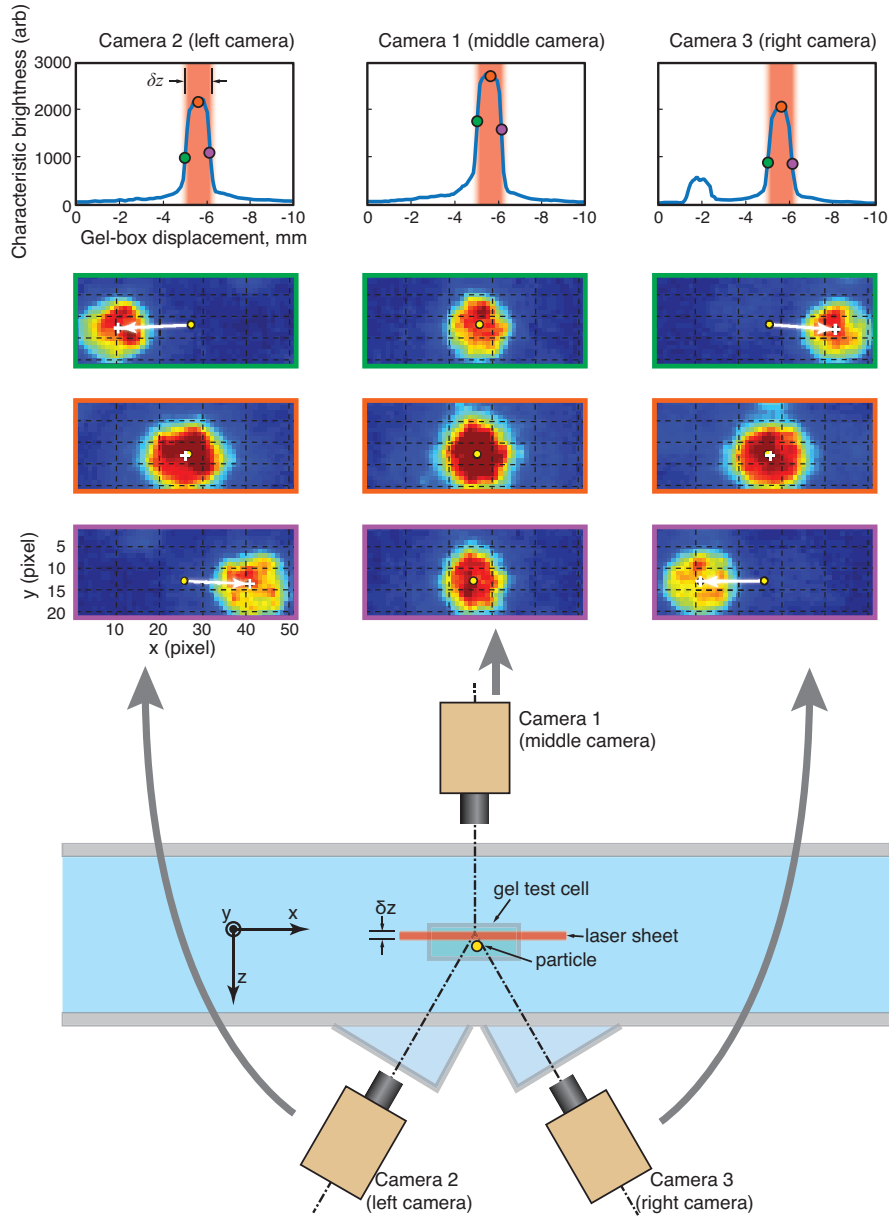


Figure 2.1: Experimental setup and images of a single particle (randomly selected in the gel sample with $C = 0.003$) as it is translated through the light sheet. Due to the oblique viewing angle of cameras 2 and 3, the particles appear to translate in the x -direction as the box is displaced along the z -axis. The difference in the apparent position from the actual position is referred to as the disparity vector (shown as white vector), and contains the information of z -position of the particle.

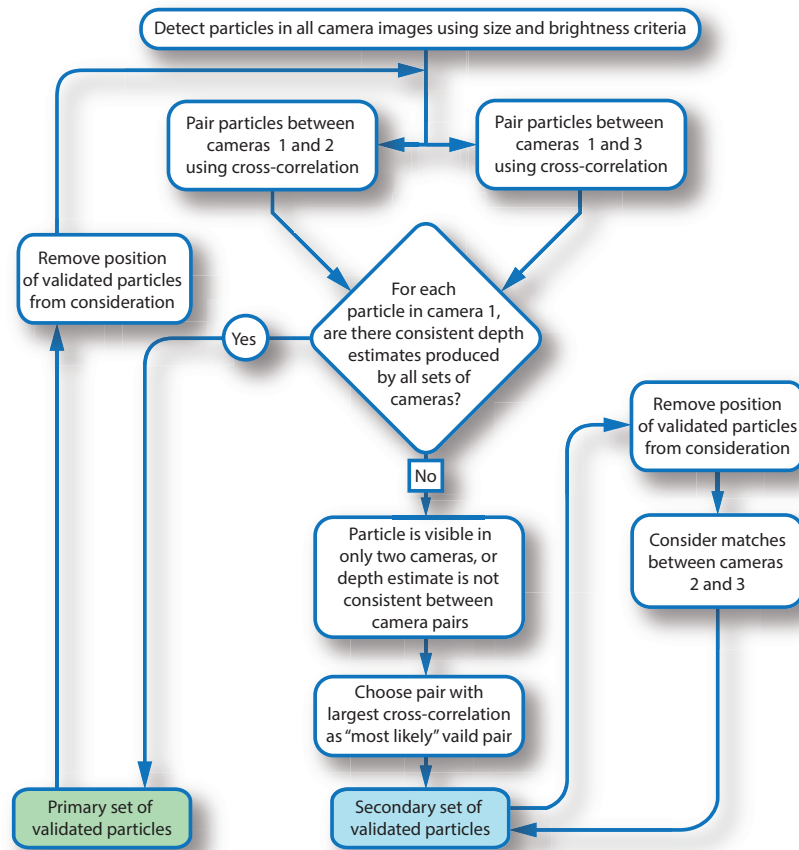


Figure 2.2: Logic diagram of 3D reconstruction routine for dispersed phase particles, using multi-camera images for single slice.

The fundamental premise is that the image from each camera provides the apparent xy -coordinates of individual particles, and the resulting disparity of the particle positions between any two image pairs conveys the z coordinate of the particle. Since only two perspectives are required to provide the depth information, the third camera (or more if additional cameras are used) can provide redundancy to improve the estimate or provide missing information when a particle is obscured from view of one of the cameras.

The process is started by identifying all particles within each camera image (after dewarped onto the $z = 0\text{ mm}$ plane) using the size and brightness method [72] to limit particles that are most likely close to the light sheet (limiting the maximum disparity that is possible between the 3 camera images). Once identified, a matching particle is sought in the other camera images by comparing the selected source particle to potential matching target particles that are located close to the corresponding epipolar line. The comparison is facilitated by limiting the search to a region based on the estimated light sheet thickness and size/brightness criteria used. This is initially conducted with a common reference camera (matching the particles between cameras 1 and 2, and then 1 and 3). In each camera pair, the quality of possible matches are quantified performing a cross-correlation between the source and target particle images, and the one with a maximum correlation value is selected as the suitable match. The disparity vector is calculated, and particles identified and paired on both image pairs should give consistent (x, y, z) positions. If confirmed, these particles are considered as validated ones and removed as candidates in subsequent stereoscopic matching. This process is iterated until

particles that can be validated by all 3 cameras are completely extracted. For those particles that do not have a match from the other pair of cameras, or do not have consistent disparity vectors computed from the two camera pairs, the pairings with the higher correlation value (no pairing means zero correlation value) are also treated as valid and included for 3D reconstruction. Finally, information from possible pairings between cameras 2 and 3 are calculated to account for particles that were not visible originally in camera 1.

2.1.3 Calibration Method: test cell and volume scanning method

To assist in the development of the proposed technique, a static dispersed phase test cell is used which closely mimics the optical conditions of a solid/water mixture, as used in our previous work [74]. The experimental setup is shown in Figure 2.1. A small box ($75 \times 50 \times 25 \text{ mm}^3$) was filled with an ethyl alcohol hydrogel (Purell hand sanitizer, index of refraction $n_f = 1.35$) and mixed with a known mass of sediment particles (soda lime glass spheres, specific gravity $s = 2.5$, index of refraction $n_p \sim 1.52$, average size of $d = 240 \mu\text{m}$ sorted using standard mesh sizes of 218 and $265 \mu\text{m}$, respectively). Five different mixtures were created with nominal target volume concentrations of $C = 1 \times 10^{-4}$, 8×10^{-4} , 3×10^{-3} , 6×10^{-3} and 1.2×10^{-2} . Three cameras were used in the positions shown (Phantom v640/641, Vision Research, 4-megapixel, 12 bit depth; Nikon Micro NIKKOR 105mm lens, $f_{\#} = 11$). After calibration (both camera calibration and self-calibration) of the cameras, the box was submerged in the test section, illuminated with a thin laser

light sheet ($\delta z \sim 1\text{mm}$ thickness), and images were simultaneously acquired on all three cameras. Following image acquisition, the box was translated $\delta z = 0.1\text{mm}$ in the direction perpendicular to the light sheet and the process was repeated. A total of 100 steps were used to generate a detailed rendering of a 10mm thick volume within the cell. The cameras and laser light sheet were fixed throughout the translation process. Figure 2.1 presents the images of a single particle at three different z -locations as it is translated through the light sheet and imaged by the three cameras. Note that due to the projection of the particle image in the oblique viewing directions (cameras 2 and 3), an apparent horizontal shift of the particle image is evident due to the particle’s z -distance from the focal plane. This shift from the actual (x, y) position is often referred to as a “disparity vector”, denoted by the white vectors in the figure, and can be used to determine the z -position of the particle.

Once the image data was acquired, the information from all of the images was used to reconstruct a “reference” data set. The reference set is used to validate the proposed technique, which is designed to extract information obtained from just a single image slice within the scanned volume. The reference set is constructed by first applying the size and brightness method [72] to identify all objects independently within the complete set (all image planes, all cameras). Then, starting with the first image plane in the set, each identified object is compared via cross-correlation to all possible objects identified within a region corresponding to the object’s expected position. For the viewing angles of cameras 2 and 3, this corresponds to an expected displacement of approximately $50\ \mu\text{m}$, or $0.2d$, giving a reliable means to associate

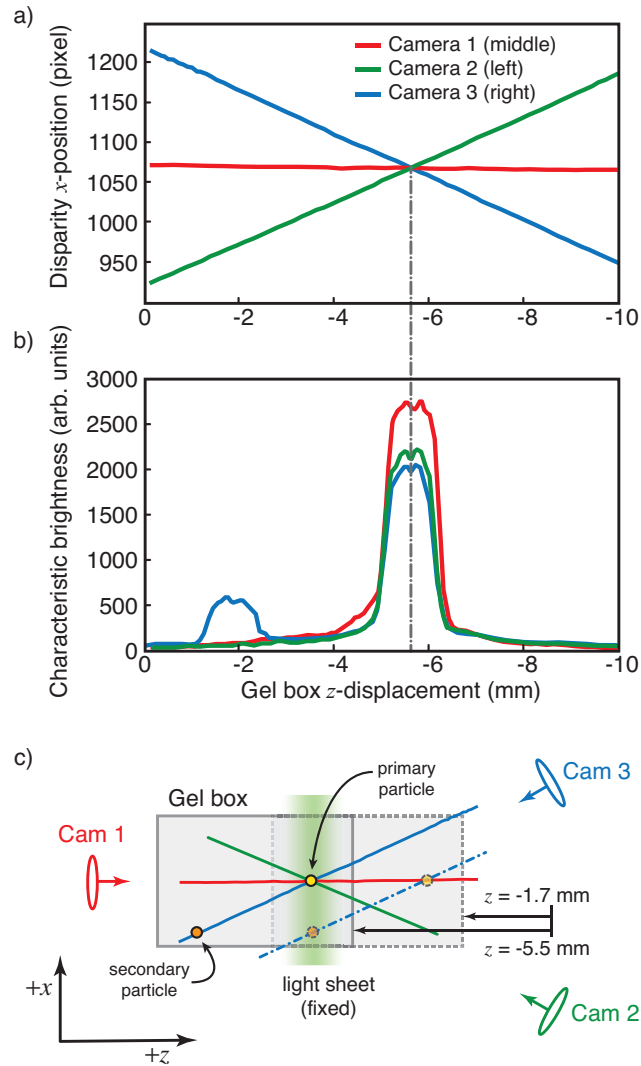


Figure 2.3: Apparent position and brightness of a single particle as viewed by the three cameras during the translation of the test cell.

the same particle throughout the entire sweep. The object in the subsequent frame with the highest correlation was selected as the most likely match. The process was then continued for the entire set, creating a “track” of the particle as the volume is swept through the light sheet. As new objects were identified, new particle tracks were created, and if existing objects had no identifiable continuation object, a track was terminated. To find the most reliable estimate of the particle locations, all of the tracks from the 3 cameras are overlaid, along with the corresponding characteristic brightness of the particles, as shown in Figure 2.3. The multiple tracks should all cross at the same point for a unique particle, with a maximum of the characteristic brightness value corresponding to when it was in the light sheet. Two criteria are used to identify a track as a dispersed particle: 1) the peak magnitude of the characteristic brightness and 2) the length of the track. For the current work, a minimum track length of 1 *mm* (11 planes) and peak characteristic brightness of 180 units were chosen to be the appropriate threshold (the sensor maximum is 4095 with a background noise level of approximately 15).

Ensuring 3 independent and complete tracks through the volume, however, was only reliably possible at low concentrations, and even then is still susceptible to the influence of what choice is made for the track length and brightness requirements to identify a particle. At the lowest concentration, 90% of the particles (80 in total) were identified in all three cameras. Many of the cases not identified in all three cameras had peak brightness values and/or track lengths near the threshold. While these objects could be identified in all three cameras if the thresholds were relaxed, it was found that spurious objects (dust particles in the gel, or even particle fragments)

Nominal Concentration, C (%)	0.01		0.08		0.3		0.6		1.2	
Reference Concentration, C_{ref} (%)	0.0098		0.082		0.31		0.60		0.93	
Camera Detection	# of particles	% of particles								
Three cameras (MLR)	72	90%	470	72%	1239	50%	1126	24%	1101	14%
Left & Right cameras (LR)	0	0%	40	6%	118	5%	408	9%	590	8%
Middle & Right cameras (MR)	1	1.3%	31	5%	224	9%	567	12%	749	10%
Middle & Left cameras (ML)	2	2.5%	44	7%	272	11%	634	13%	846	11%
Middle camera (M)	1	1.3%	18	3%	268	11%	666	14%	1334	17%
Right camera (R)	2	2.5%	27	4%	184	7%	676	14%	1520	20%
Left camera (L)	2	2.5%	19	3%	165	7%	657	14%	1521	20%
Total particles	80	100%	650	100%	2470	100%	4734	100%	7661	100%

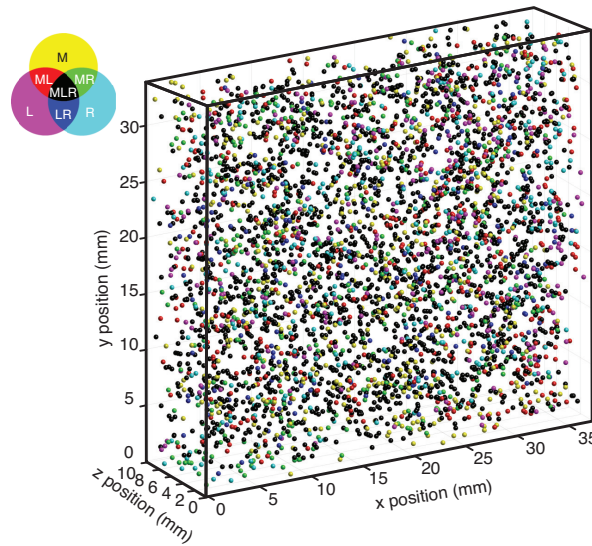


Figure 2.4: The breakdown of the percentage of particles identified by the various cameras during the volume-scan method is given in the table for all concentrations studied. The reference concentration, C_{ref} , represents the concentration spatially averaged over the full scanning volume (10 mm thick). The position of dispersed phase particles as determined using the full scan procedure is shown for $C = 0.003$.

were also starting to be accepted. Clearly, performing carefully controlled tests to assist in selecting the appropriate limits should be performed for reliable particle identification.

As the volume fraction increases, obscuration events and background light contamination caused by other particles begins to play a significant role in interrupting the continuation of the tracks. The secondary peak visible in Figure 2.3(b) (characteristic brightness ~ 600 , $z \sim -2\text{ mm}$) in camera 3 is the result of a secondary particle located just behind the line-of-sight of the primary particle and erroneously being identified as the continuation of the primary particle trace as it is moved out of the light sheet. The apparent positions of the two particles are too close for their combined signals to be separated from this camera's perspective, even though their actual 3D positions are far apart (about 15 particle diameters along the line-of-sight). The actual locations of the two particles in the x-z plane were drawn to scale in Figure 2.3(c), with the secondary particle being blocked by the primary one in camera 3, resulting in a significantly lower brightness peak. When conducting the volume-scan measurement, a single-peak-finding algorithm is applied to the brightness tracks in each camera and only the primary peaks are recognized and used to identify the associated particles to determine their 3D locations. As a result, for cases presented for the brightness track in camera 3 in Figure 2.3(b), the secondary peak is omitted and no track corresponding to the secondary particle is registered in this camera. However, the secondary particle can still be accounted for as long as it forms a detectable track in camera 1 and/or camera 2, meaning that it is not occluded by other particles from the perspective of at least one of the remaining two

cameras. In the table of Figure 2.4, a comparison of the reference concentration, C_{ref} , with the nominal concentration, C , indicates that having a particle obscured by neighboring particles in all three cameras is an extremely rare occurrence for $C < 0.6\%$, but becomes significant for the given viewing conditions at the concentrations higher than 1%. At the highest concentration studied ($C = 1.2\%$), only 14% of the particles were successfully identified simultaneously in all three cameras.

To circumvent this problem, estimates were also made with information given by the intersection of only two tracks (using combination of two different cameras), and finally by selecting the brightest points along tracks distinctly visible by only one camera. The positions of the resulting detected particles for a single concentration ($C = 3 \times 10^{-3}$) are shown in Figure 2.4. Calculating the concentration using the particle positions within the full scanning volume (10 mm thick) gives the measured reference concentrations, C_{ref} , reported in the table in Figure 2.4. With the exception of the largest concentration, the measured values are within 3% of the target values, which compares within the expected uncertainty in preparing the gel mixtures based upon the mass of particles added to the original gel (conservatively $\pm 3\%$ to $\pm 10\%$, depending on the mass of particles added, with the greatest uncertainty at the lowest concentration). The largest concentration underestimates the nominal value by nearly 20%. We believe that this is due to the significant obscuration effects that are present under these conditions, as will be discussed further below.

A further check of the mixtures is made by examining the spatial homogeneity, as shown in Figure 2.5. Here the concentration (C_{VS}) is measured using a sliding average subvolume that is $\Delta z = 3.2 \text{ mm}$ thick. This value is selected to minimize

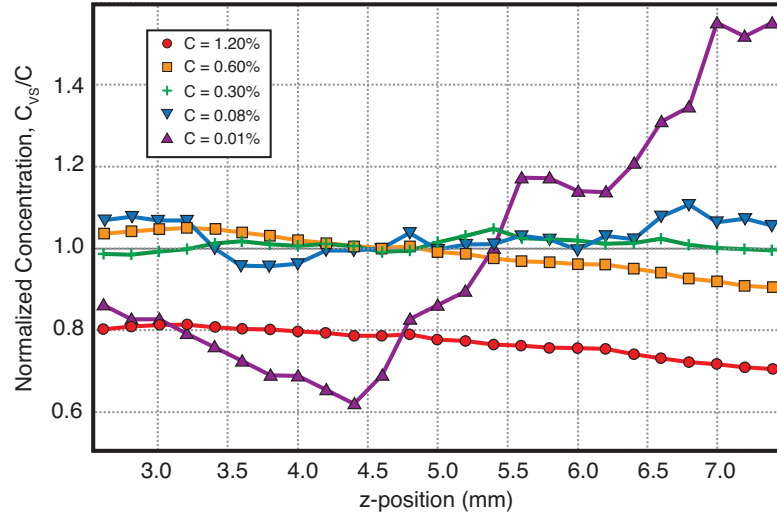


Figure 2.5: Concentration profiles calculated across the depth (z -direction) of the test cell. The individual values are calculated using a 3.2 mm thick volume at each point to allow sufficient particles for a converged estimate.

noise due to lack of statistical convergence while still allowing for some spatial resolution. All except for the lowest concentration case show a spatial variation within $\pm 10\%$. For $C = 0.08\%$ and 0.3% , the variation appears random, while for $C = 0.60\%$ and 1.20% , a distinct bias is noted as one moves across the test cell. The bias in the larger concentrations is thought to be a manifestation of the obscuration effects, particularly as the left and right cameras have a greater distance to view through the mixture as the z -position is increased. This will degrade the quality of the images in these two cameras preferentially over the middle camera, resulting a decreased ability to appropriately identify the particles. For the lowest concentration, the volume does not seem to be as uniformly mixed as the other conditions, with variations of up to $\pm 50\%$ of the total volume average.

The concentration calculated from a single plane (MCSP method, denoted as C_{MCSP}) is compared to that of the more accurate reference scan method for the

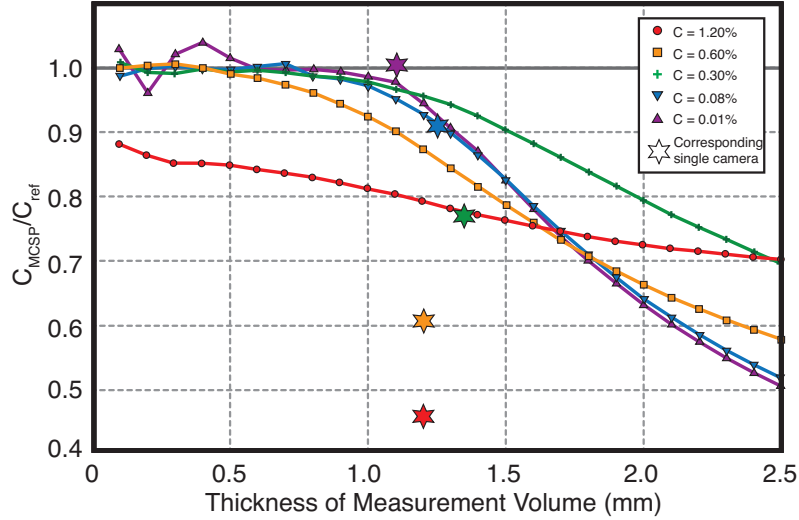


Figure 2.6: Concentration measured using the multi-camera single-plane method (C_{MCSP}) as compared to the volume-scan result (C_{ref}). Note that the nominal concentration value (C) is used for C_{ref} for the highest concentration, due to the underestimate of the volume-scan result. Corresponding measurements of the concentration provided by the standard single-camera method are indicated by the star (★).

various concentrations and a range of measurement volume thicknesses, as shown in Figure 2.6. Since the z -coordinates of the identified particles are known, the volume for the concentration calculation can be varied and precisely defined. The MCSP method is shown to provide an accuracy within 2% of the volume-scan measurement, provided the measurement volume thickness is limited to a range of 0.5 to 1 mm and the volume fraction is less than 1%. Beyond these limits, the method starts to systematically underestimate the true concentration, dropping more rapidly as the averaging volume thickness is increased for the very low concentrations, and more gradually at the higher concentrations. The roll-off point generally moves to smaller thicknesses with increased concentration, indicating that a reduced thickness for the averaging volume is required as the concentration is increased. At some value above $C = 0.6\%$, all values of the selected measurement volume thickness underestimate

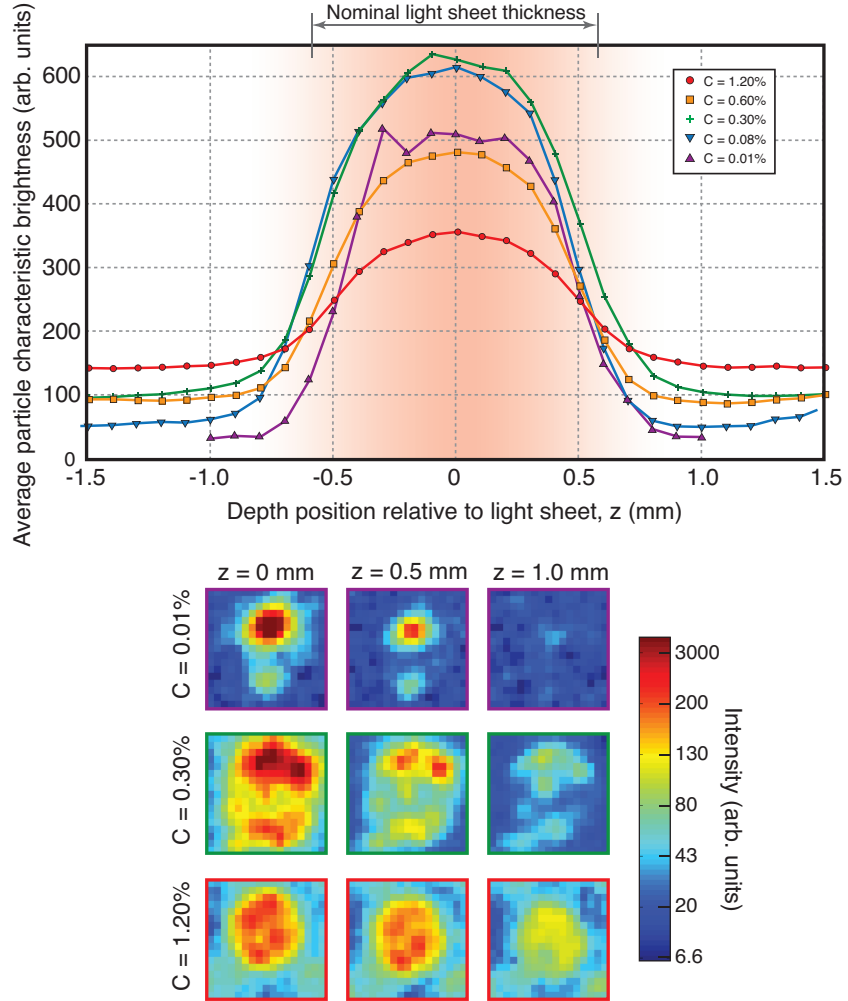


Figure 2.7: Ensemble mean of particle's characteristic brightness profile within the center of the test cell for all concentrations tested [Upper], and extracted typical images of particles at 3 concentrations and 3 different positions relative to the center of the light sheet [Lower].

the concentration, consistent with the volume-scan method used to provide the reference measure of the concentration.

The fact that there is an intermediate concentration where the thickness of the valid measurement region is actually increased over the baseline lower concentration cases is interesting and not immediately obvious (see the green line for thickness values greater than 1.2 mm in Figure 2.6 corresponding to $C = 0.3\%$ in comparison

to the concentrations higher and lower, respectively), as one would expect the gradual increase in obscuration effects to produce a gradual decay in the zone available for valid measurement. To investigate, the average characteristic brightness of the particles along tracks from the middle camera are shown for the different concentrations in Figure 2.7, along with images of representative particles within the center ($z = 0 \text{ mm}$), edge ($z = 0.5 \text{ mm}$) and outside ($z = 1 \text{ mm}$) the light sheet. From this information, it is noted that the peak brightness of the particles initially increases with concentration, with a maximum at $C = 0.3\%$, and then decays, while outside the nominal light sheet, the average particle characteristic brightness increases approximately monotonically with concentration. From the typical particle images, this can be seen to result from a shift in the illumination pattern in the particles as the concentration is increased. At the lowest concentration ($C = 0.01\%$), where the neighboring particles are far away (average particle spacing, $\lambda_p = (\pi/6C)^{1/3} \approx 20$ diameters), the only effective illumination comes from the light sheet, producing a relatively small intense region on the upper surface of the particle due to reflection, and a dimmer spot due to internal refraction and inhomogeneities within the particle on the lower surface. Once the particle is outside the light sheet, it is no longer readily visible. At the intermediate concentration, ($C = 0.3\%$, $\lambda_p \approx 6$ diameters), multiply-scattered light from neighboring particles increases the visible cross-section of the particle when inside the light sheet, even though overall light intensity incident from the sheet is reduced. Outside the light sheet, there is sufficient scattered light available to keep the particle visible in the image. At the highest concentration ($C = 1.20\%$, $\lambda_p \approx 3.5$ diameters), the particles appear as a nearly uniform intensity

across their projected area with only a gradual decay in intensity as one moves from inside to outside the nominal light sheet. The early increase in the visibility of the particle due to scattered illumination from neighboring particles is what is speculated to be responsible for the initial increase in the region of valid concentration measurement depth. As obscuration effects become more pronounced at the higher concentrations, the particles become more challenging to detect, and the region of valid measurement depth is decreased.

A comparison is made in Figure 2.6 between the MCSP method and the single-camera method used in earlier work [74]. In the single-camera method, the profiles of average particle characteristic brightness shown in Figure 2.7 are used to determine the effective measurement volume thickness. This had been previously shown to be effective up to volume fractions of $C = 8 \times 10^{-4}$, and the current work verifies this result with a 10% underestimate of true value at this concentration, and a less than 2% error at smaller volume fractions. As the volume fraction is increased, however, even accounting for the appropriate thickness does not compensate for the increasing number of particles that are lost due to obscuration effects, and by a volume fraction approaching $C \sim 0.01$, the single camera technique is only able to capture half of the valid particles. The multi-camera method is able to extend the range of accurate measurable concentration by an order of magnitude over the prior state-of-the-art.

The uncertainties in the reconstructed particle positions (by triangulation) mainly originate from the inevitable uncertainty in consistently identifying the particle's 2D intensity centroid, due to the irregular and variable particle image pat-

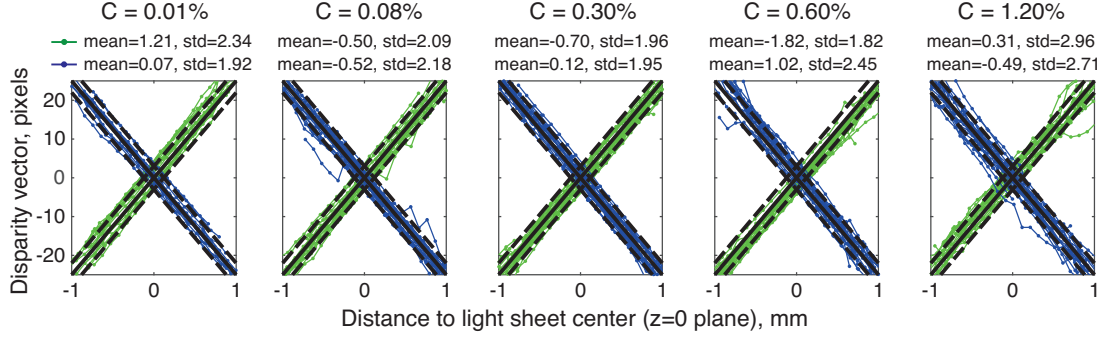


Figure 2.8: Particles' disparity vectors (x -component) as a function of their distance to light sheet center plane ($z = 0 \text{ mm}$) for different volumetric fractions, with green lines indicating disparity vector between cameras 1&2 and blue lines between cameras 1&3. The solid line denotes the calibrated/true disparity vector which a particle is supposed to have based upon its depth location and the mapping function (after camera calibration and self-calibration); and the dashed lines shows an error bound of ± 3 pixels. The mean and standard deviation of disparity vector errors (in pixels) of all the points in the figure are computed and displayed above each plot.

terms resulting from nonuniform illumination from the laser sheet and scattered light within the local environment. In order to quantify the reconstruction error, a detailed and comprehensive analysis of the particles' disparity vectors (x -component) as a function of their distance to the light sheet center ($z = 0 \text{ mm}$ plane) under the 5 volumetric fractions is presented in Figure 2.8. Each green (blue) curve represents how the measured disparity vector between cameras 1 and 2(3) of an identified particle changes as it moves away from light sheet center, whereas the black solid line denotes the calibrated/true disparity vector which the particle is supposed to have based upon its depth location (determined by Gaussian fit of brightness tracks) and the mapping function (after camera calibration and self-calibration). The dashed lines show an error bound of ± 3 pixels around the true disparity vectors. Only particles within a narrow region in the x - y plane were drawn to constrain the number of lines (around 20) for better illustration, noting that all other regions show simi-

lar results. In Figure 2.8, visual inspection of each green and blue line shows that under valid concentration measurement range ($C \leq 0.6\%$), all the lines manifest a linear relationship with mostly only sub-pixel deviations as a result of the consistent particle centroid determination algorithm developed by Khalitov and Longmire [72]. Figure 2.8 also shows that more than 90% of all the points lie within the error bound and have disparity vector errors of less than 3 pixels, which are distributed randomly and don't show a trend with their distance to light sheet center ($C \leq 0.6\%$). The disparity vector error bound can then be used to estimate the particles' 3D reconstruction error independent of particles concentration ($C \leq 0.6\%$) and location ($\pm 1 \text{ mm}$ of light sheet center), and it leads to an uncertainty in particles' 3D reconstructed locations of about 50% of the particle diameter (0.12 mm) in z - location and 20% of the particle diameter (0.067 mm) in x - and y - directions. The disparity vectors in the highest concentration ($C = 1.2\%$) exhibit generally similar trends, with the exception of an increased number of outliers, i.e., the zig-zag shape of the lines and the points outside the error bounds, which are mainly caused by the more frequent overlapping and obscuration occurrences by surrounding particles that shift the identified particle's apparent locations.

As a final note, the reader should be cautioned that our results are specific to our given optical conditions, though we propose below that the primary variables to be maintained for extension to other conditions are the light sheet thickness to particle diameter ratio and the optical depth for the imaging cameras.

The first influencing factor is the ratio between the nominal light sheet thickness and the particle diameter ($\delta z/d$). For the current study, a typical Stereo PIV

laser sheet with a nominal thickness of $\delta z = 1 \sim 2 \text{ mm}$ was used along with sediment particles with a mean diameter of $d = 240 \mu\text{m}$, resulting in a ratio around 5. One of the prerequisites for the successful application of the proposed technique is the ability to identify each discrete particle in each camera and determine their 2D centroid locations with tolerable accuracies in a consistent manner. With $\delta z/d \gg 1$, i.e. most visible particles are fully immersed in the light sheet thickness, similar particle image characteristics as those depicted in the current study would be expected and thus the proposed technique and algorithms currently being used should still remain functional. However, if $\delta z/d \ll 1$, meaning that the light sheet is incident upon only a fraction of each particle, this would fundamentally change the illumination and lead to a radical change in the resultant particle image characteristics and likely greatly disrupt the particle identification algorithm [72]. Moreover, even when a particle is correctly identified, its apparent position in each camera can be strongly biased by the specific location where the incident light strikes on the particle, which can induce systematic errors in the disparity vector and the reconstructed position. So in order to reliably implement the proposed technique for the measurement of much larger particles, it is recommended to keep the ratio, $\delta z/d$, above some pre-defined threshold by thickening the light sheet. For instance, if the particles were increased by a factor of 5 from the current conditions, thickening the light sheet by the same ratio would preserve the illumination characteristics. It is worth noting that for a fixed volumetric fraction, the particle number density is inversely proportional to the third power of the particle diameter. As a result, proportionally thickening the light sheet thickness and image viewing area according to the parti-

cle diameter will theoretically guarantee an unchanged particle image density (ppp , particles per pixel) in each camera. Similar overlapping and obscuration situations are anticipated in each camera and the proposed measurable volumetric fraction (1%) can still be achieved, albeit at the cost of sacrificed spatial resolution.

The second influencing factor is the optical depth through which the light sheet propagates and through which the particles are viewed by the respective cameras. For our test cell, the light scattered from the focal plane had to travel through a distance of 7.5 to 20 mm , depending on the camera and positioning of the test cell. If one were to change the particle size or viewing distance through the mixture, then the limits of the valid concentration range would likely change. As an observation, the optical depth, $l = 4/\pi d^2 N = 2d/3C$ (where d is the particle diameter, N is the number density and C is the volume fraction), at our highest accurate concentration measurement ($C = 0.006$) is approximately 26 mm . This is roughly twice the average viewing distance (L) to the focal plane, indicating that we are well into the multi-scattering conditions with our observations. It is speculated that using a normalized optical depth (L/l) of unity as a reference measure for the upper limit of valid measurement may be a reasonable means to extend the results of the current work to other experimental conditions (particle size and viewing depth).

2.1.4 Application to experimental data

The proposed multi-camera single-plane (MCSP) method has been applied to a sinusoidal oscillating sheet flow, with a maximum free stream velocity magnitude

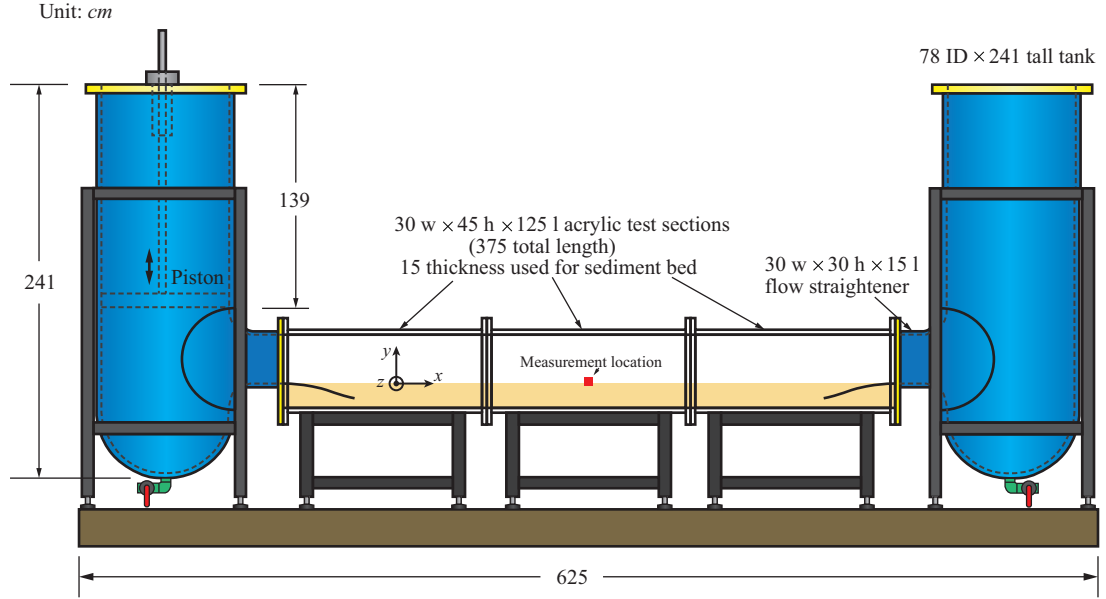


Figure 2.9: The U-shaped water tunnel. The red box shows roughly the measurement location and area. The coordinate system is shown in the figure, with $y = 0$ corresponding to the undisturbed bed level before the experiment started and the $z = 0$ plane coinciding the center of the light sheet.

of 1 m/s and a period of 5 s . The important dimensions of the U-shaped water tunnel utilized to generate the desired flow condition are shown in Figure 2.9. Three cameras were used to simultaneously register the images of both the tracer particles and the suspended sediment particles illuminated by the same laser light sheet (Photonics Industries, DM60-527). Figure 2.10 illustrates the orientation of the laser light sheet and the cameras, where the cameras were tilted downwards in order to reduce the optical depth (L/l) and gain better optical access to the sediment particles approaching the bottom of the bed. The cameras were equipped with 105 mm Nikon lenses, using $f_{\#} = 22$. The laser light sheet thickness was kept $1 \sim 2\text{ mm}$ within the measurement region, however the effective illuminating thickness was wider than that due to the intense scatter of light from the sediment bed and the suspended sediment particles during experiment. Prisms were placed between

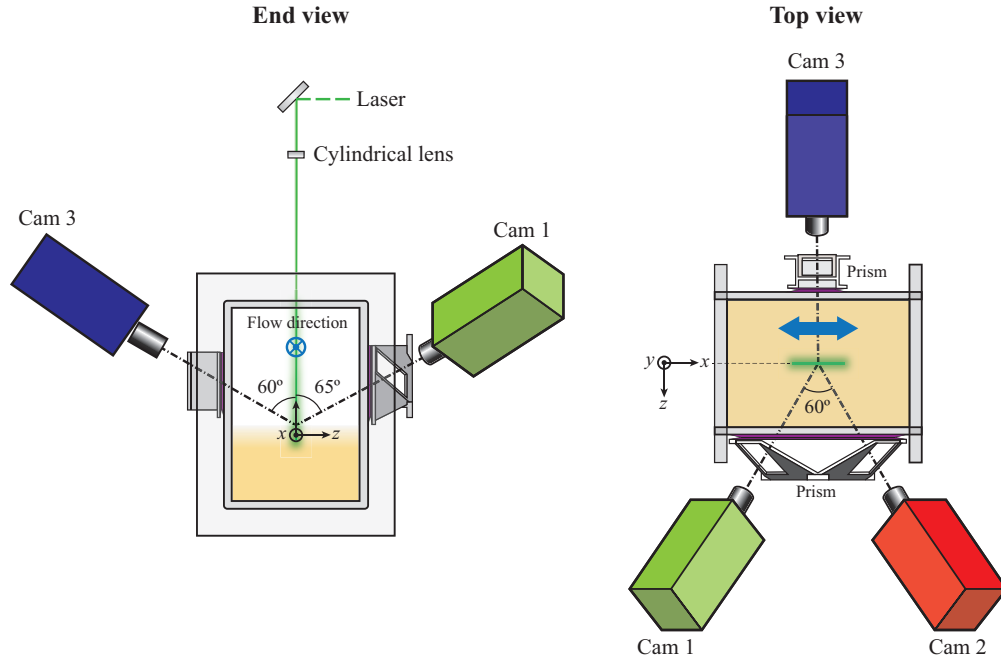


Figure 2.10: The cameras and laser configuration.

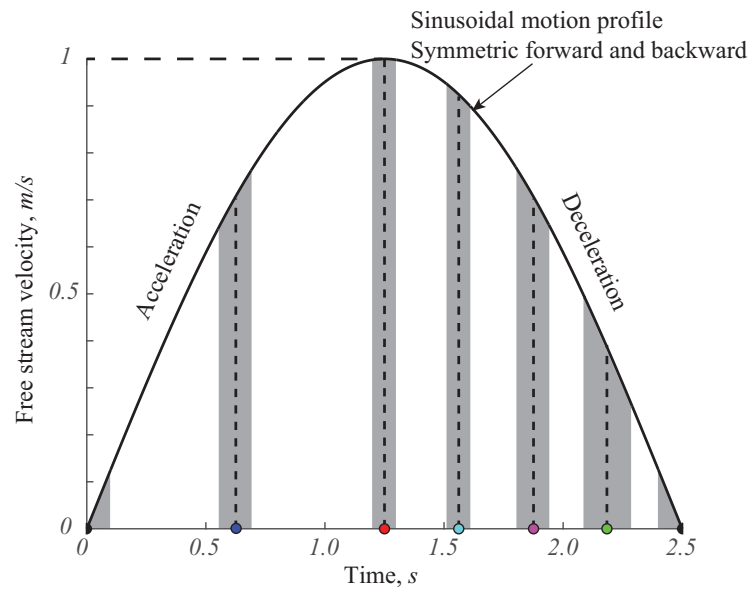
the cameras and the test section to allow the cameras to view perpendicular to the air/glass interfaces and alleviate the effect of astigmatism. The sediment particles were consistent with the ones used for developing the technique.

The measurement was performed in the middle of the test section, as shown in Figure 2.9 and 2.10, to avoid the side-wall and end effects. An effective measurement area of roughly $50\text{ mm} \times 50\text{ mm}$ spanned in the x - and y - direction respectively was achieved after the images were dewarped and only the overlapping region was taken into account, resulting in an in-plane resolution of 0.035 mm/pixel . The out-of-plane resolution, depending upon the camera configuration, for the current set-up (Figure 2.10) is 0.028 mm/pixel , meaning that a disparity vector of length 1 pixel corresponds to a 0.028 mm displacement in the depth location. The bottom of the effective measurement region was placed approximately 10 mm below the

undisturbed sediment bed level so that it could cover a full range of concentration variation in the normal-to-bed direction (from zero approaching the free stream to close-packed in the non-mobile region) at every moment in the cycle.

Time resolved measurements were performed at 6 different phases of the oscillatory motion, as shown in Figure 2.11. More frequent samples were conducted during the deceleration phase ($1.25s < t < 2.5s$), in consideration that the adverse pressure experienced during deceleration will generate more turbulence and hence is likely of greater interest. A high-speed time series of 201 images was acquired at each phase region measured, with different imaging frequencies being used to accommodate the corresponding speed of the flow while limiting the particle displacement to around 15 pixels. This results in different image acquisition duration at different phases, as shown in the shaded area in Figure 2.11. Each phase-lock measurement was replicated 70 cycles to converge the statistics. Note that with the proposed technique, a time resolved measurement is redundant and thus only the 101st image has been extracted at each phase per cycle and utilized for reconstructing the instantaneous 3D positions of the sediment particles.

The proposed technique (MCSP) was implemented to reconstruct the sediment particle distribution for each extracted image independently, from which the instantaneous normal-to-bed concentration profile could be computed. The flow is assumed to be statistically homogeneous in both the streamwise (x -axis) and spanwise (z -axis) direction. A binning size of 1 mm , with no overlap, in the bed-normal direction (y -axis) was used when calculating the concentration at each elevation. The effective measurement volume thickness (in z -direction) was set to vary linearly



Time resolved measurement at each specified phase

- Phase, 0° or 180° Imaging frequency, 1000 Hz # of images acq per cycle, 201
- Phase, 45° Imaging frequency, 1450 Hz # of images acq per cycle, 201
- Phase, 90° Imaging frequency, 2000 Hz # of images acq per cycle, 201
- Phase, 113° Imaging frequency, 2000 Hz # of images acq per cycle, 201
- Phase, 135° Imaging frequency, 1450 Hz # of images acq per cycle, 201
- Phase, 158° Imaging frequency, 1000 Hz # of images acq per cycle, 201

Figure 2.11: Data acquisition at 6 different phases displayed in only half a cycle, the other half has an identical velocity profile but with reversed velocity direction. The shaded area shows the duration for each phase lock measurement. The free stream velocity can be expressed as $U_f(t) = \sin(2\pi t/5), m/s$.

from 0.4 mm at the bottom of the bed to 1.6 mm in the dilute region. The thinner measurement volume being applied towards the bed can accommodate the higher concentration in that region, while a thicker volume in the dilute region can include more reconstructed particles and expedite the convergence of statistics. The specific value of the thickness being used is insensitive to the resultant concentration profiles. Finally, the instantaneous concentration profiles were phase averaged over the 70 independent cycles. Different measurement volume thickness has been tested (ranging from 0.2 mm to 0.8 mm on the bottom and from 1.2 mm to 2.0 mm on the top) and only a 2% variance in the averaged concentration profile was observed.

Figure 2.12 presents the phase averaged concentration profiles along the bed-normal direction measured at the 6 different phases depicted in Figure 2.11. Note that $y = 0\text{ cm}$ corresponds to the undisturbed bed level before the experiment started. Only the dilute regime, corresponding to a mass loading (ϕ_m) of $0.1\text{ g/l} \sim 50\text{ g/l}$, or a volume concentration (ϕ_v) of $0.004\% \sim 2\%$, has been demonstrated, which falls in the robust working range of the proposed 3D reconstruction technique (MCSP). Qualitatively different sediment behavior is discerned between the upper dilute region ($y > 13\text{ mm}$) and the lower dilute region ($y < 8\text{ mm}$). In the upper dilute region, a straight line can be fit to the concentration profiles at each phase, indicating a negative power law function distribution (Rouse's profile); while the curve rolls off in the lower dilute region.

A rough estimate of the time averaged concentration profile is obtained by averaging the concentration profiles at four different phases (0° , 45° , 90° and 135°), shown as the dashed line in Figure 2.12. The first comparison is made to the mea-

surement conducted by Ribberink and Al-Salem [98], in which irregular shaped sand particles and asymmetric oscillatory flows were used to generate sheet flows. They utilized a transverse aspirating sampler system to acquire the sediment concentration profiles and discovered that their data exhibited a universal slope of -2.1 (within the measurement range $0.1 \text{ g/l} \sim 10 \text{ g/l}$) occurred over a broad range of flow conditions, denoted as the thick solid line. The large disparity between the slope rendered in our measurement ($\alpha \approx -4$ in upper dilute region) and the one proposed by Ribberink and Al-Salem [98] can likely be ascribed to 1) the deficiency of phase angles (only four) used in the current study to compute the time averaged concentration profile, and 2) the difference in the sediment and flow conditions, i.e. spherical sediment particles are used and no velocity skewness is involved in the present study as opposed to Ribberink and Al-Salem [98]. It should be mentioned that in the upper dilute region, where there are fewer sediment particles and detailed visual inspection is possible, the 3D reconstructed sediment particles are back-projected to the raw images for cross-validation between cameras and a reliable 3D reconstruction result is visually confirmed. Our measurement agrees better with the results measured by Horikawa et al. [99] under a similar sediment and flow condition (exp # 1 – 2), as shown by the dash-dotted line. Horikawa et al. [99] also used a particle counting technique by securing a 1 mm thick black panel inside the tunnel offset 1 cm from the side wall and registering all the particles confined between the transparent side wall and the panel by a motor-driven camera. A similar trend to our data is observed, with $\alpha \approx -4$ in the upper dilute region with the curve rolling off towards the bed. The underestimate of concentration in the lower dilute region by Horikawa

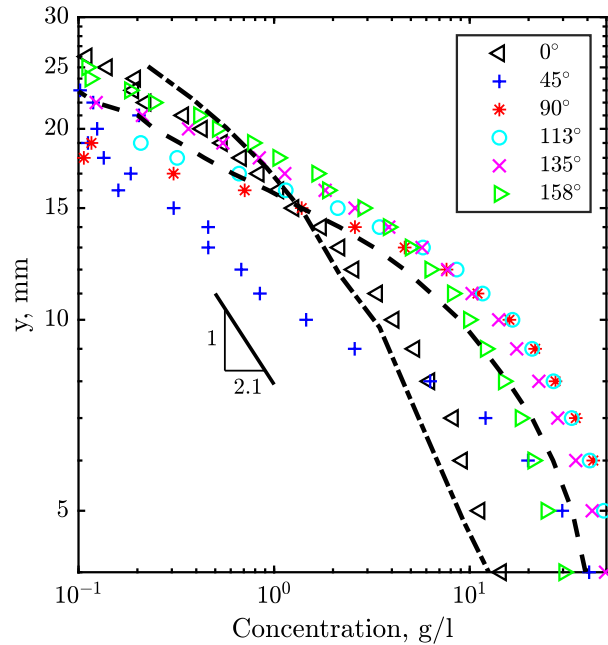


Figure 2.12: The log-log plot of the phase averaged concentration profiles measured at 6 different phases. The dashed line shows the time averaged concentration profile by averaging the concentration profiles at four phases (0° , 45° , 90° and 135°), the dash-dotted line displays the time averaged concentration profile acquired by Horikawa et al. [99] under a similar sediment and flow condition, and the thick solid line denotes the $\alpha = -2.1$ slope discovered by Ribberink and Al-Salem [98] collapsed by a broad range of flow conditions.

et al. [99] can be explained by the obscuration effects that occur at higher optical densities, for which our MCSP method was explicitly developed to address.

The proposed MCSP method is compared with two other planar imaging methods as shown in Figure 2.13, including the standard 3D-PTV method based upon the work of Maas et al. [71] and the single camera method based upon the work of Knowles and Kiger [74]. The exact same data set has been used when reconstructing the particle distribution by standard 3D-PTV method, where consistent particle triplets have been searched based only on their apparent 2D positions in the three cameras to establish stereoscopic correspondences. Only the particles detected on

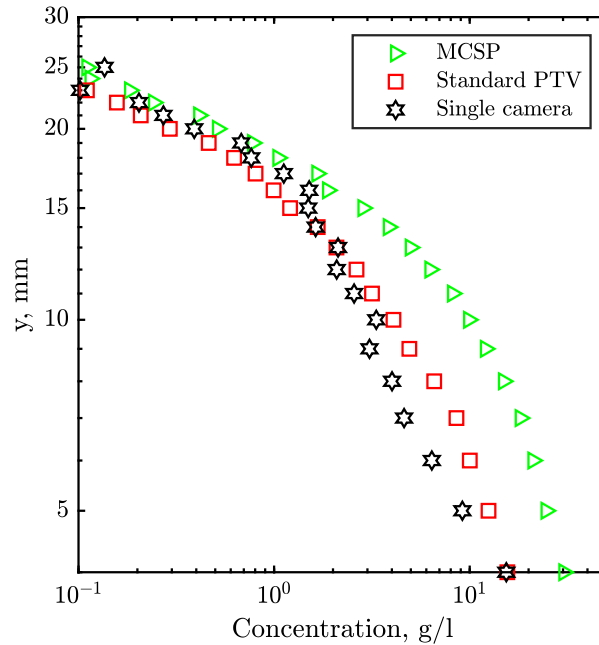


Figure 2.13: The log-log plot of the phase averaged concentration profiles at phase 158° , measured by three different methods.

all the three cameras are reconstructed and a large triangulation error of 4 pixels has been used due to the uncertainties in the determination of the centroid locations of sediment particles in each camera as discussed in Sect. 2.1.3. When applying the single camera method, only the images acquired by the middle camera have been used and the size and brightness criteria used for particle identification, which is correlated with the specified measurement volume thickness, has been determined by inspecting the average particle image characteristics near the light sheet. Figure 2.13 displays the concentration profiles at phase 158° obtained by the three different methods. Only one phase of data is presented for clarity and the comparisons are qualitatively the same for all other phases. It can be seen that in the upper dilute region, the concentration profiles calculated by all three methods collapse on each other; while the standard 3D-PTV method and the single camera

method underestimate the sediment concentration in lower dilute region. The standard 3D-PTV method of Maas et al. [71] requires the particles to be seen on all the three cameras, so its underestimation is mostly due to more frequent obscuration of sediment particles towards the bed. The irregular variations observed in the single camera measurement implies lack of statistical convergence, which originated from the significant uncertainties associated with correlating a particle's depth position to its size and brightness features. The success of the single camera method relies heavily on this correlation, which is prone to error under complex lighting conditions due to strong particle scattering and bed reflections near the bed. The IPR and STB methods are not selected for comparison due to their strong dependence upon the optical transfer function (OTF) during reconstruction, which cannot be calibrated for sediment particles. More discussions on this can refer to Sect. 2.1.1.

2.1.5 Summary

A novel 3D reconstruction technique suitable for sediment particles has been introduced and tested. The essence of this technique is 1) to utilize a thin illuminating light sheet to constrain the measurement thickness and alleviate the obscuration between particles and 2) to make the full use of the particles' image characteristics to reduce the ambiguities when creating stereoscopic correspondences and resolve more sediment particles when occlusion starts to affect. In order to test its validity, a static suspension test cell was constructed, with uniformly mixed sediment particles of volume fractions ranging from $C = 1 \times 10^{-4}$ to $C = 1.2 \times 10^{-2}$ for a fixed

particle size of $d = 240 \mu m$. The suspended particles in the test cell were scanned with an increment of $0.1 mm$ per step and then the total scanning data was combined to produce an accurate distribution of particles in the swept volume, which is treated as the reference set for evaluating the performance of the new method. The new method is proved to be able to provide an accuracy of 2% up to a volume fraction of $C \approx 8 \times 10^{-3}$, which is an order of magnitude greater than the single-camera methods used previously. In order to extend our specific testing conditions to other experimental conditions, the optical depth is examined in the current work and it is speculated that the proposed technique can measure dispersed phase concentration up to optical densities of close to $O(1)$. Finally the proposed technique is applied to an oscillatory sheet flow in which the power-law behavior of the sediment concentration profile at different phases are observed. The new technique is also compared with standard 3D-PTV method and the single camera method and its advantage over the other two methods is demonstrated in resolving the particles in high concentration regions.

2.2 Lagrangian particle tracking

In the previous section, a novel particle 3D reconstruction technique is introduced, which is able to compute the instantaneous sediment particle distribution near the light sheet center based upon single snapshots recorded by three cameras viewing from different perspectives. Given the time-resolved multi-camera measurement, the next task is to compute sediment trajectories, i.e. to link the 3D

reconstructed positions that belong to the same particle in successive time steps, which proves to be challenging when confronted with higher sediment concentrations (average particle spacing, $\lambda_p \approx 3.7 d$ at $C = 1\%$) and irregular and long distances of particle displacement between frames (maximum displacement is $15 \sim 20 \text{ pixels}$, corresponding to $1 \sim 2 d$). In this section, a Lagrangian particle tracking (LPT) algorithm based upon shake-the-box (STB) is developed and the identified trajectories are presented. In the following discussion, the same time-resolved measurement data as collected in Section 2.1.4 was used and the corresponding experiment and measurement set-up details can also refer to this section. Specifically, one realization of 201 time-resolved images captured at phase 158° is used for explaining the proposed LPT algorithm and demonstrating the resultant trajectories.

2.2.1 Algorithms

The Lagrangian particle tracking (LPT) algorithm is built upon the method of shake-the-box (STB, Schanz et al. [1]). The STB method assumes a mild temporal evolution of each individual tracer particle's positions and this temporal coherency can be used to facilitate the 3D reconstruction process and validate the identified trajectories. STB has been proved to be a powerful and robust method when applied to single phase flows with tracer particles under moderate-to-high seeding densities (up to $\sim 0.1 \text{ ppp}$). However, a necessary step in STB prohibits its direct application to sediment particles. An optical transfer function (OTF), which models the particle image with a few parameters varying according to the particle's location, has to be

calibrated and used to project the 3D reconstructed particles on to each camera image. The OTF of sediment particles is too complicated to be calibrated since the illuminating pattern of a sediment particle depends upon many other parameters beyond its apparent location within the image plane, such as the particle’s inner inhomogeneities and local concentration etc. Therefore the STB method has to be modified to accommodate its use with sediment particles. It should be noted that the modified version still retains the basic features of the STB method, such as the acceptance/rejection of the identified trajectories based upon their smoothness (acceleration, change in acceleration) and the utilization of the validated trajectories to predict and pre-solve the sediment particle distribution in the subsequent time step.

The proposed LPT algorithm is outlined in detail in the flow chart shown in Figure 2.14. First the sediment particles are identified in all camera images of the given time record (201 temporal image frames in the current example data set), with their apparent 2D positions, sizes and characteristic brightness recorded. Then the algorithm is divided into two stages, the initialization phase and the iteration phase. During the initialization phase, the particle’s 3D positions in the first 4 time steps are independently reconstructed using the proposed multi-camera single-plane method (MCSP, Section 2.1). Then a standard particle tracking velocimetry algorithm (Cowen and Monismith [100] and Keane et al. [101]) is applied between each pair of the consecutive 3D reconstructed particles and then trajectories of length four are searched and inspected for legitimacy. The inspection (or “sanity check”) is based upon the temporal coherency supposed to be exhibited by the

sediment motion, in which the acceleration and the rate of change in acceleration (“jerk”) associated with each trajectory are computed by central finite difference and only the ones with computed acceleration and jerk below a prescribed threshold are accepted as the “valid trajectories”. The determination of the threshold should account for both the physical velocity fluctuations experienced by the particles, and the differentiation errors due to inaccurate particle position determination. In the current study, considering the time interval between each image pair ($dt = 1\text{ ms}$ with an imaging frequency of 1000 Hz) is much less than the sediment particle response time ($\tau_p = 5.64\text{ ms}$), the actual change in particles velocity or acceleration within trajectories of length four (within three time steps, 3 ms) is expected to be negligibly small comparing to the differentiation errors. So the threshold is determined mainly according to the estimated instantaneous positioning errors associated with each particle, in which a quarter of the sediment particle mean diameter was used.

After the initialization phase is finished, longer trajectories are linked successively in the following iteration phase. A pictorial illustration of how each iteration is conducted is shown in Figure 2.15. At an arbitrary time step n , all of the validated particle trajectories up to time step n are acquired. First, a predictive particle distribution at time step $n + 1$ is reconstructed by fitting a quadratic curve to each particle at the last four time steps, $n - 3$, $n - 2$, $n - 1$ and n , and the extrapolated location at time step $n + 1$ on the curve is the predicted location of the particle. Then the predicted 3D positions are projected onto each 2D camera image and compared with the identified 2D particle positions. If a particle’s projection is within a certain range (a radius of 10 pixels was used, depending on the quality of prediction and the

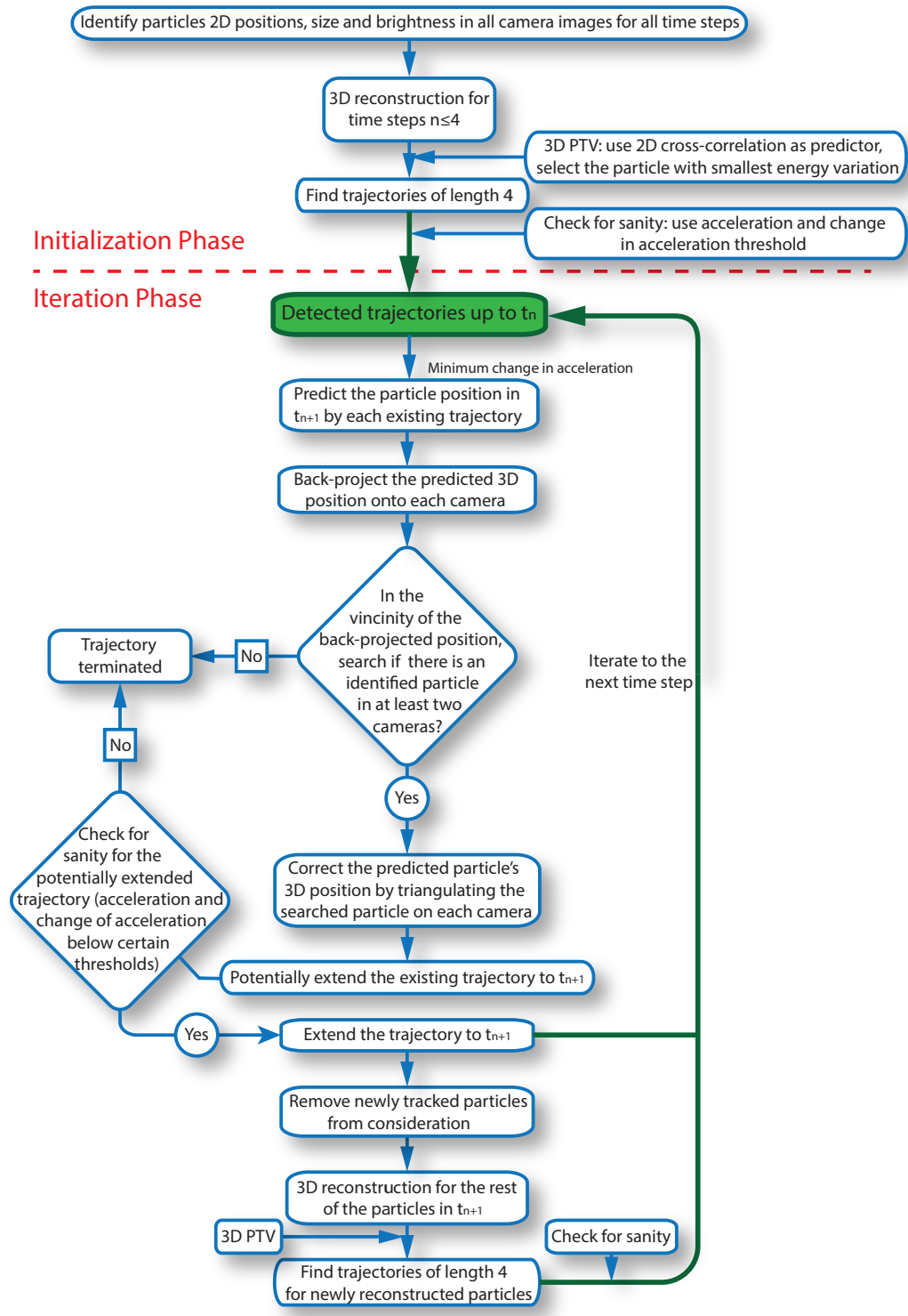


Figure 2.14: The flow chart of the proposed Lagrangian particle tracking (LPT) algorithm.

particle centroid uncertainties) of an identified 2D particle in at least two cameras, then the existing trajectories can be potentially extended to time step $n + 1$ (see particles a and c in Figure 2.15) and the predicted 3D positions can be corrected by triangulating the associated identified 2D particle positions. Before finalizing the extension of the trajectory, the particle locations at time steps $n - 2$, $n - 1$, n and $n + 1$ have to be examined to pass the sanity check. An existing trajectory is terminated if the predicted 3D position cannot be associated with identified 2D particles in at least 2 cameras (see trajectory number 2 and particle b' in Figure 2.15) or the potentially extended trajectories cannot pass the sanity check (see trajectory number 1 and particle a). Otherwise, the trajectory is officially extended to time step $n + 1$ (see trajectory number 3 and particle c) and the successfully linked particle at time step $n + 1$ is removed from consideration in the subsequent 3D reconstruction process (see particle c in the last row of Figure 2.15). After the prediction-matching-elimination procedures are completed, the proposed MSCP method is applied to the rest of the particles at time step $n + 1$ for 3D reconstruction and then standard PTV is applied to the 3D reconstructed particles at time steps $n - 2$, $n - 1$, n and $n + 1$ to compute newly emerged trajectories of length four, as what has been done in the initialization phase. The newly detected trajectories of length four are added to the pool of valid trajectories so that all the particle trajectories are updated to time step $n + 1$, then new iteration begins.

The success of STB relies on sufficient trajectory lengths to ensure a converged stage to be reached, where most of the particles at time step $n+1$ can be reconstructed by prediction instead of in the following 3D reconstruction process. The

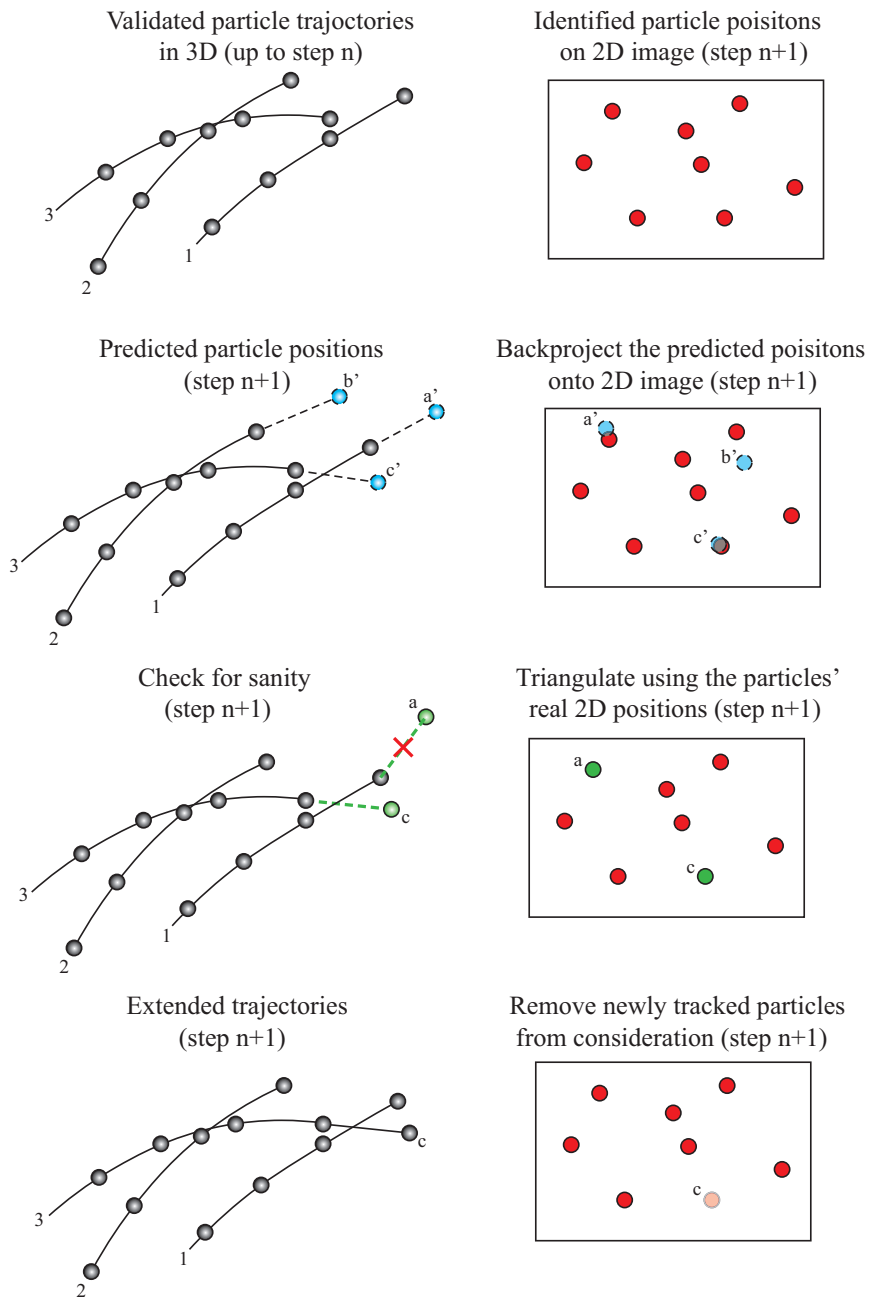


Figure 2.15: A pictorial illustration of the prediction-matching-elimination procedures used in the iteration phase in the LPT algorithm.

success of the STB approach also requires that unlinked particles are predominantly the result of particles that newly enter the field of view, and hence do not yet have a valid history. However, this can only be achieved when most particles can be reliably and consistently identified in many successive time steps in at least two cameras, which means that the particles have to remain within the field of view and the illuminating region for sufficiently long time and that obscuration among particles rarely happens. According to Schanz et al. [1], STB would typically need $10 \sim 30$ time steps to reach the converged stage, even more for higher seeding densities and vice versa. For the sediment particles in our experiment, the median trajectory length is found to be only ten so the converged stage may never be achieved. This is due to two major restrictions imposed by the sediment measurement that compromise the consistent identification of sediment particles in successive images. First, the laser light sheet is constrained to be sufficiently thin ($1 \sim 2\text{ mm}$) in order to increase the capability of measuring more concentrated sediment particles ($C \leq 1\%$), which can cause the particles to quickly drift out of the light sheet and become difficult to be identified. Second, much more severe obscurations occur among sediment particles, especially toward the sediment bed, which increase the uncertainties for a particle to be successively identified. The tracer particles, on the other hand, typically have a volumetric fraction of at least three orders of magnitude smaller than the sediment particles, and thus less obscurations are anticipated.

2.2.2 Trajectories results

A time-resolved measurement, consisting of 201 instantaneous snapshots, acquired at phase 158° (during deceleration, approaching flow reversal) in an oscillatory sheet flow, as described in Section 2.1.4, is selected for testing the proposed LPT algorithm. The particle trajectories being identified up to the 101st time step in the iteration phase is shown in Figures 2.16 and 2.17. Figure 2.16 (a) shows the raw image captured by the middle camera at the 101st time step, while Figure 2.16 (b) is a snapshot of all the 3D reconstructed sediment particles at the same moment. Figure 2.16 (c) demonstrates all the validated trajectories of the sediment particles with trajectory lengths longer than four up to the 101st time step, being projected onto the $x - y$ plane. The upper plot in Figure 2.17 shows the front view of all the 3D reconstructed particles at time step 101, with green denoting the particles that can be associated with a valid trajectory and red representing the unlinked ones. The shaded yellow and blue regions denote two different concentration regions, with $C \lesssim 0.4\%$ and $C \approx 1.5\%$ respectively. It is shown in the figure that under concentrations $C \lesssim 0.4\%$, around 70% of all the reconstructed particles can be successfully linked; while under the highest concentration of our interest ($C \approx 1\%$), only approximately 40% can be linked. Most of the unlinked reconstructed particles lie relatively further away from the light sheet, outside of the effective measurement volume as defined in the concentration measurement in Section 2.1.4, and they cannot be consistently identified in each camera for 3D reconstruction from frame to frame. A plan view of the particle trajectories residing

in each shaded region (boxed by the corresponding color) is shown in the bottom plot in Figure 2.17, clearly demonstrating that the particles drift in the z - direction in both regions and that most of the linked trajectories are located close to the light sheet center ($z = 0\text{ mm}$). The trajectory lengths in the more concentrated region (blue box) is obviously much shorter than those in the more dilute region (yellow box), this can be explained by again referring to the tapered effective measurement volume used for the concentration measurement, only inside which the majority of all the particles can be reliably identified and reconstructed. So towards higher concentrations, particles drift out of the narrower effective measurement volume more quickly and become less likely to be identified, reconstructed and linked afterwards.

The possible sources of position errors associated with the detected trajectories include three major components: 1) the incorrect particle matching during 3D reconstruction, 2) wrong particle tracking between two consecutive images, and 3) the triangulation errors originated from inaccurate determination of particles 2D centroid locations. Since the first two error sources generally cause much more noticeable mistakes, they can be mostly eliminated by the sanity check used in the LPT algorithm. For the third one, it is mentioned in Section 2.1.3 that due to the large sizes of sediment particle images and their irregular intensity distributions, up to 3 *pixels* of centroid location errors can be generated and therefore the 3D reconstructed particle positions are inherently inaccurate. These errors will inevitably propagate to the subsequent velocity and acceleration calculations when differentiating the discrete particle positions along the trajectory. The uncertainties in the velocity and acceleration measurements based upon the acquired sediment particle

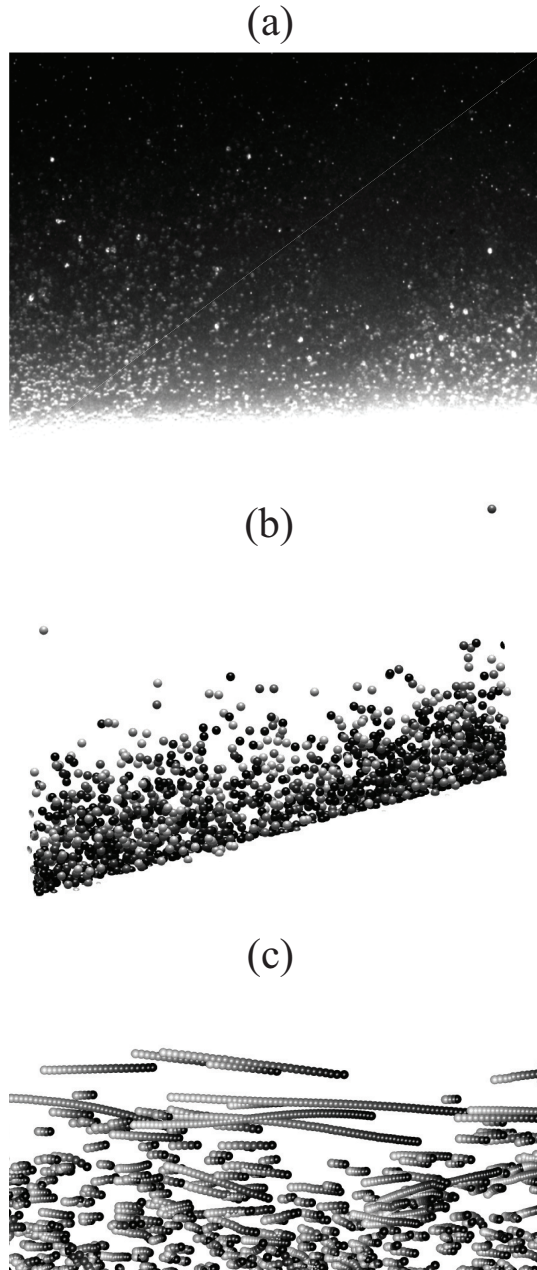


Figure 2.16: (a) The raw image captured by the middle camera at time step 101. (b) A snapshot of all the 3D reconstructed sediment particles at the same moment, colored by the particles' distance to the light sheet center, black being closer to the center and white being further from the center. (c) Front view of the traces of the sediment particles up to time step 101 (the trajectories terminated before time step 101 are not shown). Only the trajectories of length longer than four are treated as valid and plotted. Particles are colored by their time steps, with black indicating later moments and white earlier moments.

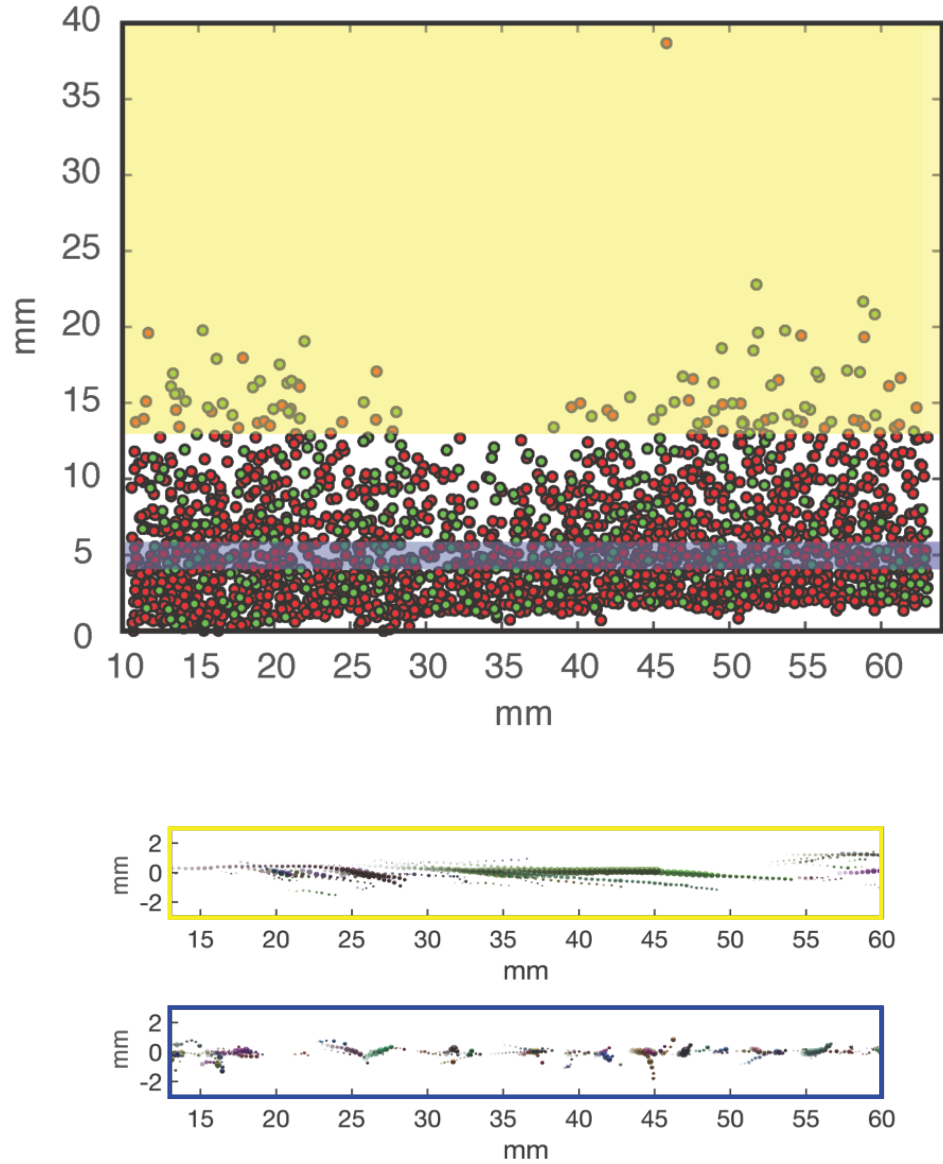


Figure 2.17: [Upper] The front view of all the 3D reconstructed sediment particles at time step 101. The particles that can be associated with a valid trajectory of length longer than four are colored by green, while red denotes the ones that cannot be linked. Two regions shaded by yellow and blue indicates concentration ranges of $C \lesssim 0.4\%$ and $C \approx 1.5\%$ respectively. [Lower] From top to bottom, plan view of the valid sediment particle trajectories up to the 101st time step that reside in the vertical layers shaded by yellow and blue respectively. The size of the plotted spheres are proportional to their mean apparent sizes identified in each camera. The transparency of a particle's color denotes its corresponding time step, with more transparency denoting earlier arrivals and vice versa.

trajectories will be discussed later in Section [4.2.1](#).

Chapter 3: Measurement technique: carrier phase velocity

In the current study, concurrent PTV/PIV measurement of both the sediment particles and the carrier phase flow are conducted in sheet flow conditions to gain a better understanding of the coupled dynamical behavior of the two phases. The measurement of sediment particles, including reconstructing their instantaneous 3D locations and tracking their locations to form trajectories over time, has been described in chapter 2. This chapter will focus on presenting a novel technique that is capable of reliably extracting the carrier phase velocities with the presence of sediment particles up to a volume fraction of $C \sim 1\%$ without sacrificing the sediment measurement. The carrier phase velocity is measured by imaging the tracer particles seeded in the flow. The size of tracers used in liquids is typically on the order of $\mathcal{O}(10 \mu m)$ to achieve a sufficiently small Stokes number, minimizing the induced perturbation and guaranteeing their faithful movement with the ambient flow. The diameter of the tracer particles used in the current sheet flow measurement is sieved ranging from $25 \sim 50 \mu m$, i.e. almost one order of magnitude smaller than the sediment particles. Due to its much smaller size, a tracer particle reflects significantly less light comparing to a sediment particle, given that a particle's intensity is roughly proportional to the particle's projection area. A direct PIV process of the

two-phase images can result in incorrect carrier flow measurements near sediment particles, which tend to be biased by the sediment velocities due to the contamination of the much stronger sediment signals. A reliable phase separation technique is critical for the measurement of carrier phase velocity field, irrespective of the implementation of PIV or advanced particle tracking method.

In what follows, an overview of the past work on how the tracer images were extracted and carrier phase velocities were subsequently computed in multiphase flow measurements is first provided, followed by the challenges confronted when applying existing phase separation techniques directly to the current sheet flow measurements. This motivates a novel imaging method using fluorescent tracer particles along with an apertured long pass filter, which is demonstrated to achieve a desirable balance of intensity between the signals of both phases. Lastly, the proposed apertured filter method is demonstrated in the sheet flow conditions, and shown to produce accurate carrier phase velocity measurement.

3.1 Literature review and problem statement

In multiphase flow measurement, researchers have proceeded in two ways to separate the signals from each phase, one is based upon optical discrimination according to the difference in the emission wavelengths of each phase and the other one is via image post-processing. Optically separating the signals from each phase normally requires the use of fluorescent tracer particles and band-pass filters in front of multiple cameras selectively registering the signals from only one of the phases

(Poelma et al. [91], Blois et al. [102], Elhimer et al. [103]); or the use of RGB cameras (Hagiwara et al. [104]); or the use of dual illuminating sources (Lindken and Merzkirch [105]). In sheet flow measurement, the conventional combined use of fluorescent tracer particles with optical long pass filter can effectively remove the unwanted signals of the sediment particles to enable the direct measurement of the carrier phase, however additional cameras without optical filters must be added to resolve the sediment phase if concurrent measurement is required. Past studies (Poelma et al. [91], Blois et al. [102], Elhimer et al. [103]) typically employed this method only for planar PIV measurement, in which a total of two cameras (one for each phase) are adequate. However, when applying this method in a volumetric measurement imaging configuration, which often requires at least three cameras for each phase, a concurrent two-phase measurement would consist of a total of six cameras, which is not only unaffordable for most labs but also can be very space-consuming and potentially causes difficulties in the arrangement of these cameras near the experimental facilities. Thus it is highly favorable to register both phases in a single monochromatic camera and then use image post-processing techniques to separate each phase. Our goal in this chapter is to introduce a novel apertured filter method, which optimizes the image quality of both phases registered in each single camera and is able to achieve comparable measurement capability and accuracy that could only be previously achieved by assigning cameras dedicated to the measurement of each phase separately.

With both phases captured in a single monochromatic camera, the phases can be discriminated by various image processing techniques developed in the previous

studies, either according to the difference in the particle image characteristics (Kiger and Pan [93], Khalitov and Longmire [72]); using digital masking technique (Gui et al. [92], Lindken and Merzkirch [106], Song et al. [107]); distinguishing characteristic features in the correlation plane/vector post-processing stage (Delnoij et al. [94], Deen et al. [95], Seol and Socolofsky [96]); or by machine learning (Ilonen et al. [108], Poletaev et al. [109], Xue and Katz [110]).

The two most heavily utilized state-of-the-art methods, MFS and TPF, are briefly introduced here, since both of them are extensively used for phase discrimination in the current study. The median filter subtraction method (MFS), proposed by Kiger and Pan [93], is mainly used in the current study for filtering out the sediment signals from the raw two-phase images such that the extracted tracer particle image can be directly used for unbiased PIV process. In this method, the tracer particles (with typical image diameters of $2 \sim 3$ pixels) are treated as “salt and pepper” noise and can be effectively removed by applying a median filter. Under appropriate restrictions, the filtered image would then contain only images of the much larger sediment particles which can be subtracted from the original image to generate a “fluid tracer” image appropriate for single-phase PIV processing. The other method, the two-parameter filtering method (TPF, Khalitov and Longmire [72]) relies on the disparity of the image size and intensity exhibited by the two phases, based upon which the identified objects can be categorized as tracers, sediment particles, or fragments. The detailed processing procedures are discussed in Section 3.4.

Both the median filter subtraction (MFS) method and the two-parameter fil-

tering (TPF) method were developed under the context of two phase flows with very dilute solid particles ($C \leq 0.01\%$), see Kiger and Pan [93] and Khalitov and Longmire [72] for details. These methods immediately fail when implemented for sheet flow conditions due to the much higher sediment concentrations (up to $C = 1\%$) and the huge disparities in the image intensities of the sediment particles and the tracer particles. Figure 3.1 demonstrates a single snapshot taken in an actual sheet flow measurement, extracted from a region with a sediment concentration of $C \approx 1\%$ (left figure) and a region with $C \approx 0.1\%$ (middle figure). When the sediment concentration reaches $C \approx 0.1\%$, even after the MFS method is applied to the middle figure, the sediment residuals dominate the image intensity in much of interrogation regions ($32 \times 32 \text{ pixels}^2$) for PIV cross-correlation. When the sediment concentration further increases to $C \approx 1\%$, only very few tracer particles are visible in the image as denoted by the red empty squares in the left figure, since most tracers, even if not physically blocked by the surrounding sediment particles, blend into the high background noise created by the relatively strong scattered light from the sediment particles outside the light sheet. In order to successfully implement the above methods in sheet flow measurements, balanced signals of both phases are required so that the MFS method can achieve a cleaner filtration of sediment signals, leaving no significant sediment residual intensities so that an increased number of tracer particles can be distinguished from the background.

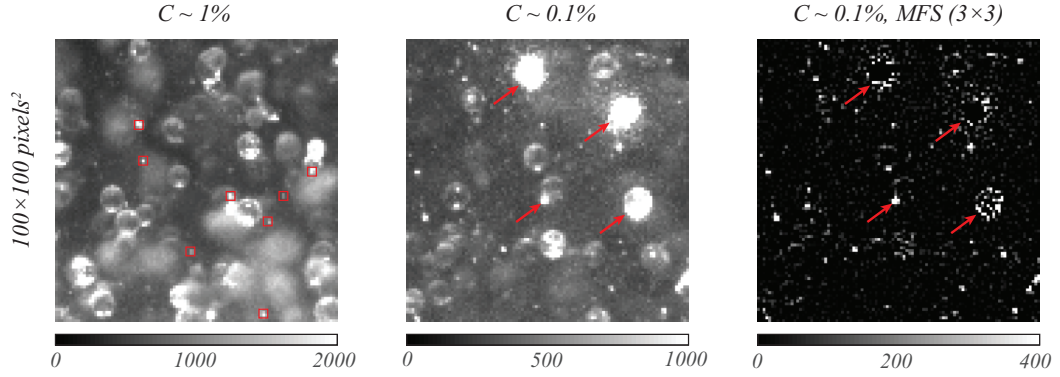


Figure 3.1: [Left]&[Middle] Sampled raw sediment-tracer images extracted from two different concentration regions. [Right] The resultant image after median filter subtraction is applied to the middle one, with a filter length of 3 pixels. Red boxes denote the distinguishable tracer particles and red arrows denote the location of some selected bright sediment particles.

3.2 Description of Apertured Filter method

The apertured filter method is motivated and inspired by the optical phase separation method stated above, in which fluorescent tracer particles combined with suitable band-pass optical filters are used. In this section, the conventional method is first examined in detail under the application of our sheet flow measurement. With its shortcomings revealed, the discussion naturally motivates the development of the proposed apertured filter method. The principle of the apertured filter method is described and its advantages demonstrated in the concurrent measurement of both phases.

3.2.1 Limitations with conventional filters

In the sheet flow measurement, Nd:YLF laser (Photonics Industries, DM60-527) with a peak emission wavelength of 527 nm is used for the illumination of both the sediment particles and the tracer particles. Rhodamine WT fluorescent tracer particles, with diameters ranging from 25 to $50\ \mu\text{m}$, were used for the measurement of fluid velocity. The reflection and emission spectrum of the sediment particles and the fluorescent tracer particles under the illumination of the Nd:YLF laser were measured using a fiber optic spectrometer (Ocean Optics USB4000). This was done by suspending each particle sample (sediment or fluorescent tracers) in water contained in a narrow cuvette and directing the laser beam through the fiber optics into the cuvette. The reflected and emitted light from each sample was then collected by the receiver pointing perpendicular to the light propagating direction. The measured reflection and emission spectrum is displayed in Figure 3.2. The figure shows that the sediment particle spectrum have only one peak that occurs at 527 nm , coinciding with the peak emission wavelength of the laser; whereas fluorescent tracers have two distinct peaks, at 527 nm and 590 nm , which correspond to the scattered light (direct reflection of laser light) and the excited fluorescent light respectively. The relative intensities of these two light components (scattered and fluoresced) were estimated by integrating the tracer particle spectrum curve with respect to the wavelength under each of the two peaks. It should be noted that the intensity is plotted on a log-scale, so even though the first peak (527 nm) is very narrow, its peak value is actually 100 times of that of the second peak (590 nm). Overall, the first

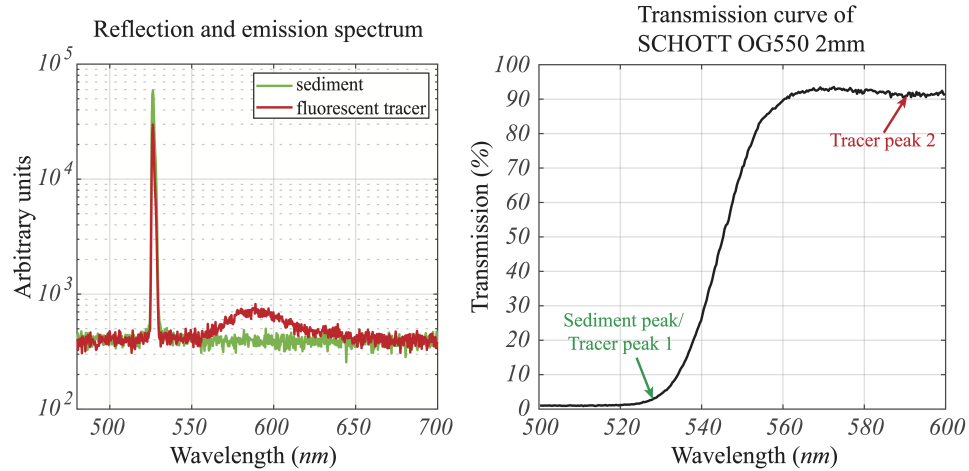


Figure 3.2: [Left] The measured reflection and emission spectrum of the sediment particles and the fluorescent tracer particles respectively, which are consistently used in all the subsequent measurements. [Right] The measured transmission curve of the commercial optical long pass filter, SCHOTT OG550 glass with 2 mm thickness.

peak contributes 75% of the total energy, while the remaining 25% is contributed by the exited fluorescent light. The relative intensities between the sediment signals and the tracer signals should not be compared in this figure, since they depend not only upon their particle sizes but also the number of particles put into the cuvette when preparing each sample.

Commercial optical long pass filters, SCHOTT glass OG550 ($50 \times 50 \times 2 \text{ mm}^3$), were placed in front of each camera lens and used to filter out the sediment signals, whose cut-on wavelengths were also measured by the fiber optic spectrometer, as shown in Figure 3.2. The figure shows that by applying the above filter, 97% of the sediment signals can be blocked and 90% of the fluorescent light emitted by the tracers can be transmitted and received by the cameras, considerably reducing the original intensity ratio between the recorded sediment signals and tracer signals.

The transmission curves of the SCHOTT glass filters used on different cameras vary slightly from one to another and the uncertainty in the transmission rate is within 1%. A pair of raw two-phase images is displayed in Figure 3.3, capturing the same illuminated sediment particles and fluorescent tracers with and without the SCHOTT glass long pass filter respectively. After the application of the long pass filter, the intensities of the sediment particles are substantially diminished and many more tracer particles emerge, which were previously lost in the high background noise resulting from the scattered light from the sediment particles outside the light sheet. The figure also reveals the problem with the direct application of a simple long pass filter: the image contrast of the sediment particles is severely degraded, rendering many of the particles non-detectable with the current phase detection algorithm. The identifiable sediment particles are marked as red solid circles as shown in Figure 3.3. The uncertainties in the centroid determination of the identified sediment particles are also likely to increase due to their weak and even incomplete registered images. The compromised identifiability of the sediment particles and the reduced accuracy in their centroid locations can directly lead to complications in triangulation and 3D reconstruction, increasing the uncertainty associated with their concentration and velocity measurements.

3.2.2 Development of Apertured Filter method

The two images shown in Figure 3.3 represents two extreme cases in terms of the image quality or the identifiability of each of the two phases (sediment and

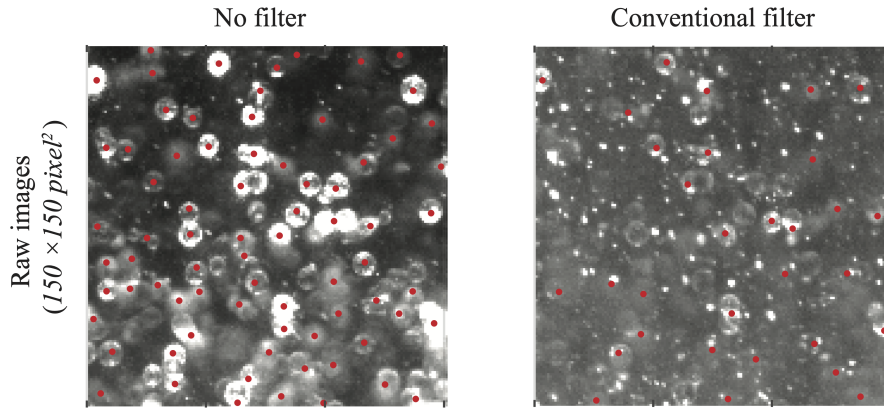


Figure 3.3: Comparison of raw images captured with no optical filter and with conventional optical filter (SCHOTT OG550). The identified sediment particle locations are labeled as red solid circles.

tracers), which naturally motivates the idea of creating a small opening at the center of the applied long pass filter (SCHOTT OG550) to transmit extra green light (wavelength = 527 nm) through the filter, enhancing the sediment signals while keeping the tracer signals more or less the same. The proposed solution is called the “apertured filter method” hereafter. A photo of the fabricated apertured filter consistently used in the current study is shown in Figure 3.4, in which the aperture is created using a waterjet cutting machine (Omax ProtoMAX).

The working principle of the apertured filter method is straightforward and can be easily explained assuming an ideal optical long pass filter, which has 100% rejection and transmission rate for the laser light and the fluorescence light respectively. Without the center hole, only the fluorescent tracer particles can be registered in the cameras; by inducing a small opening (much smaller than the camera aperture size used), the image intensities of fluorescent tracer particles are still primarily gov-

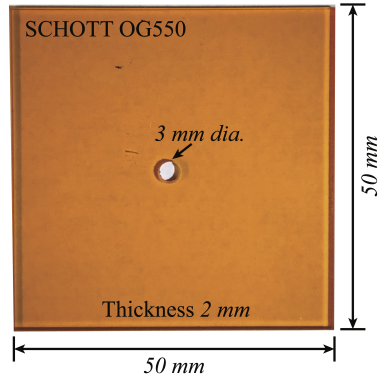


Figure 3.4: The fabricated apertured filter.

erned by the camera aperture size and thus remain almost the same, whereas the sediment particle intensities are solely determined by the hole size on the filter and should be proportional to the hole area. So in effect, with only one single camera, the two phases can be simultaneously imaged under two different “camera aperture” settings independently, i.e. the aperture used for sediment particles are fixed to the size of the hole and the aperture used for tracer particles are determined by camera lens aperture being used. Moreover, even with a fixed hole size on the apertured filter, by simply adjusting the camera aperture ($f_{\#}$), the relative intensities of the two phases can be theoretically adjusted to a wide range of ratios to customize for specific applications.

The effectiveness of the apertured filter method is demonstrated in Figure 3.5, where two-phase images were recorded and compared under three different camera settings, i) with no optical filter ($f_{\#} = 11$), ii) with apertured filter ($f_{\#} = 5.6$) and iii) with a conventional optical filter ($f_{\#} = 5.6$). In this figure, identical distributions of both the sediment particles and the tracer particles under identical illuminations

are imaged, and the only factor influencing the resultant image characteristics is the application of the different types of filters. The two-phase suspensions are generated in a gel-box with statically suspended sediment and tracer particles of prescribed volumetric fractions, which has a similar vertical concentration profile as that measured in an actual sheet flow. The images in Figure 3.5 were extracted from a region where the sediment concentration transitions from 0.2% (upper half) to 1% (lower half). The locations of the identified sediment particles (red solid circles) and the identified tracer particles (green solid squares) are marked on the raw images and the median filtered images respectively. Human intervention has to be used when identifying the tracer particles and details in the phase identification algorithms are discussed in Section 3.4. The size-brightness distributions of all the identified sediment and tracer particles are also plotted in Figure 3.5. Significant underestimation of the identifiable tracer particles and sediment particles is noticed in the “no filter” case and the “conventional filter” case respectively as illustrated in Figure 3.5; while the apertured filter method produces balanced signals for both phases, which enables an excellent identifiability and separability of both phases. The bottom row figures also show that the apertured filter method ensures a much cleaner filtration of sediment signals after median filter subtraction ($3 \times 3 \text{ pixels}^2$) is applied to the corresponding raw image, reducing the energy of sediment residuals to the same level as that achieved by the “conventional filter” case.

Equipped with the apertured filter, the relative image intensities between the sediment particles and the tracer particles can be adjusted by simply changing the camera aperture $f_{\#}$. The actual adjusted results are demonstrated in Figure 3.6

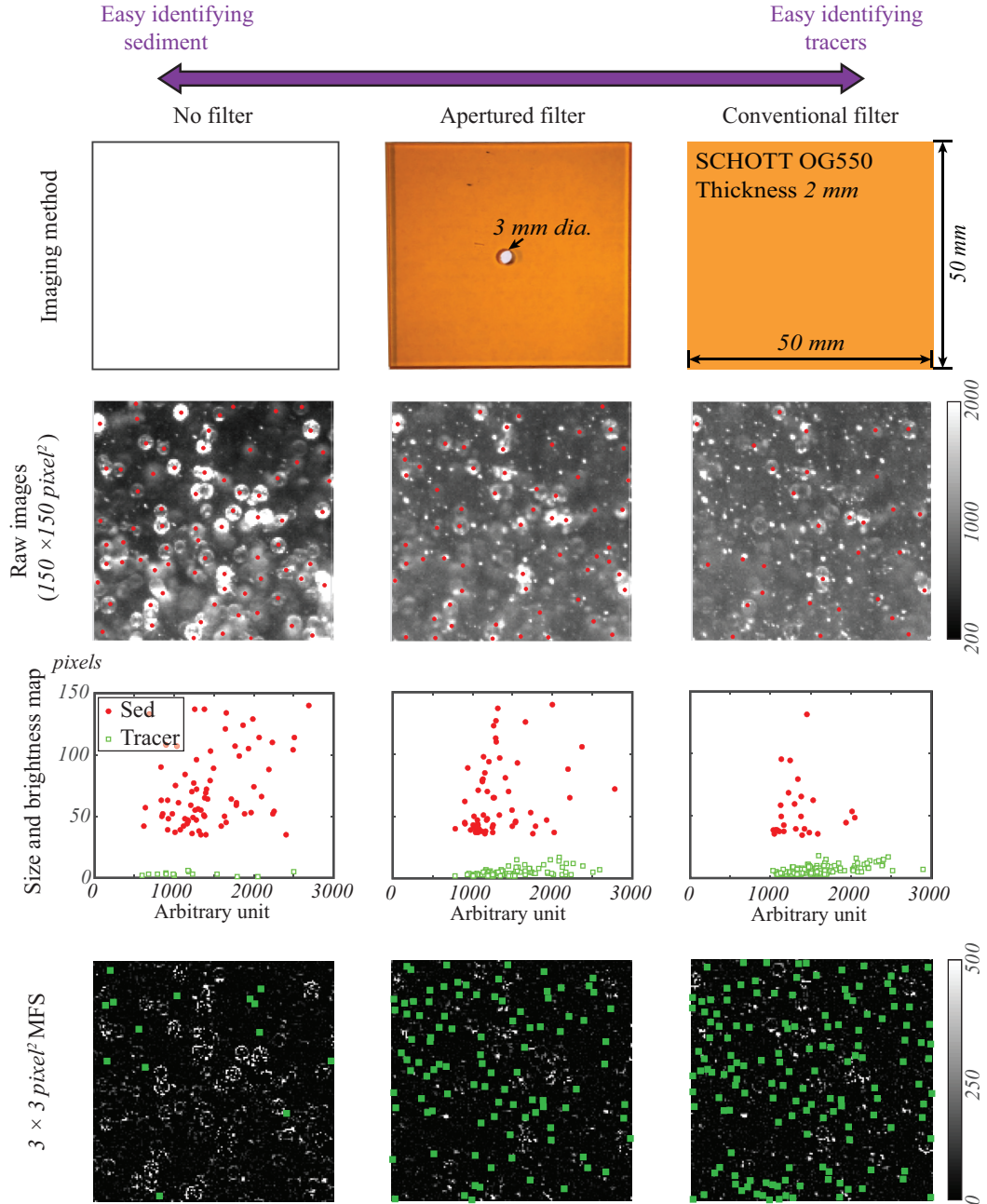


Figure 3.5: The second row shows the raw images captured under three different camera settings (with no filter, with conventional filter and with apertured filter), with identified sediment particles denoted by red solid circles. A median filter subtraction image processing algorithm is applied to each raw image and their results are shown in the bottom row, with identified tracer particles marked as green solid squares. In the third row, size-brightness maps are generated for each particle identified. The raw images were extracted from a region where the sediment concentration transitions from 0.2% (upper half) to 1% (lower half).

by applying three different camera aperture $f_{\#}$'s. With an increase in the camera aperture size (from $f_{\#} = 11$ to $f_{\#} = 2.8$), a noticeable trend of decreased sediment particle brightness and increased tracer particle brightness is clearly shown in the figure. The fewer tracer particles shown in the image with $f_{\#} = 2.8$ compared to $f_{\#} = 5.6$, even though the visible ones appear brighter, is most likely due to the focus degradation that occurs due to the aperture opening in the optical path that is exacerbated at small $f_{\#}$ settings. It is believed that this problem can be mitigated if the hole at the filter center is cast with index-matching material, or if measurements are conducted under a much simpler imaging condition than the one used in the current measurement. With the current imaging set-up, as shown in Figure 3.9, the Scheimpflug imaging conditions and the complex materials with multiple refractive index between the camera and the measurement location (despite of the use of the prisms) can both deteriorate the image quality. It is found that the best image quality for both phases can be achieved when the camera aperture $f_{\#} = 5.6$ is used, which will be used for all the subsequent apertured filter measurements.

It is also worth mentioning that the apertured filter method is inexpensive and easy to implement. The expense for purchasing and manufacturing each apertured filter in the current study is approximately \$80, including the price of the SCHOTT OG550 glass filter and the water jet cutting fee. Otherwise, to substitute the apertured filter, it could be excessively expensive and troublesome, and sometimes even impossible, to find a commercial optical filter with the perfect transmission curve producing the desired rejection and transmission rate at desired wavelengths.

Some technical questions confronted when fabricating the apertured filter are

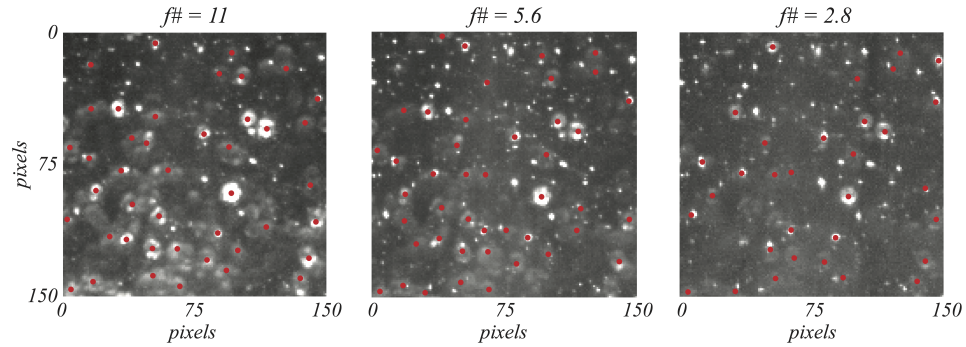


Figure 3.6: Comparison of raw images acquired by apertured filter method, with different camera aperture $f_{\#}$'s applied. The raw images were extracted from a region where the sediment concentration transitions from 0.2% (upper half) to 1% (lower half).

addressed below to assist the readers with the same needs to customize their own apertured filter. 1) The selection of commercial optical filter. Band pass filter with a suitable cut-on wavelength that separates the dominating wavelengths of the two phases is required, preferred with a similar transmission curve of an ideal filter, i.e. large rejection optical density (> 2) and small slope factor. An ideal transmission curve enables a more accurate theoretical estimation of the resultant transmission rate of the apertured filter for the each phase, derived according to the hole size and the camera aperture used. A more ideal optical filter would also enable a larger range of adjustment of relative image intensities between phases. 2) The mechanical vignetting effect, which occurs when objects outside the focal plane protrude into the optical path and results in darkening of image corners. For the apertured filter imaging, the apertured filter behaves as a symmetric obstruction that can potentially form a bright central region in the image center and dark areas towards the image periphery. Tests have been conducted to ensure a complete

elimination of such effect. Consistent with optical lens theory, it is found that the presence of observable vignetting is influenced by the following parameters: the hole size in the filter, the camera aperture $f_{\#}$, the filter-to-lens distance, the thickness of the filter and the angle of view (ratio of camera sensor size to lens focal length). A general rule of thumb is to keep all of the five parameters as small as possible to prevent the vignetting effect. In the current imaging set-up, a 105 mm Nikon Micro NIKKOR lens is used and the filter thickness and hole diameter are 2 mm and 3 mm respectively. The filter is taped directly to the front surface of the camera lens to achieve a practically nearest filter-to-lens distance. With these parameters fixed, different camera aperture $f_{\#}$'s were tested for the vignetting effect and it was found that with $f_{\#} \leq 11$, no vignetting effect can be detected (no noticeable darkening of image corners).

3) Camera focusing issue. The hole at the filter center creates a disparity of the optical paths length (OPL) for light rays (emitted from the imaging object) traveling through the filter versus through the hole directly into the camera sensor and can induce focusing issues. So in order to alleviate the focusing problem, the thickness of the optical filter need to be selected as small as possible to reduce the disparity in the OPL, unless some index-matching material is cast and filled in the hole. This issue can also be mitigated by increasing the camera aperture $f_{\#}$, however as illustrated in 2), there is an upper limit in the $f_{\#}$ to avoid the vignetting effect. With the 2 mm thick apertured filter (SCHOTT glass, $n_d = 1.51$) used in the current study, focused particle images of both phases can be achieved with camera apertures of $f_{\#} \geq 4$.

3.3 Experimental set-up for validation

With the application of the apertured filter method, an extensive experiment is designed and conducted to demonstrate its effectiveness in facilitating phase identification and separation and enhancing the concurrent velocity measurement for both the sediment phase and the carrier phase.

3.3.1 Gel-box construction and imaging set-up

The same practice as has been done in chapter 2 was adopted, where known masses of sediment particles were stationarily suspended in a transparent container filled with dense hydro-polymer gel (Purell hand sanitizer, index of refraction $n_f = 1.365$), enabling repeatable scans of sediment particles through the light sheet. The major limitation of the previous gel-boxes is that each of them contains sediment particles of a single volumetric fraction everywhere, which is very different from what happens in actual sheet flows that consist of a steep gradient of sediment concentrations. As pointed out in Section 2.1.3, the sediment local concentration can potentially change the illuminating patterns of the local sediment particles. The camera viewing angle and viewing optical depth are also different from the ones encountered in actual sheet flow measurements. The goal here is more ambitious: that is, to replicate as similar as possible both the sediment particles near-bed lighting conditions and the camera imaging conditions used in actual sheet flow measurement.

Two modifications were made to the gel-box to meet our goals. First, instead

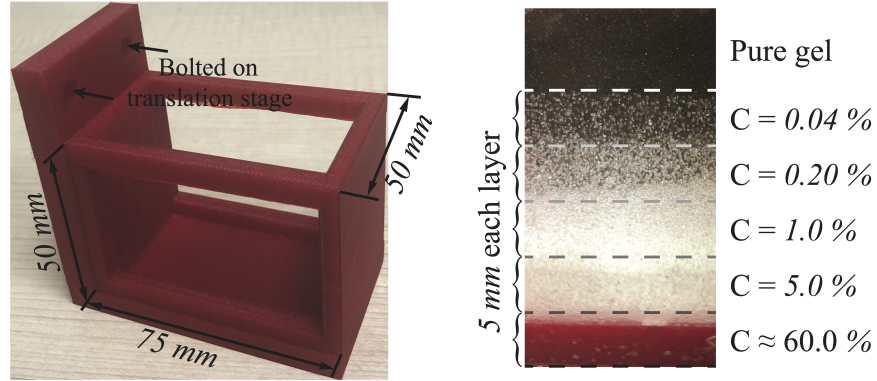


Figure 3.7: [Left] The 3D printed gel-box frame. [Right] Layers of sediment particles with different volumetric fractions.

of a uniform concentration, five layers of sediment particles with different volumetric fractions were statically suspended in the same hydro-polymer gel, each of which contained a 5 mm thick close-packed sediment bed along with 5 slabs of different concentrations that decreased with elevation (each 5 mm thick), as displayed in Figure 3.7. This provides an excellent resemblance of the suspension layer thickness and concentration gradient that occurs in a typical sheet flow. Second, an identical camera and laser set-up as was used during actual sheet flow measurement is maintained, as shown in Figure 3.9. The gel-box container was made of a 3D printed frame with glass slides sealed on the sides and top to allow optical access for illumination and imaging, with dimensions shown in Figure 3.7. Its horizontal dimensions ($75\text{ mm} \times 50\text{ mm}$) are made large enough to maintain the same camera viewing optical depth as confronted in actual sheet flow measurement.

The sediment-gel samples (each with the prescribed volumetric fractions of 0.04%, 0.2%, 1% and 5%) were prepared separately, by mixing known masses of

sediment particles in known masses of hydro-polymer gel, whose density was carefully calibrated with a volumetric flask. Each sample was mixed in a sealed glass bottle (Pyrex) simply by shaking for at least 5 minutes until the sediment particles appeared uniformly distributed everywhere in the bottle. Then each bottle of samples was immersed in a pool of hot water until there was a complete removal of the air bubbles trapped in the gel that resulted from the mixing process. The bottle was kept sealed during hot water bath to prevent the vaporization of the more volatile gel ingredients and no change in the refractive index was found before and after the samples were heated. After that, the prepared samples were carefully filled into pastry bags and squeezed into the gel-box container in sequential layers according to the designed concentration profile. Mixing between layers needed to be prevented, which required extreme patience when squeezing.

A major technical issue confronted during the preparation of sediment-gel samples of large concentrations (5% and 60%, as requested by the newly proposed sediment-gel samples) is documented here for readers of the same needs or of interests, which hasn't been reported in past literatures (Knowles and Kiger [74]) due to the small concentrations ($< 0.1\%$) used in previous studies. It was observed that there was a limit in the volumetric fractions of sediment particles that the hydro-polymer gel can effectively suspend, which is about 2%. When the volumetric fraction is above 2%, shaking the sediment particles in the gel caused a deterioration of the gel, transforming it from an initially "oil-like" substance (viscous, surface shape persevering, retarded flow) to a "water-like" liquid (flowing easily). Once transitioned to a "water-like" state, all the sediment particles settled down to

the bottom forming a close-packed sand bed within hours. The static suspension of sediment particles in the hydro-polymer gel relies on the Bingham plastic phenomenon, enabled by a certain type of thickening agent contained in the gel, named acrylates C10-30 alkyl acrylate crosspolymer. It is suspected that when mixing the sediment particles in the gel, the thickening polymers were entangled on the surface of the sediment particles and lost their thickening properties exhibited in solutions. More sediment particles introduced in the gel could attach more thickening polymers, resulting in a deficiency of thickening polymers left in the gel and the failure of suspension. Fortunately, this thickening polymer, acrylates C10-30 alkyl acrylate crosspolymer, is commercially available (sold as white powders) and once was added into the sediment-gel mixture, the sample with a volumetric fraction of 5% could be successfully produced with exceedingly stable sediment suspensions lasting for months. Within the amount being used, acrylates C10-30 alkyl acrylate crosspolymer can be completely dissolved in the gel and no changes in the refractive index or optical quality of the gel was detected.

The close-packed sediment bed was secured at the bottom of the gel-box test article with the help of SYLGARD 184 silicone elastomer, which has two liquid parts and can be conveniently cast into very complicated geometries by mixing the two parts with the suggested ratio. SYLGARD 184 is known for its excellent optical quality once cured, so it is frequently used for index-matching measurement in experimental studies. Only minimal amount of the elastomer is needed, enough to wet all the sediment particles and form a “paste-like” character, which was then fill in the recessed region at the bottom of the gel-box test article (see Figure 3.7

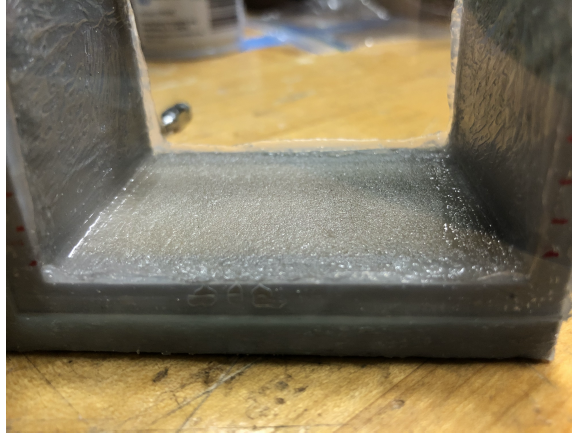


Figure 3.8: The sediment bed secured at the bottom of the gel-box test article, cast with SYLGARD 184 silicone elastomer.

[left]) and left for cure. The cast and cured sediment bed is shown in Figure 3.8, which is steadily secured on the bottom and has the exact same appearance of a real static sediment bed. The other advantage of using SYLGARD 184 is that it isolates the sediment particles from direct contact with the upper gel and avoid the suspension problem described above. The refractive index of SYLGARD 184 is 1.41, slightly larger than that of the gel or water, however this difference should not cause significant changes in the reflected light from the bed comparing to a real static sediment bed.

Two types of gel-box has been made, both having the same sediment concentration in each layer, and one of them is also added with fluorescent tracer particles of comparable amounts used in actual sheet flow measurement. The gel box with tracers (“two-phase gel-box”) represents a more realistic sheet flow measurement and mainly used for qualitative illustrations, such as comparing the image qualities with different imaging parameters as shown in Figure 3.5. On the other hand,

the one containing only sediment particles (“single-phase gel-box”) will be used to generate composite two-phase flow images, for the purpose of examining the phase separation results and quantifying the errors associated with the sediment and the carrier phase velocity measurement, as will be discussed in sections 3.3.2 ~ 3.5.

The gel-box was secured to a precisely controlled 3-axis (along x -, y - and z -direction) translation stage and placed in the water tunnel immersed in water at the exact same location where the actual sheet flow measurement takes place, as shown in Figure 3.9. The details of the laser and camera specifications and orientations are provided in Section 2.1.4 and Figure 2.10. Each camera is equipped with a 105 mm camera lens (Nikon Micro NIKKOR f/2.8) with an apertured filter (3 mm in diameter hole) placed adjacent to its front surface, as shown in Figure 3.9. The camera aperture $f_{\#}$ was set to be 5.6 for all the cameras in all the subsequent apertured filter imaging.

3.3.2 Composite two-phase flow

In order to evaluate the cross-talk effect between phases, we adopt the method used in Khalitov and Longmire [72] and Kiger and Pan [93], in which images of the two phases were taken separately under identical imaging conditions and then these two sets of single-phase images were synthesized to form composite (artificial) two-phase flow images. The single-phase images were processed independently and the processed results were treated as “ground truth”, as they contained no errors originating from the cross-talk between phases. The composite images were processed

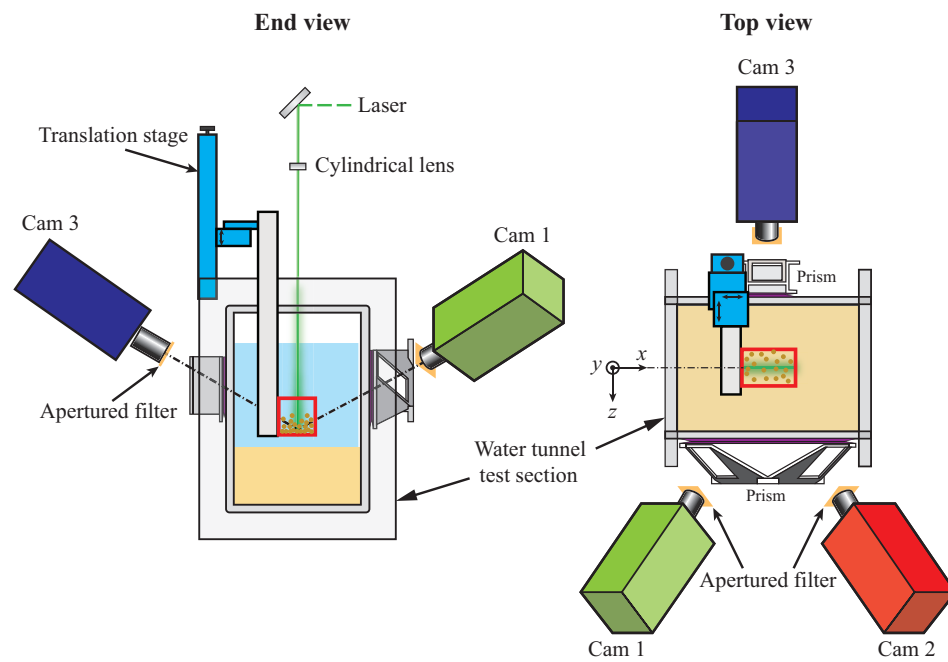


Figure 3.9: The experimental set-up for the validation of the proposed apertured filter method. The validation measurement was conducted in the sheet flow water tunnel, with the gel-box precisely translated along x -, y - and z - axis.

using the same procedure used for real two-phase flow images. The combined signals from the two phases must be separated first and then the separated phases were processed and their results were compared to the “ground truth”. The past work (Khalitov and Longmire [72] and Kiger and Pan [93]) have shown that their image composition algorithms could preserve major image characteristics of both phases and proved the effectiveness of the composition method in quantifying contamination errors due to the presence of the other phase.

In the current study, the sediment phase images were acquired by taking static sediment particle images in the single-phase gel-box at prescribed translated locations. The gel-box was translated in only horizontal directions ($x - z$ plane), with an incremental displacement of 0.1 mm in both directions. The precision of the translation stage is $2.5\ \mu\text{m}$, one hundredth of the sediment particle diameter. Two types of translations were conducted, 1) a total of 125 steps in only depth direction (z - direction), and 2) a 15×10 2D position matrix, 15 steps along x - direction and 10 steps in z - direction (coordinate system is shown in Figure 3.9). The first type of translation was a volume scan of all the sediment particles residing in the central 12.5 mm thick volume of the gel box and will be mainly used for the validation of 3D reconstruction and concentration measurement of sediment phase, same as what has been done in chapter 2; while the second type of translation forms a position matrix that allows us to assign a variety of sediment particle motions and thus were mainly used to quantify the uncertainties associated with sediment velocity measurement. The carrier phase images were acquired by removing the gel-box from the water tunnel and directly imaging the clear water seeded with tracers. The flow in the

clear water is generated by hand-dragging a small piece of plate through the measurement location, which is attached on a thin string to minimize the disturbance of the water surface due to dragging, which can cause the deflections of the light sheet position. These carrier phase images were also used in planar self-calibration when calibrating the cameras.

After the single phase images were acquired, the image composition algorithm used in the work of Khalitov and Longmire [72] is implemented to merge each pair of single phase images into a composite two-phase image. In this algorithm, at each pixel location the intensities were compared between the sediment phase image and the carrier phase image and the larger value is assigned to the composite two-phase image. The synthesized two-phase images are shown in Figure 3.10. Figure 3.10 c) and d) provide a visual comparison between the composite two-phase image and the raw two-phase image taken in the two-phase gel-box, which demonstrates an excellent consistency of the image characteristics of both phases validating the use of composite images in the subsequent study. They also have excellent resemblance of a single snapshot acquired in the actual sheet flow measurements.

3.4 Phase discrimination with apertured filter imaging

With the fast development of 3D particle reconstruction and tracking techniques, Lagrangian particle tracking starts to show its advantages in improving the measurement resolutions and accuracies and so sometimes is preferred over the conventional PIV measurement. One of the most critical prerequisites for the ap-

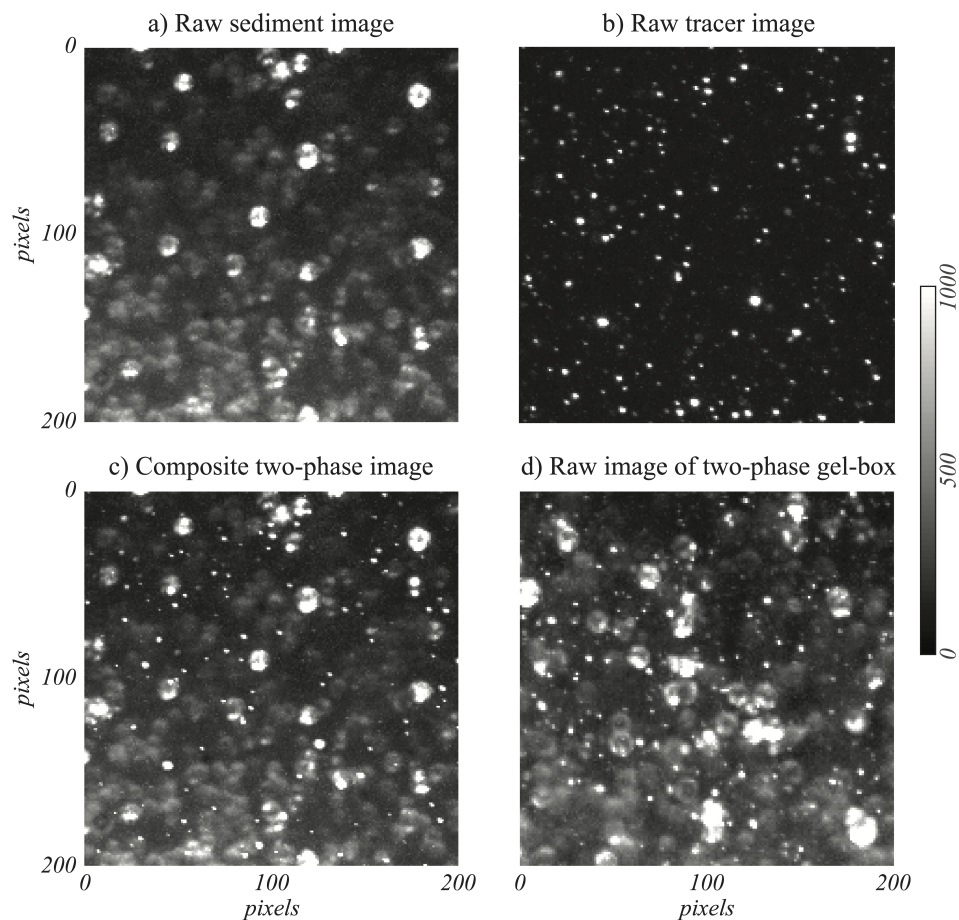


Figure 3.10: a) & b) are the sampled raw single-phase images, used as input to synthesize the artificial two-phase image shown in c), using the algorithm described in the work of Khalitov and Longmire [72]. c) is compared with d), a sample raw image taken in the two-phase gel-box, which demonstrates similar image characteristics of both phases. a) & d), were both extracted from a region where the sediment concentration transitions from 0.2% (upper $0 \sim 100$ pixels) to 1% (lower $100 \sim 200$ pixels).

plication of Lagrangian particle tracking is the identification of the tagged particles within an image, either in the discrete phase or in the carrier phase. The apertured filter method has enabled a decent two-phase imaging with visually distinguishable sediment particles and tracer particles, motivated the use of 3D particle tracking on both phases. In this section, the accuracy and uncertainty associated with the identification of both the sediment particles and tracer particles are evaluated using the artificial two-phase images.

The two-parameter phase separation algorithm proposed by Longmire and Khalitov (TPF, [72]) is adapted for the identification of sediment particles. The algorithm is briefly described as follows: 1) 2D median filter ($7\text{ pixels} \times 7\text{ pixels}$) and 2D Gaussian kernel are applied sequentially to the artificial two-phase image, to remove the tracer signals (existing as “salt and pepper” noise) and smooth the remaining sediment particle image. 2) The convexity of intensities at each pixel is examined to determine whether the pixel belongs to an object or just background noise. 3) The object pixels that form a single connected region are grouped together and labelled as an object with its size (number of pixels occupied) and characteristic brightness (averaged intensity over all the occupied pixels) recorded. 4) A threshold based upon size and brightness is used to determine if the identified object is a sediment particle or not. In the current study, only the size threshold (40 pixels) needs to be satisfied when identifying a sediment particle, since the apertured filter method balanced the intensities of the sediment particles and the tracer particles, and their characteristic brightness showed no noticeable differences, as demonstrated in Figure 3.5. The apparent sediment particle mean diameter and tracer particle

mean diameter are approximately 10 pixels and 3 pixels respectively, so the median filter length applied in step 1, 7 pixels , should be large enough to effectively filter out most tracer signals and the size (area) threshold applied for the sediment identification in step 4, 40 pixels , can account for the majority of particles residing close enough to the light sheet center.

When the above algorithm is applied for tracer particle identification, a significant number of sediment remnants (mainly from out-of-plane sediment or sediment coronas) could also be detected as tracers, as already pointed out in the work of Khalitov and Longmire [72], which acted as a source of noise for the carrier phase PIV measurements. In the current studies, the concentration ($0.01\% \sim 1\%$) is orders of magnitude higher than that used in the work of Khalitov and Longmire [72], which not only increases the number density of sediment particles but also creates a much more complex lighting conditions, and leads to even more misinterpretations of sediment remnants as tracer particles (false positive detections) when applying the above phase discrimination algorithm. It should be noted that the false positive detections and the false negative detections (a valid tracer not being able to be identified) have approximately the same effect on the PIV calculations, both undermining the cross-correlation peak, and they don't necessarily lead to a problematic PIV calculation as long as the false signals are statistically small comparing to the true tracer signals. However if 3D particle tracking is to be conducted, the false positive detections might cause a much worse effect than the false negative ones, since they can act as a source of "ghost particles" during 3D reconstruction and might result in a completely wrong particle velocity vector, whereas the false

negative detections would only reduce the number of reconstructed particles and subsequently sacrifice the spatial resolution. So a new algorithm is developed to identify the tracer particles in a more reliable way, especially aiming to minimize the false positives for the purpose of a reliable particle tracking. In this algorithm, $5\text{ pixels} \times 5\text{ pixels}$ median filter subtraction (MFS, Kiger and Pan [93]) is first applied to the artificial two-phase images to filter out the sediment particles. The size of the filter is selected to guarantee a good preservation of the tracer particle images with less consideration of the completeness of sediment removal. The resultant image after the median filter subtraction (MFS) is shown in Figure 3.11 b). It is shown that the out-of-plane sediment particles with relatively low intensities in the raw image are effectively filtered out by MFS, leaving almost no noticeable traces. The outstanding pixels are mainly composed of either true tracer particles or the remnants of the bright and in-focused sediment particles, as denoted by the green arrows. These sediment particles are often located near the light sheet center and can be reliably detected with the sediment identification algorithm. In order to completely remove these sediment residuals, as a second step, a mask consisting of the identified sediment pixels (acquired from the sediment identification results) dilated by one pixel, as shown in Figure 3.11 c), is further applied to the filtered image. It is shown in Figure 3.11 d) that this step effectively removes nearly all the sediment residuals and leave most of the tracer particles unchanged. At last, a simple threshold (150 *counts*) on the pixel intensities is used to identify all the object pixels (similar to step 2&3 in sediment identification), and then the size and brightness criteria can be used to identify the tracer particles (similar to step 4 in

sediment identification). The parameters used in the last step can be adjusted for the best performance.

The above phase identification algorithms were applied to both the artificial two-phase images and their corresponding source single-phase images for comparison. The identification results are presented in Figure 3.12, where the artificial two-phase image is superimposed with the identified sediment particle locations and the identified tracer particle locations in a) and b) respectively. For each phase, the identification results based on the artificial two-phase image are marked as solid circles and the ones based on the source single-phase image is indicated by empty squares. The unmatched identification results between the artificial image and the source image are colored as blue, consists of the false positive detections denoted by blue solid circles and the false negative detections denoted by blue empty squares.

The sediment particle identification algorithm works exceedingly reliable up to volumetric fractions of 1%, attaining an overall identification error rate below 2%, accounting for both false positive and false negative detections, as demonstrated Figure 3.12 a). The few unmatched sediment identifications between the composite image and the source sediment-only image are mostly due to the out-of-plane sediment particles whose sizes were on the edge of the threshold being applied. These particles will not affect the subsequent concentration or 3D tracking calculations once an appropriate measurement volume thickness is prescribed, as explained in Chapter 2. The only false identification found to be caused by the presence of tracer particles is the false positive detection pointed out by the blue arrow in Figure 3.12 a). It is caused by two adjacent tracer particles being merged together as

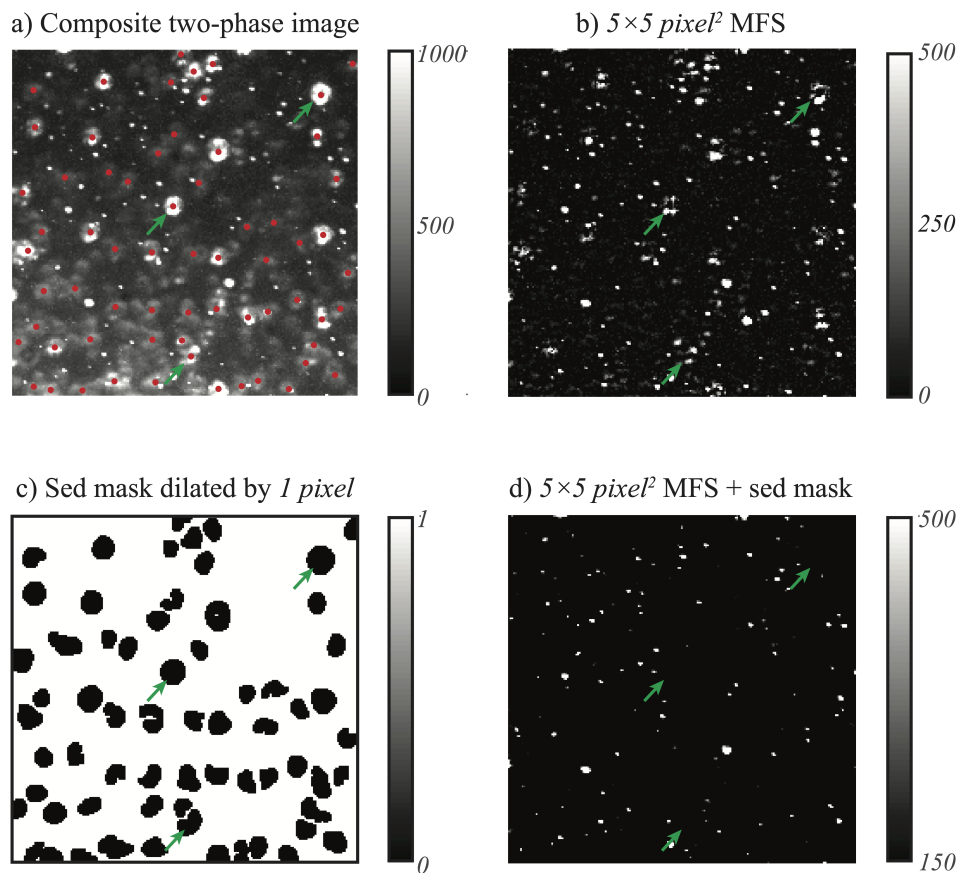


Figure 3.11: Image processing for tracer particle identification: a) The composite two-phase image with identified sediment particles marked as red dots; b) The image after median filter subtraction ($5 \times 5 \text{ pixels}^2$); c) A mask of all the pixels belonging to the identified sediment particles, dilated by one pixel outward; d) Median filter subtraction + sediment mask, where the the color bar starts from the brightness threshold for tracer detection. Three bright and in-focused sediment particles are selected and pointed out by the green arrows. The source single-phase images of a) are presented in Figure 3.10 a) & b).

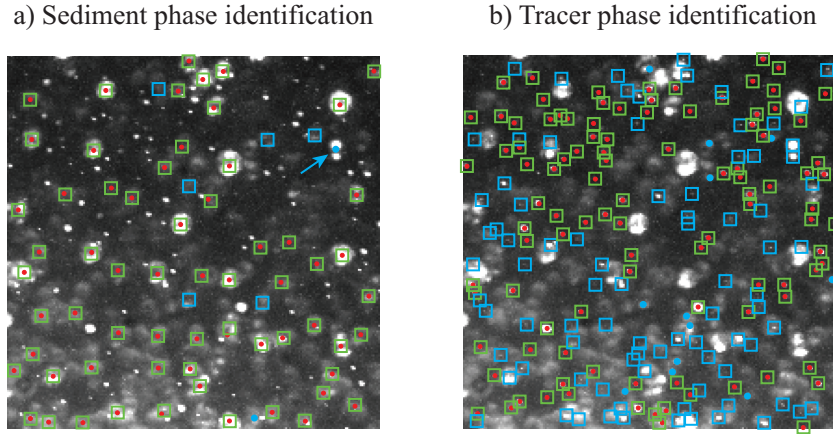


Figure 3.12: The same composite two-phase image superimposed with a) identified sediment particle locations and b) identified tracer particle locations indicated by solid circles, while empty squares represents their true locations computed with the corresponding source single-phase image. All the false identifications (unmatch between circles and squares) are emphasized by blue color, including false positive detections denoted by blue solid circles and false negative detections marked by blue squares. Their source single-phase images are presented in Figure 3.10 a) & b).

one sediment-like particle after the application of median filter and the smoothing kernel (step 1 of the sediment particle identification algorithm). Such occurrences, where the tracer-to-tracer distance is smaller than the tracer particle diameter, are very rare and most likely to be eliminated later during triangulation and particle tracking due to lack of available matching particles in other cameras or in subsequent time steps.

The identification of tracer particles based upon the source tracer-only images is very straightforward and accurate and these high-fidelity results are used as a reference (“ground truth”) to quantify the uncertainty of tracer identification in the composite two-phase images. Two types of errors are defined, the percentage of the number of incorrectly identified tracers normalized by the total number of

tracers being identified (the error rate), and the percentage of the number of the tracers unable to be identified normalized by the total number of valid tracers (the missing rate). The error rate is used to quantify the false positive detections and the missing rate is used to quantify the false negative detections. Both of them can also be represented in Figure 3.12 b), by the ratio of the number of the blue solid circles to all the solid circles (the error rate) and by the ratio of the number of the blue squares to all the squares (the missing rate). In the figure, it is shown that both types of errors strongly depend on the sediment concentration and the error rate ($\sim 5\%$ at $C = 0.2\%$ and $\sim 15\%$ at $C = 1\%$) is much smaller than the missing rate ($\sim 15\%$ at $C = 0.2\%$ and $\sim 50\%$ at $C = 1\%$). The tracer identification algorithm is deliberately optimized in this way for the reduction of the false positive errors, which might have a more significant influence on the subsequent 3D reconstruction and 3D tracking. A closer inspect on the images inside all the blue squares, where the tracers exist but cannot be identified, shows that most of the unidentified tracers can be barely perceived by human visual observation, as they either blend into the high background noise or completely blocked by sediment particles. This means that in the current imaging set-up, even with apertured filters applied, there are still about half of the tracer signals lost due to the presence of sediment phase under a volumetric fraction of 1%.

3.5 Validation of carrier phase measurement

Stereoscopic PIV (SPIV) is implemented to the carrier phase to resolve the 3D velocity vectors located on the light sheet center plane. Before the implementation of SPIV process, image pre-processing is critical in order to remove the unwanted signals from the sediment phase. There are two competing factors when filtering the sediment signals, one is the completeness of the filtration and the other one is the preservation of the true tracer signals. Failure of either of them will tend to increase the uncertainties in the subsequent velocity vector computation. In the rest of this section, two different image processing techniques are applied to the same composite two-phase image and the above two criteria are used to visually evaluate their performance. Then SPIV process is conducted to the filtered two-phase images and the associated errors with both image processing methods are assessed.

3.5.1 Image processing techniques

The first image processing technique is the direct adoption of the one proposed by Kiger and Pan [93], in which the median filtered image is subtracted from the raw image (referred to as “MFS”), whose details are provided in Section 3.1 or in the original paper. For tracer images of diameter $2 \sim 3 \text{ pixels}$ and sediment particle images of diameter $10 \sim 15 \text{ pixels}$, $3 \sim 7 \text{ pixels}$ median filter length proved to be the most effective in filtering out the sediment signals and the smaller the filter length is used, the more complete the sediment signals can be filtered. It is shown in Figure 3.13 c) that even with the most aggressive filtration ($3 \times 3 \text{ pixels}^s$ MFS), the removal

of the bright sediment particles is still unsatisfying, which leaves visible unfiltered traces that have approximately the same intensities as the true tracer signals, shown as “coronas” denoted by the green arrows. The residuals of the sediment signals would inevitably bias the measurement of the carrier phase velocities, which will be quantified later in this section.

For the second image processing technique, it is similar to the one used for tracer particle identification and has been mostly elaborated in Section 3.4. In this method, in addition to median filter subtraction with a relaxed filter length ($5 \times 5 \text{ pixels}^2$), the sediment residuals are further masked out with a binary mask with zeros consisting of all the pixels occupied by the identified sediment particles (referred to as “MFS+mask” hereafter). However, the sediment mask applied may leave empty voids in the image, as shown in Figure 3.13 e), and these voids can also bias the cross-correlation peak during PIV process. To compensate for this effect, the averaged background noise level needs to be computed and subtracted in order to maintain a uniform background level, eliminating the effect of the voids. In the current study, twice the average background noise (40 arbitrary units) is subtracted from the filtered and masked image (Figure 3.13 e)). A comparison of the resultant image with and without background noise subtraction is presented in Figure 3.13 e) and f), in which an over-saturated gray scale is used to manifest the background noise. It is shown that after background noise subtraction, a much more uniform background is achieved despite of the non-uniform distribution of tracers.

A direct visual examination of the filtered two-phase images by the two image processing method is provided in Figure 3.13 c) and d). The MFS+mask method

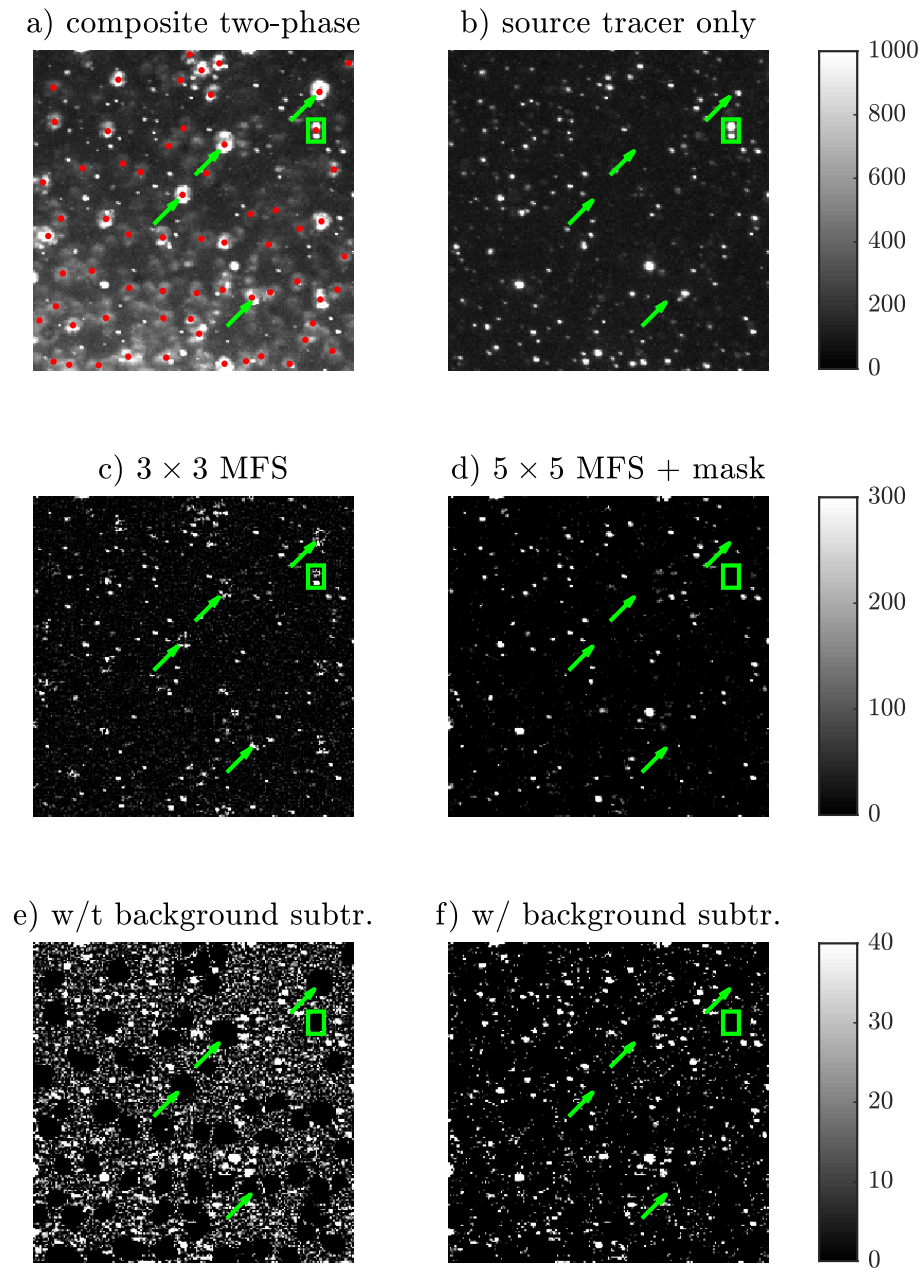


Figure 3.13: a) The composite two-phase image with identified sediment particles marked as red dots. c) & d) used two different algorithms to filter out the sediment signals in a), aiming at a clean tracer image extraction. b) is the source tracer image (single phase before composition) and serves as the “ground truth” for c) & d) to compare with. e) & f) both use the MFS+mask method, without and with the background noise subtracted. The corresponding source single-phase images are presented in Figure 3.10 a) & b).

clearly achieves a much cleaner removal of the sediment signals than the MFS method, indicated by the green arrows; meanwhile, due to the relaxed median filter (larger filter length) being used, it also achieves an improved preservation of the tracer particle images. The success of the MFS+mask method relies on an accurate sediment identification results. The incorrect elimination of tracer signals, as denoted in the green box in the figure, are due to incorrect sediment identification and only very rarely occurs. These incorrectly eliminated tracer particles can survive with the MFS method.

3.5.2 Stereoscopic PIV error quantification

The filtered composite two-phase images using the above two image processing techniques along with their corresponding source single-phase tracer images were all directly fed to Davis 10 for stereoscopic PIV process. The resultant velocity vectors computed with the source single-phase images are used as the high-fidelity reference for the two-phase image to compare with. The disparity only represents the cross-talk errors, originated due to the presence of the sediment phase. In order to reach a statistical convergence, 151 source tracer image pairs and 13 different source sediment particle images were used to generate a total of $151 \times 13 = 1963$ pairs of synthesized two-phase images. The 13 sediment images were uniformly extracted from the volume scanning data set with a constant interval of 1 *mm*, resulting in 4 \sim 5 completely independent sediment phase images. In each image pair, the same sediment particle image is used, indicating precisely zero motions

in the sediment phase. In the carrier phase flows, the time interval dt between each image pair is selected to achieve roughly the same maximum absolute displacement as that encountered in the actual sheet flow measurement (around 10 pixels). The out-of-plane displacement in the artificial two-phase flows are found to be close to those experienced in actual sheet flow. Stereoscopic PIV processing is conducted between each pair of cameras, in which an iterative multi-pass computational scheme with the smallest interrogation window size of $32 \times 32 \text{ pixels}^2$ is used and a maximum reconstruction error of 1 *pixel* is allowed. With three cameras used in the current experimental set-up, each instantaneous realization of carrier phase flow corresponds to three measured velocity fields (computed from each pair of cameras), which should completely agree among each other for ideal measurements. At each location, three velocity vector candidates are available and in order to choose the one with the most confidence and accuracy, the velocity uncertainties associated with the three computed velocities are compared and only the velocity with the smallest uncertainty is exclusively used to determine the local velocity. The velocity uncertainties were computed by first evaluating the cross-correlation uncertainties in each camera according to the correlation statistics and then propagating the 2D uncertainties to the 3D triangulated velocity measurement (Wieneke [111], Sciacchitano and Wieneke [112]).

Figure 3.14 and 3.15 displays the spatial displacement error distributions associated with the artificial two-phase images, which is found to be highly correlated with the local sediment concentration. The dash-dotted lines demarcates the five different sediment concentration layers, with $C = 0\%$, $C = 0.04\%$, $C = 0.2\%$, $C = 1\%$

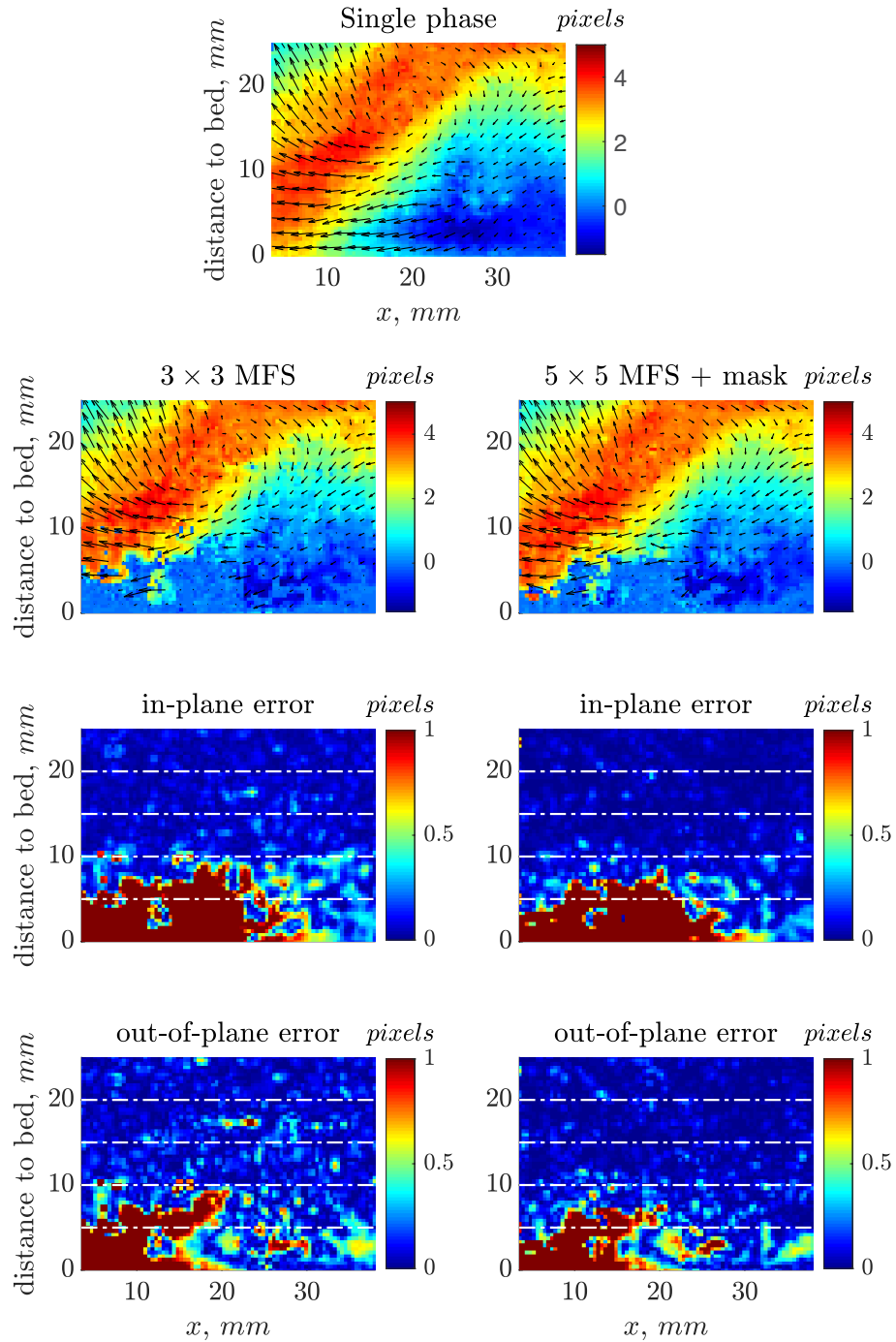


Figure 3.14: Displacement field of a single realization of carrier phase flow. The maximum displacement in the in-plane (x - and y -) and out-of-plane (z -) directions are both around 5 pixels . The instantaneous absolute errors are also shown. The dash-dotted lines shows the demarcation of the five different sediment volumetric fractions (0%, 0.04%, 0.2%, 1% and 5% from the top).

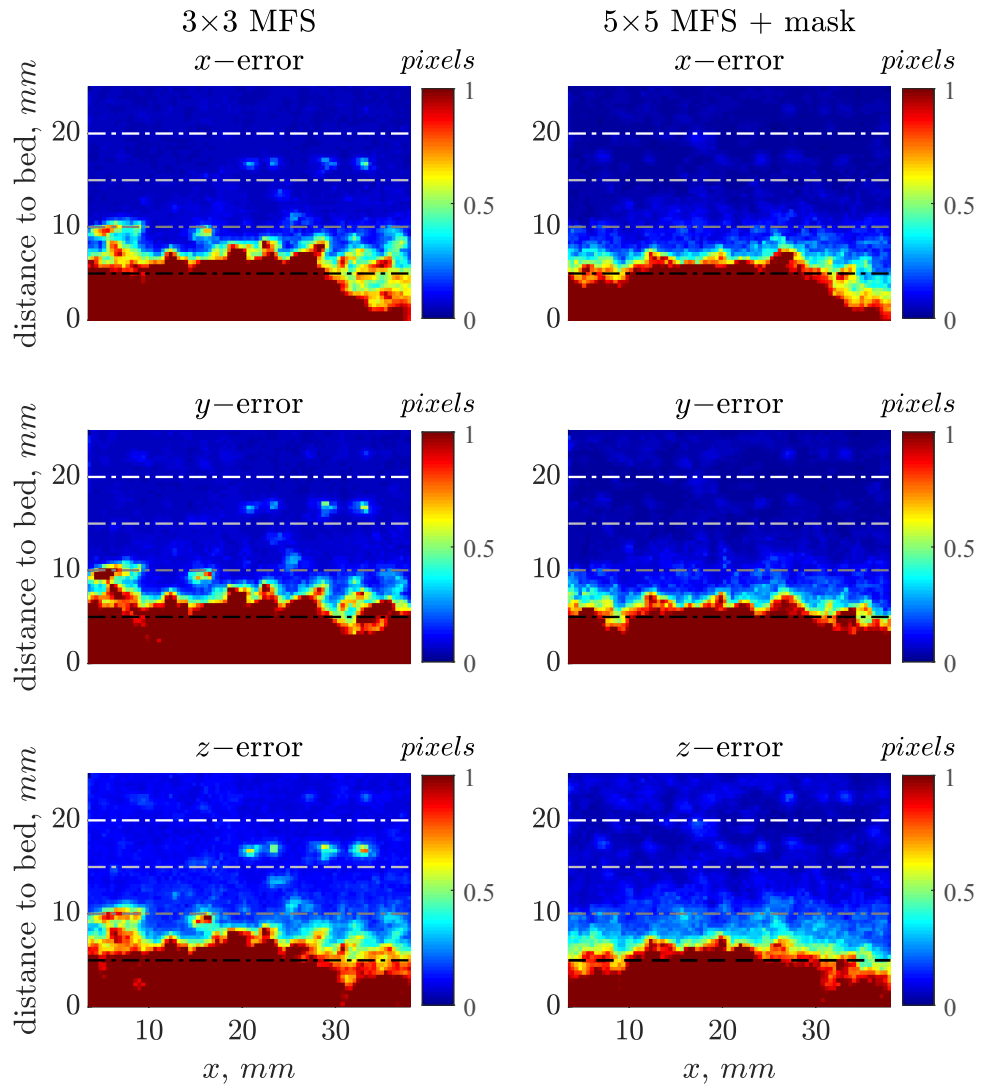


Figure 3.15: Averaged absolute errors in the carrier phase displacement for all the carrier phase flows under a single sediment distribution. The dash-dotted lines shows the demarcation of the five different sediment volumetric fractions (0%, 0.04%, 0.2%, 1% and 5% from the top).

and $C = 5\%$ increasing from the top layer. The instantaneous displacement field is compared in Figure 3.14, with the instantaneous absolute displacement errors quantified in the in-plane and out-of-plane directions separately. Strong out-of-plane motions and a distinct vortex can be observed in the instantaneous displacement field, both of which are faithfully captured in both of the filtered images. It is shown in the error plots that for concentrations $C \leq 0.2\%$ (the top three layers), both filtering methods can very effectively remove the sediment signals and only generate errors up to 0.3 pixels , especially for the MFS+mask method probably due to the larger filter length utilized, which induce less alterations of the original tracer images. Within the concentration layer of $C = 1\%$, a sharp transition from low error level ($\sim 0.1 \text{ pixels}$) to high error level ($> 1 \text{ pixels}$) exists, that occurs around 7 mm above the bed. This is due to the fact that all the cameras are looking downwards into the suspended sediment samples so there is an overlap of registered sediment particles from adjacent concentration layers. Within the 5% concentration layer, the carrier phase can no longer be reliably extracted and so the measurement should not be trusted any more. The lower error region in the bottom right corner occurred in the 5% concentration layer is due to the small difference in the displacement between the local carrier phase motion and the static sediment motion, and the cross-talk error can only occur when the two phases renders different velocities.

The same observations and conclusions can be made with the mean absolute errors shown in Figure 3.15, in which a single sediment phase image is used and the average is conducted over the 151 different carrier phase flows. The purpose of this figure is to show if there is any consistent error patterns associated with the

sediment particle distribution, since the velocity vectors near a sediment particle are expected to consistently exhibit a high error level. It is shown in the figure that there isn't a strong correlation between the displacement errors and the sediment particle locations.

Figure 3.16 demonstrates the ensemble average and the cumulative distribution of the absolute errors in the carrier phase displacement computed in each of the four different sediment concentration layers ($C = 0.04\%$, $C = 0.2\%$, $C = 1\%$ and $C = 5\%$). The average is computed over all the available artificial two-phase flow images, i.e. using all the carrier phase flows and all the sediment distributions. When calculating the statistical errors in the concentration layer of $C = 1\%$, the displacement vectors located in the bottom 2 mm are excluded to isolate the effect from the 5% concentration layer. It is found that with the MFS+mask method, under concentrations $C \leq 0.2\%$, a mean absolute error of 0.1 pixels and an error bound of $\pm 0.2\text{ pixels}$ with 95% confidence can be achieved in all displacement directions. When the local concentration increases to $C = 1\%$, a mean absolute error of 0.2 pixels in the x - and y - directions and 0.3 pixels in the z - direction can be achieved and the corresponding 95% confidence error bounds are $\pm 0.7\text{ pixels}$ in the in-plane directions and $\pm 1\text{ pixels}$ in the out-of-plane direction respectively. It is noticed that the MFS+mask method can consistently attain a slightly more accurate displacement calculation under all of the four concentrations than the MFS method and thus will be adopted when computing the actual sheet flow carrier phase velocity. It should be mentioned that the overall carrier phase measurement errors should consist of not only the cross-talk errors, as addressed above, but also the inherent

PIV errors associated with single phase PIV measurement, which is relatively small comparing to the prior (typically smaller than 0.1 pixels).

At last, it should be emphasized that comparing to the actual sheet flow measurements, the above validation experiments were conducted with similar sediment concentration profile and with the exact same imaging set-up, and the acquired images were processed with the same procedures using the same parameters, so the above reported measurement uncertainties should be safely applied to the actual sheet flow measurement results, which will be presented in Chapter 4. Some differences that can potentially affect the reported actual sheet flow measurement uncertainties should be pointed out as follows: 1) the artificial effects in the composition of the two-phase images, 2) the difference in the tracer particle seeding density, 3) the difference in the sediment particle motion (no sediment motion in the above error analysis), and 4) the difference in the carrier phase flow characteristics, such as motion scales and shear rates.

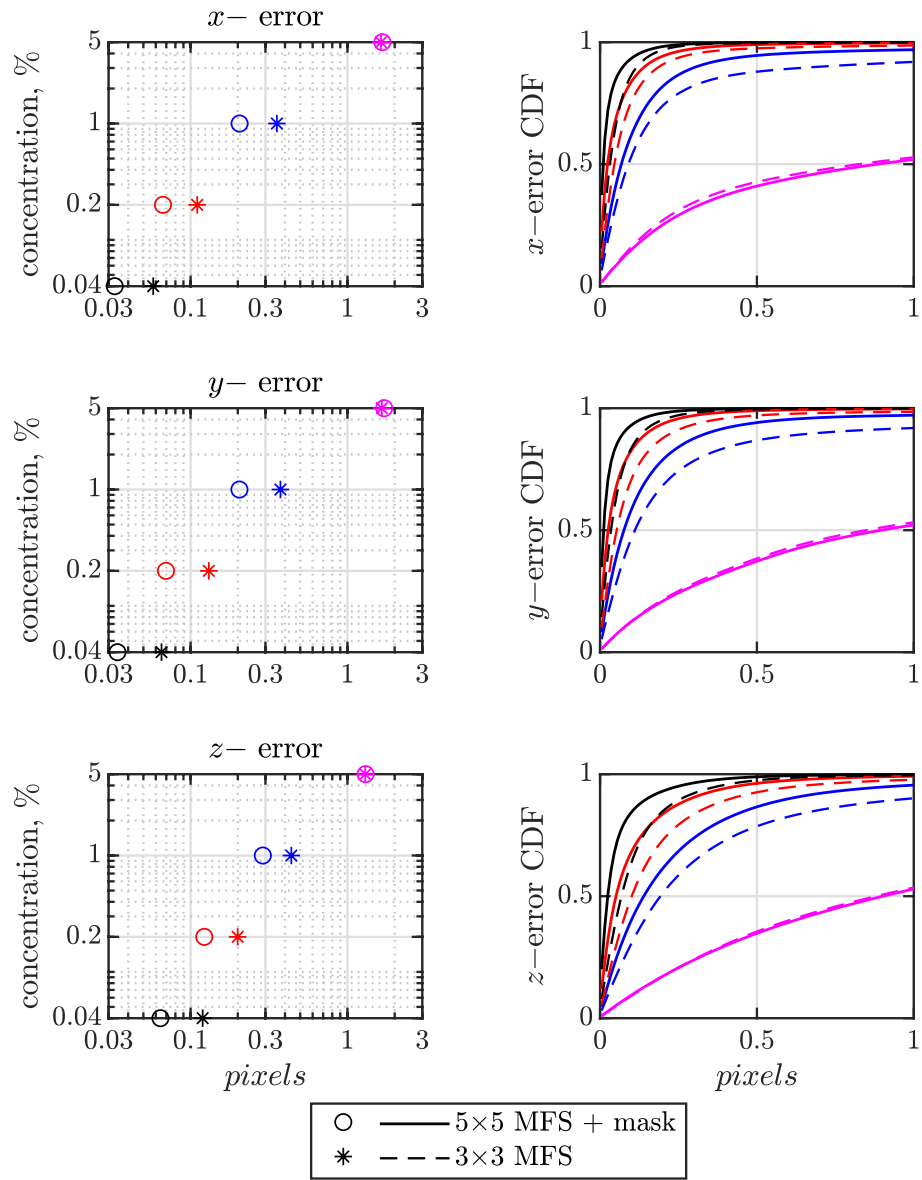


Figure 3.16: The ensemble average and the cumulative distribution of the absolute errors in the carrier phase displacement accounting for all the carrier phase flows and all the sediment distributions. Only the displacement vectors located in the upper 3 mm is used when calculating the mean error in $C = 1\%$ concentration layer.

Chapter 4: Particle-turbulence interaction during flow reversal under oscillatory sheet flow

4.1 Experimental details

The experimental and imaging set-up has been demonstrated in chapters 2 and 3, which are consistently used in the actual sheet flow measurement. A brief summary is provided in the following for the completeness of this chapter. The schematic of the oscillatory flow tunnel used to generate the sheet flow is presented in Figure 2.9, with its dimensions, the coordinate system and the measurement location and area indicated. The detailed laser and camera configurations are presented in Figures 2.10 & 3.9, in which Nd:YLF laser (Photonics Industries, DM60-527) and three high-speed cameras (Phantom v640/641, Vision Research, 4-megapixel, 12 bit depth) each equipped with a 105mm lens (Nikon Micro NIKKOR, $f_{\#} = 5.6$) and an apertured optical filter (SHOTT OG550 2mm thick, 3 mm in dia. hole) are used. Multiple spherical and cylindrical lenses are used to converge the laser beam overcoming a long travel distance ($\sim 6 m$) and spread into a sheet of light at the measurement location, with a nominal thickness of $1 \sim 2 mm$. Prisms, with 3D printed frames, were placed between the cameras and the test section to alleviate the

astigmatism effect due to the inclined viewing angles of the cameras. The cameras and the prisms were both mounted on a 80/20 aluminum frame, which were bolted directly to the steady concrete floor. A soft connection is created between the prism frame and the test section side wall using stripes cut from plastic bags, between which water is contained. In this way, any vibrations in the test section caused by the motion of the piston when running experiments can be effectively isolated from the imaging system. Some other details on experimental procedures and data acquisition schemes are discussed in the following sections [4.1.1~4.1.3](#).

4.1.1 Oscillatory flow tunnel: piston motion

Oscillatory sheet flow is generated in the water tunnel (see [Figure 2.9](#)) by driving the flow in the horizontal test sections with a piston in the tall tank on one end. The piston motion is precisely controlled by the feedback control system equipped with a position sensor directly measuring the instantaneous piston position. Highly repeatable piston motions can be generated and [Figure 4.2](#) illustrates the uncertainties in the piston motion in one of the experimental runs during the sheet flow measurements, with target external flow velocity varying with time periodically as $U_o(t) = U_{o,p} \sin(2\pi t/T)$, m/s , where $U_{o,p} = 1 m/s$ is the nominal magnitude of the free stream velocity and $T = 5 s$ is the bulk flow oscillation period. [Figure 4.2](#) compares the actual piston displacement (measured by the position sensor) and velocity, sampled at a frequency of $1024 Hz$, to the corresponding commanded values. The velocity signals were computed by differentiating the measured position profile. The

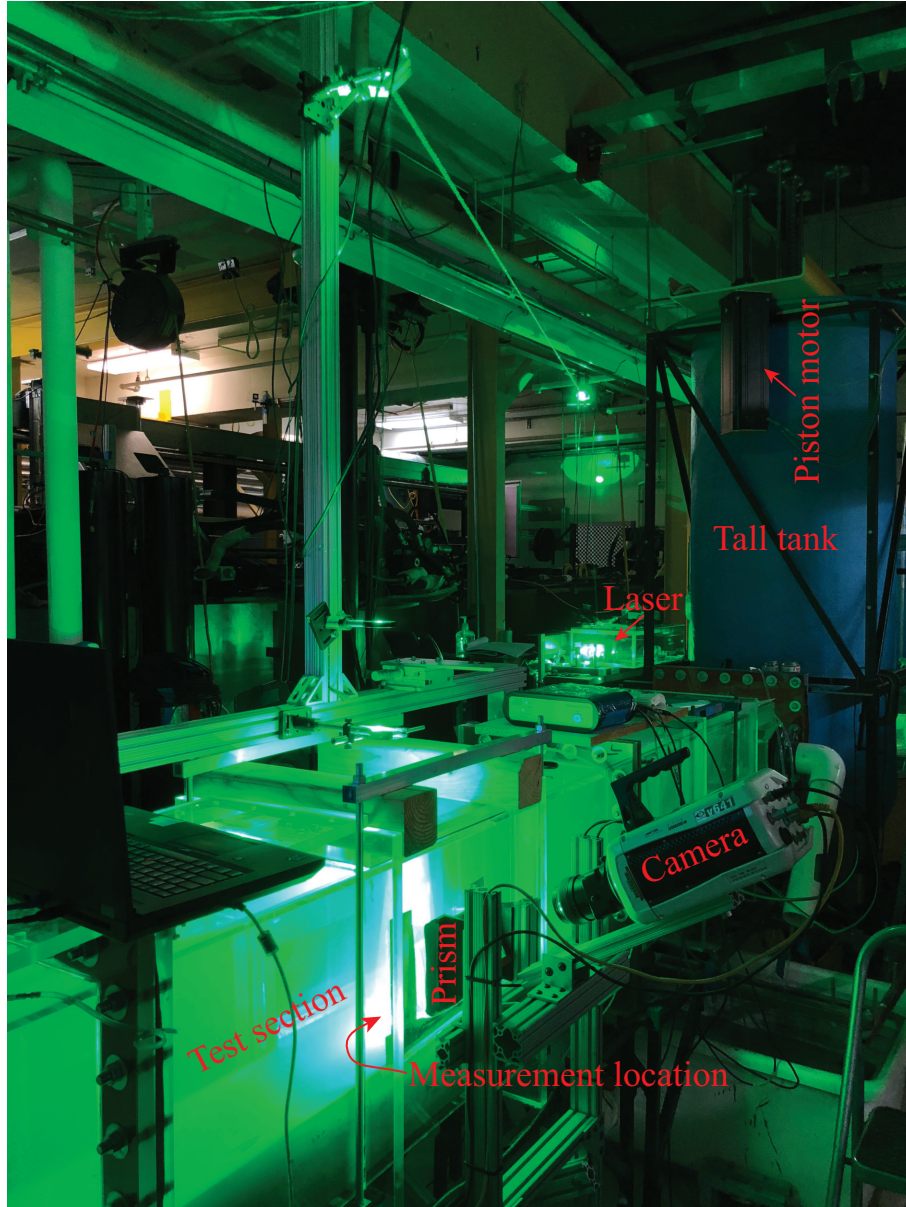


Figure 4.1: A photo taken during data acquisition, showing an overview of the actual experiment and imaging set-up.

inherent noise in the position measurements is significantly magnified after differentiation, so a sliding average of 100 *ms* was applied to the velocity profile to smooth out the high frequency noise. Both the actual displacement and the actual velocity consistently demonstrate systematic phase lag and overshooting effect comparing to the commanded values. The overshoot ratio was measured to be around 4% of the amplitude for both the velocity and the displacement profiles. Due to the observed phase lag, a direct trigger system based upon the piston's actual instantaneous position was implemented, as will be discussed in Section 4.1.2. With the corrected target (or commanded) profile (shifted in phase and scaled), the percentage error of the actual piston motion (normalized by the amplitude) is computed at each instant in time and also shown in Figure 4.2, which amounts to 0.24% normalized root-mean-square (rms) error for the displacement and 1.28% for the velocity. More details in the flow tunnel construction and the qualification of the flow tunnel performance with smooth non-mobile bed can be found in the previous work of Knowles [70].

4.1.2 Synchronization and triggering

Phase-locked measurements at every 10° within each cycle ($T = 5\text{ s}$) are desired, which requires periodic signals associated with the piston motion to synchronize the measurements to each phase. This is realized by the laser-photodetector triggering system as illustrated in Figure 4.3. A Helium-Neon laser is fixed on the top of the piston tank and the photodetector (PDA100A, Thorlabs) is secured to the

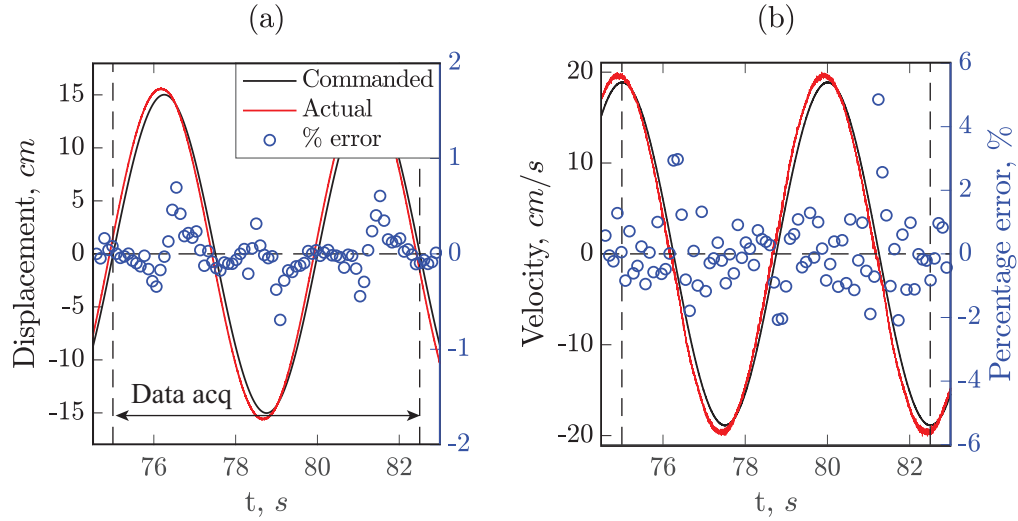


Figure 4.2: The actual piston motion errors relative to the commended signals in a) displacement and b) velocity.

upper plate of the piston structure that actuates the piston. In each experimental run, the piston starts from its mid-stroke equilibrium position (also referred to as “home position”) in a sinusoidal fashion. The laser beam is aligned to the center of the photodetector when the piston is initially at home position, such that every time the piston passes mid-stroke, the photodetector receives the laser light and outputs a pulse signal (see Figure 4.3). The pulse signal needs to be sufficiently brief relative to the timing precision required for the data collection to accurately represent the instant when the piston is at home position. A pinhole with a diameter of $500 \mu m$ is secured in front of the photodetector to further reduce the pulse width. Finally, a less than $\sim 5 ms$ pulse width can be achieved, as shown in the figure. These pulses represent the instants when the piston is at home position and one of them is used to define the starting point of the subsequent phase-lock measurements.

The detailed image recording scheme is illustrated in Figure 4.4. The pulse generated by the photodetector triggers the pulse-delay generator (Model 577, Berke-

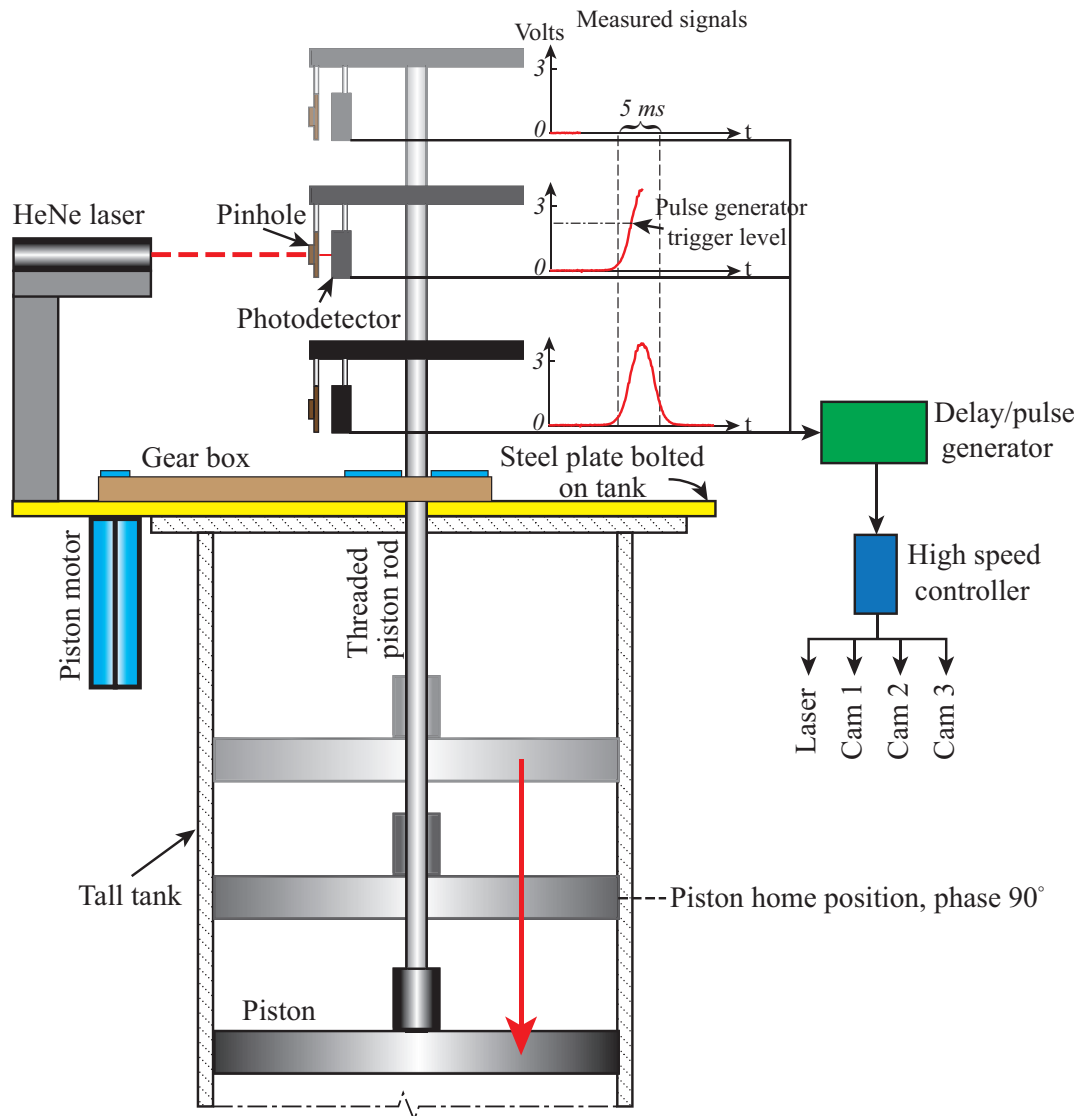


Figure 4.3: Schematic of of the triggering system.

ley Nucleonics), which, after a pre-calculated delay of 120.4 ms , starts to generate periodic pulses precisely with the desired phase-locked frequency (every 10° , or 138.9 ms). The phase-locked pulses are then used to trigger the HighSpeed Controller (Lavision), which integrates the three high-speed cameras and the laser to acquire images at a frequency of 2000 Hz (in single pulse or time-resolved mode). 75 time-resolved images are recorded at each phase administered by the pulse-delay generator and the pre-calculated delay time ensures that the middle ($\sim 38\text{th}$) of the recorded images corresponds to the exact instant of each phase. The phases are defined according to the piston/external flow velocity profile (consistent with the one defined in Figure 2.11), in which phase 0° and 180° correspond to moments of zero free stream velocities/flow reversals and phase 90° and 270° correspond to the occurrence of maximum/minimum external flow velocities.

The uncertainties in phase synchronization is assessed. The above triggering scheme relies on an accurate detection of the exact moment when the piston is at home position, which acts as a reference starting point for the subsequent triggers. The majority of the timing error is associated with the slight misalignment of the laser beam to the piston home position. A conservative estimate of the misalignment error gives an upper bound of $\pm 1.5\text{ mm}$, which corresponds to a timing uncertainty of $\pm 7.5\text{ ms}$ given the speed of the piston at home position is approximately 20 cm/s . Another timing error originates from the finite width of the pulse signal of the photodetector. Since only the pulse peak represents the exact moment when the piston is at home position, the offset between the peak and the actual triggered point of the pulse-delay generator can induce additional timing errors. It is shown in

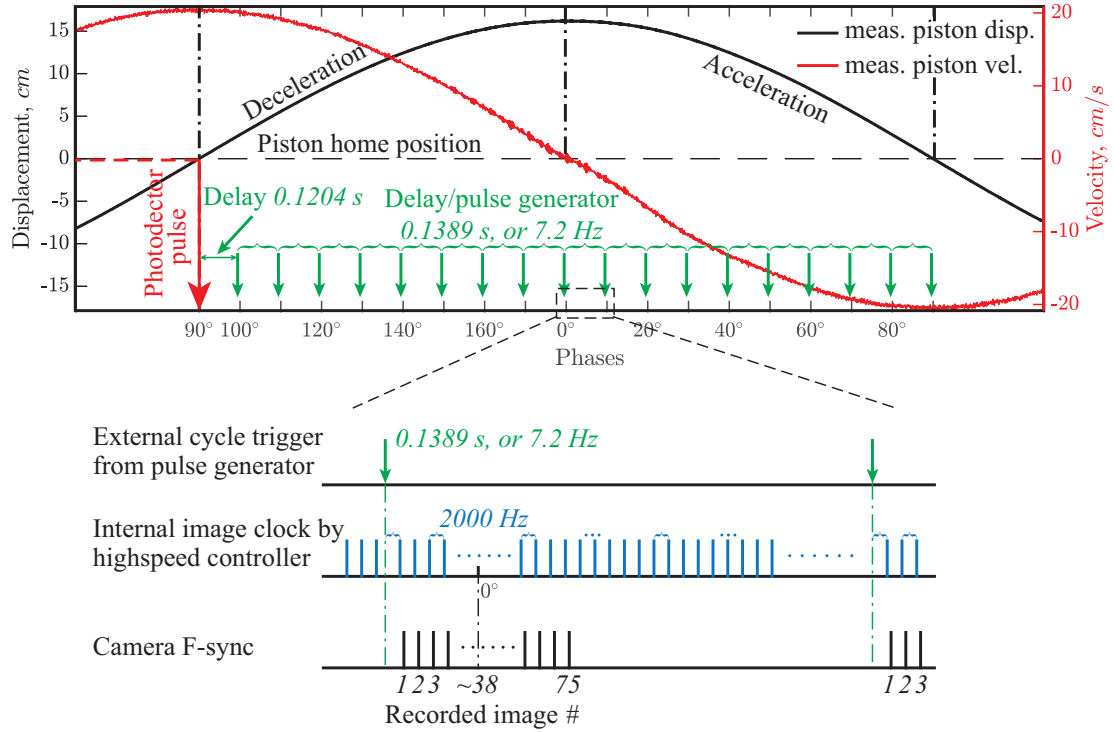


Figure 4.4: The trigger and synchronization illustration.

Figure 4.3) that the offset error is about ± 1 ms. Overall, the uncertainties in phase synchronization is estimated as ± 10 ms, or $\pm 0.72^\circ$, or ± 20 images in each time resolved measurement at each phase (2000 Hz imaging frequency and 75 images in total).

Each experimental run consists of 20 cycles of piston motion and data acquisition starts and ends within 15 ~ 19 cycles of piston motion. 15 cycles are waited before taking measurements to ensure the oscillatory sheet flow has reached a steady transient state. Constrained by the camera memory, images are acquired for three sequential half cycles within a single run and a total of 28 independent runs were conducted, which results in a total of 84 independent time-resolved measurements (75 images) at each phase to converge the statistics. The static sediment bed height

is used as a reference height (defined as $y = 0 \text{ mm}$) when reporting the results and thus is monitored before and after each run. The sediment bed is re-filled every 25 experimental runs to ensure an insignificant overall change in the bed height (within 5 mm).

4.1.3 Tracer particle: fabrication and seeding

Due to the scale of our experimental facility, large amounts of fluorescent tracer particles are required. The cost of commercial fluorescent tracer particles can be prohibitive, so mass production of fluorescent tracer particles inexpensively and in-house would be desirable. The detailed fabrication procedures can be found in Pedocchi et al. [113] and Washuta [114], and thus are only briefly described in the following. The fluorescent tracer particles were made by thoroughly mixing the fluorescent dye (Rhodamine WT) with two-parts epoxy (MAS) in a pan left to be cured. Then the hardened mixture is ground with a belt sander into a wide range of polydispersed particles, which are subsequently sieved into different size ranges. The size of the fluorescent tracer particles used in the current study are the ones sieved down to $25 \sim 53 \mu\text{m}$. The specific gravity of tracers are estimated as $SG_{tr} = 1.13$.

A reliable measurement of the carrier phase flow requires a relatively high seeding density, as the sediment clouds can both diminish and contaminate the tracer particle signals (obscuration and “cross-talk”). It has been shown in section 3.4 that with 1% volumetric fractions of sediment particles, half of tracer particles are not detected either due to direct obscuration by sediment particles or being merged into

the high background noise created by the scattered light from out-of-plane sediment particles. In contrast to this, a dense seeding of tracer particles in the entire fluid volume could degrade the light sheet quality, resulting from the fact that the sheet must propagate through 30 *cm* of fluid prior to reaching the measurement region, as shown in Figure 4.5. A thickened light sheet due to diffusion by tracer particles is unfavorable for both sediment reconstruction and stereoscopic PIV implementation. In order to solve the above dilemma, a local seeding scheme was designed to seed directly to the imaging region immediately prior to the start of image acquisition, as illustrated in Figure 4.5. A thin seeding rod (made of copper, 3 *mm* in diameter) is inserted into the tunnel from the bottom of the test section through the sediment bed, which is allowed to slide in the vertical direction. Concentrated seeding solution is injected during the 9th through 13th cycles of piston motion, right before image acquisition. The seeding rod is slid upwards to the static bed level and a syringe is used to slowly inject suitable amount of tracer particles into the imaging area. Once seeding is finished, the seeding rod is retracted back in the non-mobile sand layers to avoid any intrusions in the flow during measurement. An additional three cycles are used following injection and retraction to wash out the disturbance to the flow and permit the tracers to mix uniformly throughout the volume of fluid to be measured. As more and more measurements are conducted, tracers are accumulated in the flow, which has the potential to degrade the light sheet quality. To prevent this from happening, the light sheet is monitored by checking its thickness projected on the static bed from the self-calibration images. No noticeable changes in the light sheet thickness were detected for at least 13 consecutive runs (i.e. seeding for 13

times), which corresponded to the water change interval for the experiments.

4.1.4 Camera calibration and planar self-calibration

Calibrating the recorded images consists of two steps. Step one is the camera calibration, in which a calibration target with regular dot patterns are simultaneously registered by the three cameras at different depth locations to gain a correspondence between the 3D world coordinates (established by the calibration target) and the 2D pixel coordinates in each camera. In order for the the calibration target to be optically accessible for cameras on both sides of the target, the dot pattern is printed on a transparent paper and sandwiched between two glass slides (0.3 mm thick each) to ensure the flatness of the dot pattern, see Figure 4.6. The calibration target is secured on a translation stage (see Figure 3.9) and is precisely translated to eleven different depth locations ($z = -1.5 \sim 1.5\text{ mm}$) with an incremental displacement of 0.3 mm . At each depth location, third order polynomial mapping functions are used to fit between the world coordinates and the camera pixel coordinates. Step two is called the planar self-calibration (Wieneke [97]), in which the established world coordinate system (by camera calibration) is adjusted via translation and rotation, such that the $z = 0\text{ mm}$ plane coincides with the light sheet center, according to the disparity map computed between pairs of dewarped images from any two cameras. The self-calibration images contain only the tracer particles in order to have a better representation of the light sheet position and are acquired separately with an exceedingly low external flow speed that is below the incipient threshold of

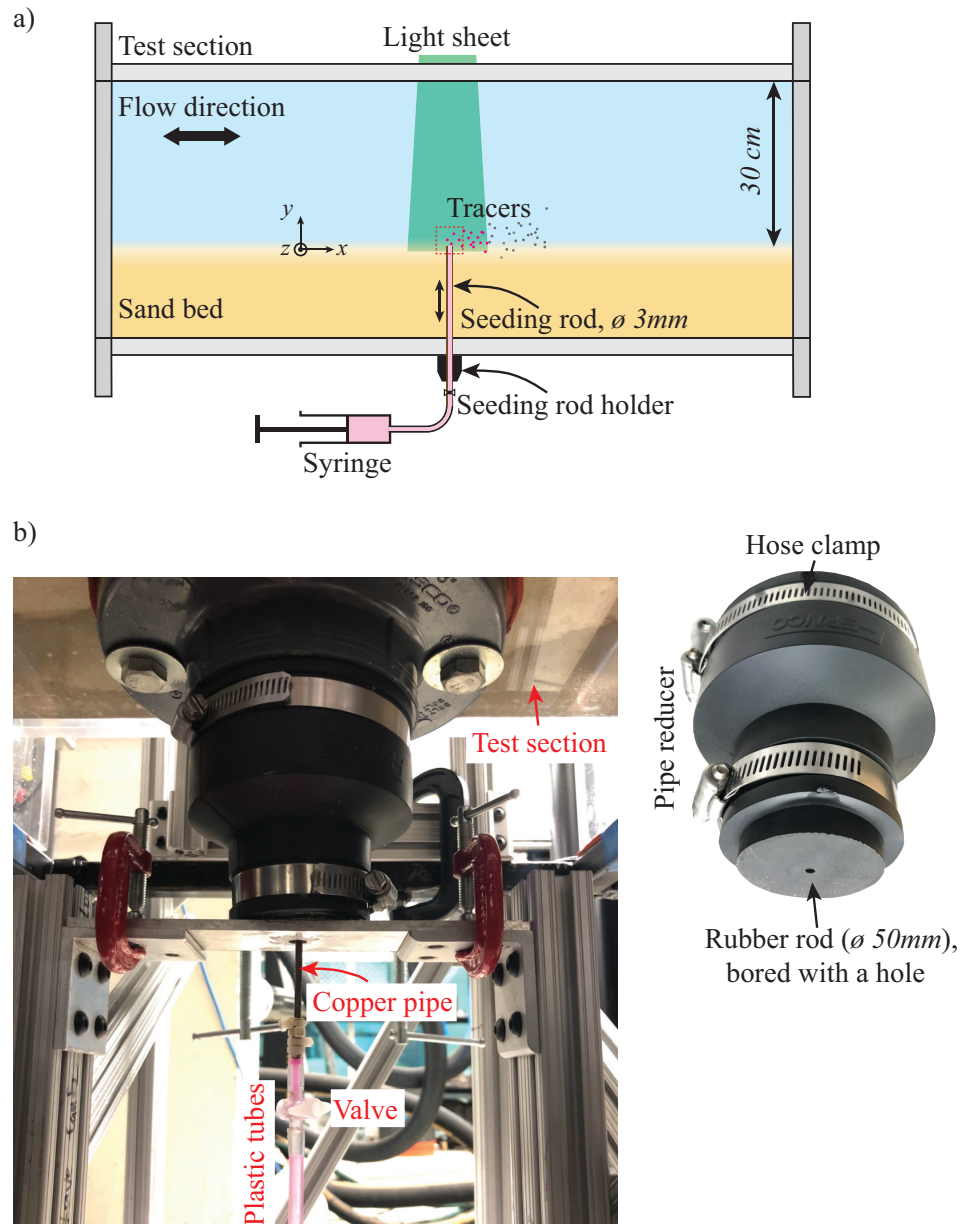


Figure 4.5: a) Schematic and b) the actual photo of the seeding system, mainly consisting of the retractable seeding rod and its corresponding holder and tubings.



Figure 4.6: Photo of the printed calibration target on a transparent polymer film sandwiched between two glass slides.

sediment motion. Planar self-calibration is computed using the commercial software package DaVis (version 10, LaVision), in which each pair of the three camera images is used to compute the disparity map, based upon which an optimized adjustment of the coordinate system is computed to modify the mapping functions of all the three cameras altogether. Finally, a consistent world coordinate system with $z = 0\text{ mm}$ coinciding the light sheet center is established along with its correspondence to the pixel coordinates in each camera. The camera calibration images are acquired every time after the sand bed is refilled to account for possible camera vibrations during refill and the planar self-calibration images were acquired twice each day and the light sheet and camera positions were assumed to be unchanged throughout the day. Images acquired in different days use their own calibration functions, though only a small variance was observed in the day-to-day calibration results. The final field of view, determined by the common area shared by at least two cameras, is $32 \times 33\text{ mm}^2$ and the resultant spatial resolution is 40.4 pixels/mm .

4.2 Data process and uncertainties quantification

Discrete particle tracking for the sediment phase and Stereoscopic PIV for the carrier phase were performed with the time resolved measurements (75 images at 2000 Hz) at each phase. For the sediment phase, the particles were first identified with their centroid locations and characteristic size and brightness determined in each camera (Khalitov and Longmire [72]). Then an algorithm adapted from the “shake-the-box” method (STB, Schanz et al. [1]) was implemented to simultaneously reconstruct the 3D positions of the sediment particles and search for their temporal trajectories. A novel 3D reconstruction technique is applied that is more suitable to tackle large particles (10 \sim 15 *pixels* in diameter, ten times larger than the tracer particles), in which the stereoscopic correspondences were established by inspecting the triplets formed by each sediment particle after being dewarped and projected onto $z = 0\text{ mm}$ plane. This process was facilitated by screening the candidate matchings according to the particles size and brightness. The details of the above methods and the preliminary processed results were elaborated in Chapter 2. In order to resolve the instantaneous carrier phase velocity field, the tracer images need to be extracted to eliminate the cross-talk from the sediment signals before being sent to Davis 10 for stereoscopic PIV process. A new image processing technique, named “MFS+mask”, is implemented for the filtration of sediment signals, which is discussed in detail in Section 3.5. The rest of this section analyzes the uncertainties associated with the measured kinematics of both phases in the actual sheet flow.

4.2.1 Sediment particle kinematics

Once the sediment trajectories are acquired, the computation of the sediment velocity is a trivial task by directly differentiating the positions with respect to the corresponding time interval using finite difference schemes. However, even very slight uncertainties in the positions can be amplified to a significant level after differentiation. To achieve a highly accurate 3D position reconstruction with sediment particles is even more challenging due to the inevitable large uncertainties when determining the particles centroid locations in each camera as a result of their large apparent sizes and irregular and variable image patterns, as demonstrated in Figure 2.8. When evaluating the kinematic error (position, velocity or acceleration) associated with a particle in actual sheet flow measurements, the ground truth value is typically unknown, so the error has to be estimated. The temporal coherency expected by each particle is utilized for the estimation. This is done by fitting a smooth polynomial curve to the measured kinematic track along a particle trajectory, from which the kinematic error was estimated as the deviation of each individual point from the fitted curve. The errors computed in this way represent our best expected approximation to the true error and will be consistently adopted in this section.

Figure 4.7 shows the temporal evolution of the 3D positions of a single sediment particle during flow reversal within an actual sheet flow measurement, which has a median trajectory length (tracked over 15 consecutive time steps) and represents a typical sediment trajectory. The y - position denotes the particle's distance to the static sediment bed and $z = 0\text{ mm}$ corresponds to the light sheet center. It

is shown in the figure that most of the position errors, defined as the deviations of the measured positions with respect to the fit polynomial curves, are contained within $\pm 10 \mu m$ or $\pm 0.4 pixels$ in all three directions, corresponding to 4% of the sediment particle diameter. The position error is comparable to the one obtained in the conventional “shake-the-box” method (Schanz et al. [1]), after normalizing their position errors (also estimated as the deviations in the tracer particle position from the fit B-spline curve) by the corresponding particle mean diameter. However, this is still not accurate enough to produce a relatively smooth velocity curve after discrete differentiation. Two methods are proposed and tested in order to further reduce the noise in the velocity measurement and the same particle trajectory, as shown in Figure 4.7, is used to explain the two methods and assess the velocity uncertainties associated with each one.

4.2.1.1 Trajectory based velocity computation

The first method is to first fit a polynomial or spline curve to the measured trajectory and then velocities are computed by differentiating the fitted smooth curve (trajectory based). This is a common practice utilized in 3D particle tracking technique (Schanz et al. [1], Ouellette et al. [115] and etc.). In the current study, polynomials of different orders were used to fit each trajectory in each direction. The orders used for polynomial fit should depend upon the trajectory length and be able to capture the general shape of the trajectory. Based on an empirical observation, for trajectory lengths smaller than 20 samples (corresponding to a time duration

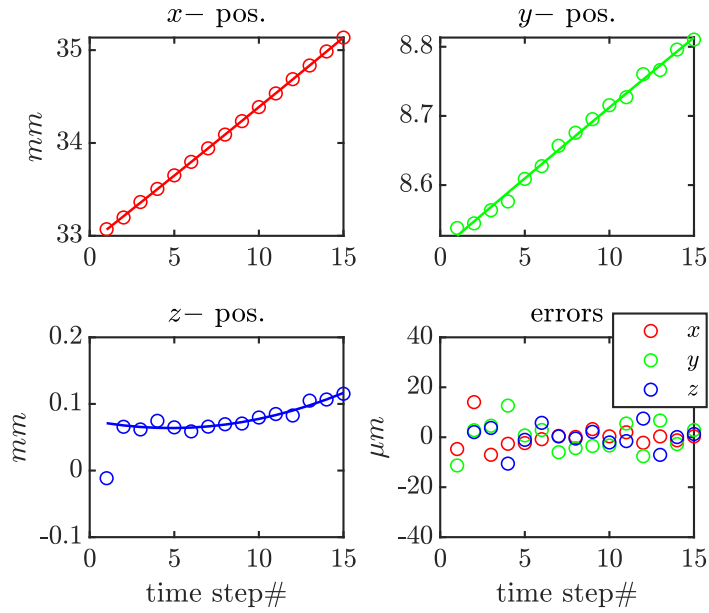


Figure 4.7: The trajectory of a sample particle, decomposed in x -, y - and z - directions. The circles represents the reconstructed particle’s instantaneous positions and a second order polynomial is fit to these positions in each direction, denoted by the solid lines. The fitting errors are also shown in the figure. The same particle is also used in Figure 4.8.

of $< 10\text{ ms}$), second order polynomials are sufficient; for lengths between 20 to 40 samples ($10\text{ ms} \sim 20\text{ ms}$), third order polynomials are used and fourth order polynomials were implemented for even longer trajectories ($40 \sim 75$ samples, or $20\text{ ms} \sim 37.5\text{ ms}$). Theoretically, this is also deemed as a reasonable fit given that the particle’s response time is 5.64 ms . It is shown in Figure 4.7 that the polynomial fit can capture the shape of the particle trajectory with high fidelity, with root-mean-squared errors around $8\ \mu\text{m}$ in each direction. The velocities can then be computed by differentiating the fitted smooth polynomial curves in each direction, as will be shown by the red solid lines in Figure 4.9.

4.2.1.2 Cross-correlation based velocity computation

The second method relies on image correlation to first obtain a more accurate measurement of the sediment particle's 2D displacement (in *pixels*) in each camera, and then the 3D velocity vector under world coordinates can be derived according to the particle's 2D displacement from different perspectives and the calibration function (cross-correlation based). The same particle trajectory as depicted in Figure 4.7 is used to demonstrate the 2D cross-correlation results, as presented in Figure 4.8. For the particle at each position on the trajectory, its associated raw particle image in each camera is extracted by cropping the raw image with a square window centered at the identified particle centroid location. Cross-correlation is performed between each pair of extracted particle images separated by a prescribed time interval ($dt = 1\text{ ms}$). The cropped window size (equivalent to the interrogation window size) is selected to be the particle image diameter. In Figure 4.8 (top two rows), the extracted sediment particle images are contained within the green boxes, where cross-correlation is performed. The red circles denote the centroid locations of the identified sediment particle in each camera and the red arrows indicate the particle displacement in each camera by direct subtraction of centroid locations between each image pair.

It has been demonstrated in Figure 2.8 that large uncertainties up to 3 pixels can be detected in the computed sediment particle centroid locations due to effects such as non-uniform illumination, overlapping with and obscuration by the surrounding particles. The advantage of 2D cross-correlation lies in that its accu-

racy doesn't depend on the accuracy of particle's centroid locations and only uses them as a predictor to search for the interrogation region. As long as the particle image pattern remains relatively unchanged between image pairs, irrespective of how irregular the image pattern is and how large the centroid location error is, cross-correlation should be able to produce accurate displacement measurements. In conventional planar PIV, 0.1 pixels error can be achieved under suitable imaging conditions, usually with a 32×32 interrogation window size containing ~ 8 uniformly distributed tracer particles with image diameters of $2 \sim 3$ pixels. The current imaging condition (top two rows in Figure 4.8) is completely different from the one stated above and renders a much worse condition for the implementation of cross-correlation. An increased displacement errors is inevitable, which will be quantified in the next paragraph. The resultant cross-correlation map is also shown in Figure 4.8. It is shown that the cross-correlation map indeed generates a broader peak than conventional PIV does. Sub-pixel resolution is computed using Gaussian fit near the correlation peak. The peak with sub-pixel accuracy is shown by the white arrow in each correlation map, which is roughly equal to the correction made by the cross-correlation method to the displacement computed by direct subtraction of centroid locations.

The 2D displacement of the particles (in *pixels*, within 1 ms) in each camera computed by cross-correlation and direct subtraction is compared in the bottom two rows in Figure 4.8. It is shown that the non-physical fluctuations in the displacement still exists even with the cross-correlation method, whose overall fluctuation level is only slightly lower than direct subtraction method. It is worth noting the obvious

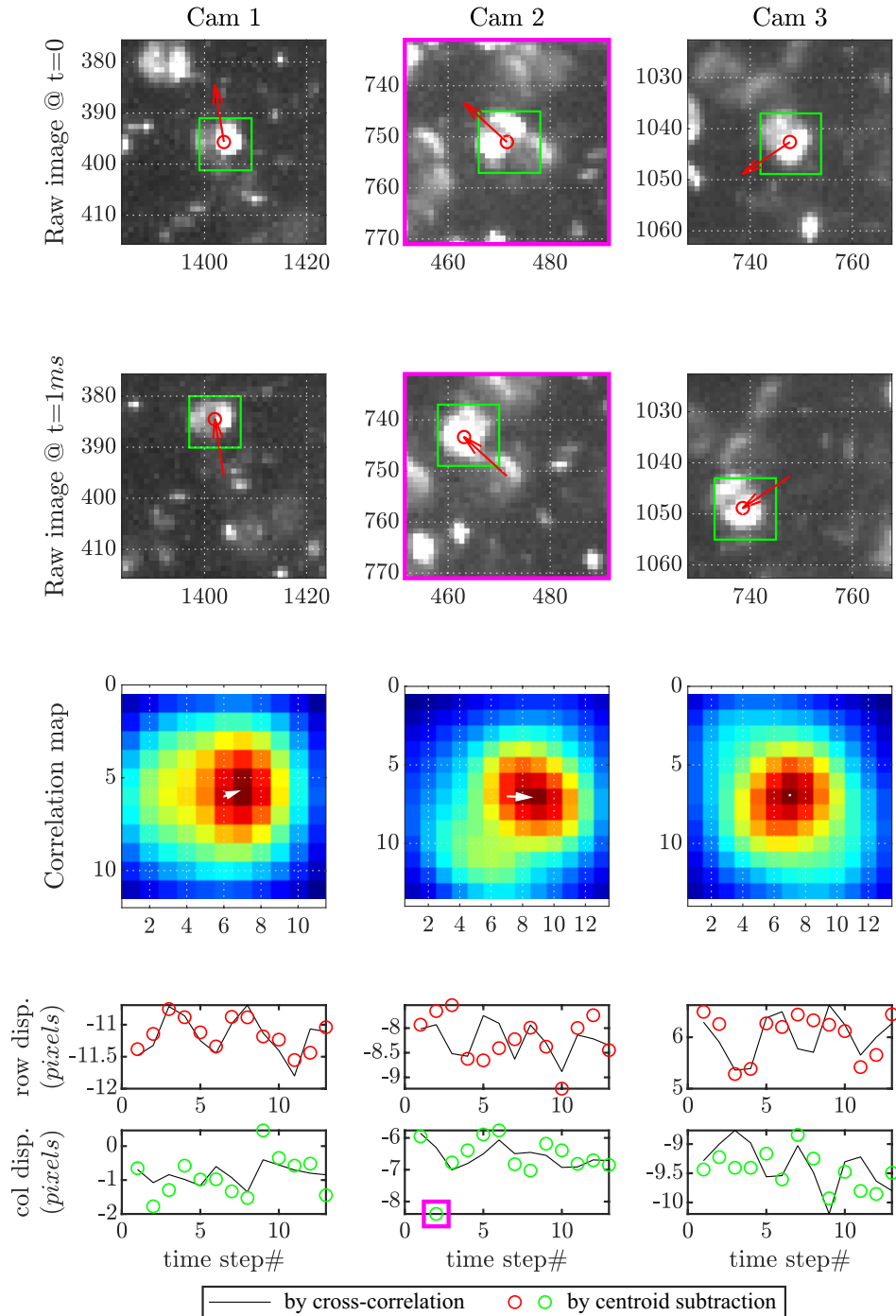


Figure 4.8: Top two rows show the raw images zoomed in near the particle under investigation. Cross-correlation is performed between the extracted particle images, which are defined as the cropped region inside each green box, to compute the sediment displacement (in *pixels*) in each camera. Red arrows show the displacement computed by direct subtraction of identified particle centroid locations. The third row shows the correlation maps with white arrows denoting the computed peak locations with sub-pixel accuracy. The bottom two rows compare the row and column particle displacement computed by cross-correlation and by direct subtraction. A particle with median trajectory length (= 15) is used for demonstration.

outlier in the column displacement detected in the second camera (marked by the magenta box) is corrected by the cross-correlation method. This point corresponds to the displacement between the two particles shown in the upper two rows in the same figure, also boxed with magenta color. The outlier is a direct result of the wrong identification of the particle's centroid location at the first time step (labelled as $t = 0$) due to another particle in the background falsely identified as part of this particle. Such errors, even though very rare, can be reliably corrected by the cross-correlation method. Figure 4.8 (bottom two rows) shows that the 2D cross-correlation uncertainty (estimated by the noise level) is around $\pm 0.3 \sim \pm 0.4 \text{ pixels}$ in each camera, which is reasonably accurate considering that the sediment particle images are not ideal for cross-correlation and that there exists some degree of dynamical change of the particle's image patterns between image pairs.

Once the particle's 2D displacement (in *pixels*) in the three cameras are computed by cross-correlation, the calibration (or mapping) functions are used to compute the three components (x -, y - and z -) of the particle's velocity under world coordinate system (in cm/s). The mapping functions are calculated by Davis ¹⁰ accounting for the results of both camera calibration and planar self-calibration. The mapping functions use a common world coordinate system for the three cameras (with $z = 0 \text{ mm}$ coinciding with the light sheet center) and fit third order polynomials to map the world coordinates (x, y) at each discrete z - plane to the pixel locations (C, R) in each camera, which can be expressed as the following:

$$\begin{bmatrix} C^i \\ R^i \end{bmatrix} = \vec{F}^i(x, y, z = z_a), \quad z_a = -1.5, -1.2, \dots, -0.3, 0, 0.3, \dots, 1.2, 1.5 \text{ mm} \quad (4.1)$$

where the superscript i represents the camera number and z_a corresponds to the translated calibration target locations and are the planes where the third order polynomial mapping functions are available. The gradient of each mapping function $\nabla \vec{F}^i$ (i.e. the first order Taylor expansion of \vec{F}^i) can be used to map the particle's 3D displacement $(\Delta x, \Delta y, \Delta z)$ to its 2D displacement $(\Delta C^i, \Delta R^i)$ in each camera, which is adequately accurate for fairly small displacement as used in the current application. The gradient matrix, $\nabla \vec{F}^i$, has 2×3 components and is evaluated at the particle's instantaneous in-plane location and on the nearest z_a - plane, i.e. at $x = x_p, y = y_p, z = z_{a_0} \approx z_p$, where (x_p, y_p, z_p) represents the particle's instantaneous 3D position. Central finite difference with a step size of $\pm 0.3 \text{ mm}$ is used to calculate the derivatives in the z - direction. The system of linear equations mapping between a particle's 3D displacement and 2D displacement in multiple cameras can be combined and written as,

$$\begin{bmatrix} \Delta C^1 \\ \Delta R^1 \\ \Delta C^2 \\ \Delta R^2 \\ \dots \end{bmatrix} = \nabla \vec{F} \cdot \begin{bmatrix} \Delta x \\ \Delta y \\ \Delta z \end{bmatrix} \quad (4.2)$$

for forward mapping, and

$$\begin{bmatrix} \Delta x \\ \Delta y \\ \Delta z \end{bmatrix} = (\nabla \vec{F})^{-1} \cdot \begin{bmatrix} \Delta C^1 \\ \Delta R^1 \\ \Delta C^2 \\ \Delta R^2 \\ \dots \end{bmatrix} \quad (4.3)$$

for backward mapping, where $\nabla \vec{F}$ is a 4×3 or 6×3 matrix depending upon the number of cameras used and defined as follows:

$$\nabla \vec{F} = \begin{bmatrix} \nabla \vec{F}^1 \Big|_{x=x_p, y=y_p, z=z_{a_0}} \\ \nabla \vec{F}^2 \Big|_{x=x_p, y=y_p, z=z_{a_0}} \\ \dots \end{bmatrix} \quad (4.4)$$

and $(\nabla \vec{F})^{-1}$ represents its pseudo inverse matrix.

Given the 2D displacement in at least 2 cameras $(\Delta C^1, \Delta R^1, \Delta C^2, \Delta R^2, \dots)$, equation 4.3 solves for the corresponding 3D displacement. This equation is an over-determined system of linear equations and can only be solved in the least-square sense. The residuals of the least-square fit (also termed as the “reconstruction error”), ξ_{resid} , can be used as a measure of the quality of the 3D reconstructed displacement vector $(\Delta x, \Delta y, \Delta z)$, making it appropriate for sanity check. The 3D displacement is computed using each pair of cameras and only the pair generating the smallest reconstruction error, ξ_{resid} , is selected to exclusively determine the particle’s

3D displacement. A reconstruction error of less than 1 *pixel* can be achieved in at least 95% of the velocity reconstructions, which is a typical error threshold used in stereoscopic PIV process.

The instantaneous velocities computed by the above cross-correlation method ($dt = 1\text{ ms}$) form velocity tracks associated with each sediment particle trajectory. The temporal coherency exhibited by each sediment particle allows us to further de-noise the directly measured instantaneous velocities. A sliding average of length three is applied to each velocity track, which acts in effect as a low pass filter with a cutoff frequency (half power point) of 313 Hz to suppress the high frequency random noise, which is legitimate given the particle's response time of 5.64 ms (or 177 Hz). The resultant velocity track in each direction for the same sediment particle as studied above is shown in Figure 4.9, which are denoted by the black circles. In comparison to the cross-correlation based velocities, the trajectory-based velocities are superimposed as the red lines.

The velocity uncertainties associated with the cross-correlation based method are evaluated by inspecting the deviation of individual velocities from their polynomial fit, which is denoted as the black lines in Figure 4.9. One less polynomial orders are used to fit the velocity tracks than the ones applied to the corresponding trajectories, as elaborated in Section 4.2.1.1. The red circles represent the velocities computed by direct subtraction of the reconstructed particle positions separated by $dt = 1\text{ ms}$ and then smoothed by a sliding average of length three. These velocities (red circles) are compared to the trajectory-based results and their deviations are used for quantifying the uncertainties associated with the trajectory-based method.

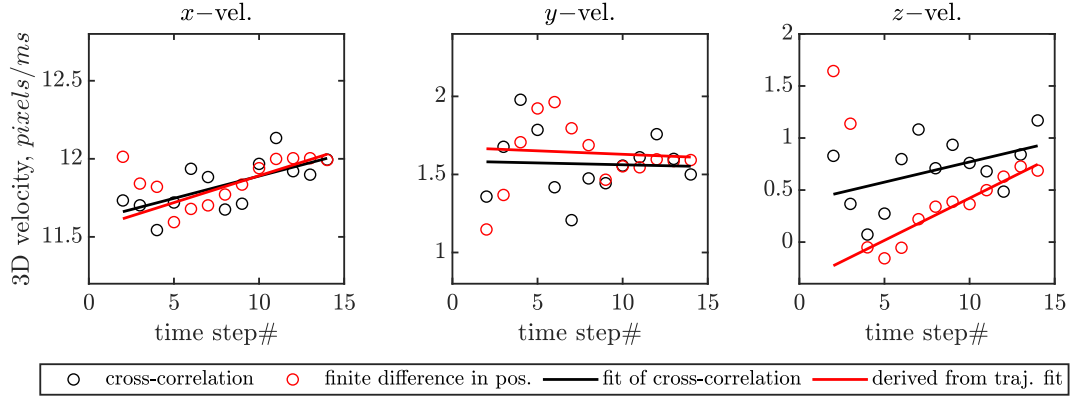


Figure 4.9: The 3D velocity vectors computed by the proposed two methods, cross-correlation based (\circ) and trajectory-based (---). The velocity data is presented as the pixels the particle traveled within 1 ms . The same sediment particle as depicted in Figure 4.8 is used.

It is observed that aside from the few outliers exhibited by the trajectory-based results (the two in the z -velocity), most of the noise fluctuates within ± 0.3 pixels in the x - and y - directions and ± 0.5 pixels in the z - direction. It is also found that for this particular trajectory, the noise levels in the velocity measurement are comparable between the two methods and a more comprehensive statistical analysis is needed to determine if one is more accurate than the other to any degree of statistical significance. It is worth mentioning that the fitted velocity curves between the two methods are fairly close, especially in the in-plane directions.

4.2.1.3 Evaluation of the two methods

Statistical error analysis is conducted to compare the two proposed velocity computational schemes and provide an error bound estimate for the current sediment kinematics measurement. The statistics are computed by examining all the trajectories detected in one run (75 time steps) at phase 0° . To estimate the errors (or noise

level) of the computed particle positions and velocities, the same method is adopted as illustrated in Figures 4.7 and 4.9, in which polynomials are fit to the scattered data points and the resultant fitting errors are used to estimate the uncertainties in measurement. The statistical errors are computed separately for trajectories located at different heights from the static bed with a binning size of 2.5 mm . It should be expected that the kinematics should show decreased uncertainties far away from the bed where the sediment concentration is sufficiently low to guarantee a relatively simple illuminating environment without much multi-scattering effects, and an increased noise towards higher concentration regions closer to the bed, where the effect of the surrounding particles starts to become evident creating tracking ambiguities and lighting contaminations (overlapping or obscurations).

It is shown in Figure 4.10 that for particles located more than 20 mm above the bed, where the sediment concentration is below $C = 0.05\%$, very accurate position and velocity measurements can be achieved with both velocity computational schemes. For the cross-correlation based measurement, 1 mm/s and 2 mm/s mean absolute errors in the in-plane directions and the out-of-plane direction can be achieved respectively. For particles located between 3 mm and 20 mm above the static bed ($C \leq 1\%$), the average absolute position errors are approximately $6\text{ }\mu\text{m}$, $6\text{ }\mu\text{m}$ and $8\text{ }\mu\text{m}$ in the x -, y - and z - directions respectively, corresponding to a total absolute position error of 0.3 pixels , or 5% of sediment particle mean diameter. For the velocity measurement, the cross-correlation based measurement shows a consistent yet slight advantage over the trajectory based measurement at almost every height. For sediment particles located between 5 mm and 20 mm above the

static bed ($C \leq 0.4\%$), absolute velocity errors of 6 mm/s in the in-plane directions and 10 mm/s in the out-of-plane directions can be achieved with the cross-correlation based measurement, which respectively correspond to 2.4% and 4% of the maximum absolute velocities exhibited by the sediment particles. The acceleration errors shown in Figure 4.10 are directly derived from the velocity uncertainties by dividing the mean absolute velocity errors at each elevation by a prescribed time interval of 2.5 ms , assuming only trajectories with lengths larger than seven are used for acceleration evaluation.

Even though the cross-correlation based method only shows a slight improvement in the accuracy of the velocity measurement, it is still worth mentioning some of its major advantages over the alternative: 1) The cross-correlation based method is less prone to particles centroid errors and can function well even with incorrectly matched particles in one of the three cameras. This is mainly due to its flexibility in choosing the pair of cameras to use when reconstructing the 3D velocities and the pair with the smallest reconstruction error can usually eliminate the erroneous 2D vectors computed in one of the cameras. As a result, it reduces the velocity measurement noise level by approximately 50% at some elevations. 2) If the tracking ambiguity errors are disregarded, the cross-correlation method offers the most accurate measurement of the instantaneous sediment velocity one can achieve using current measurement technique. The cross-correlation method consists of two steps: i) 2D cross-correlation, which already represents the state-of-the-art image pattern matching method; and ii) 3D velocity reconstruction. The only source of error in the second step is from the calibration function, whose errors typically can be ne-

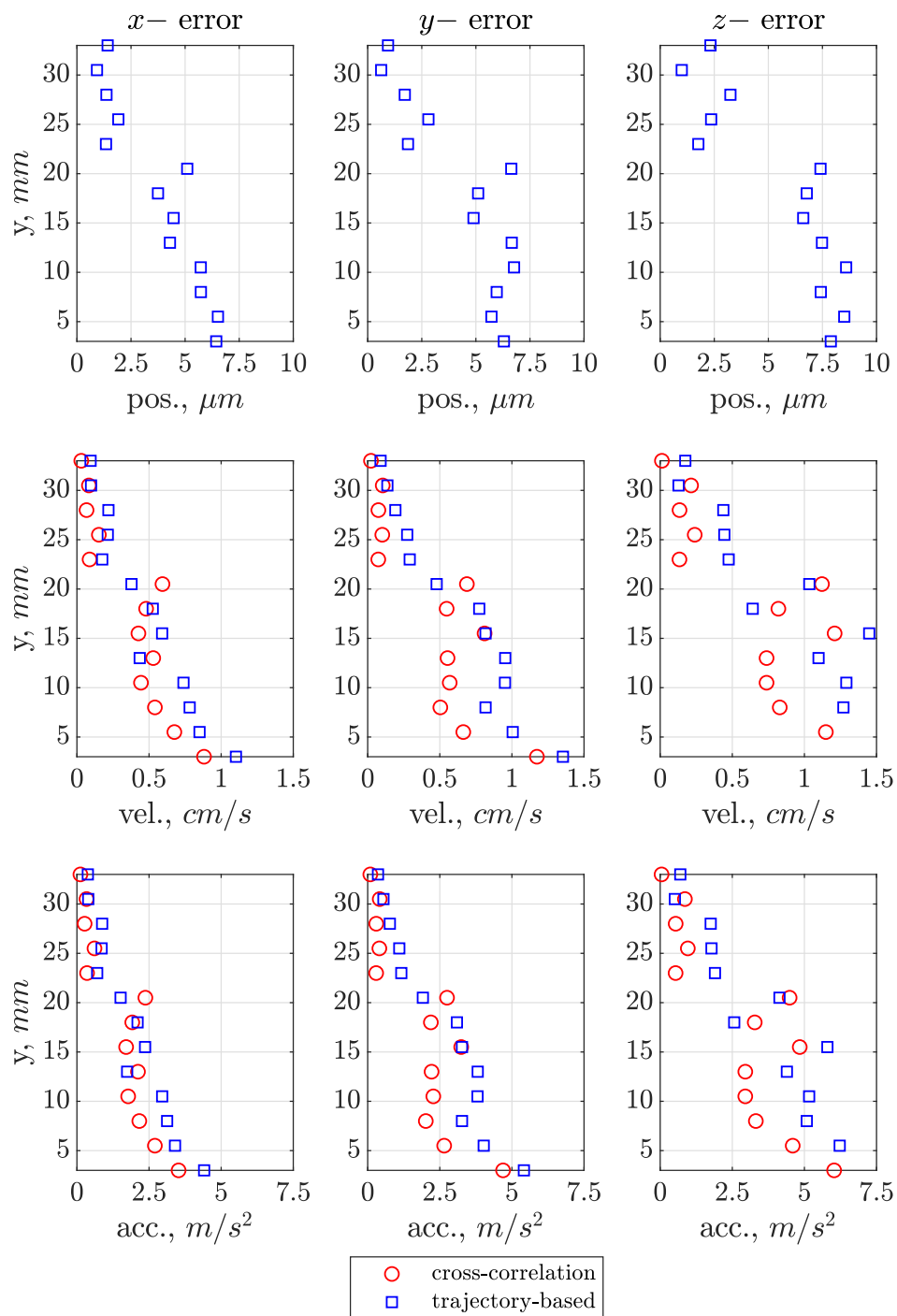


Figure 4.10: The statistics of the sediment particles kinematics error as a function of their distance to the static bed.

glected in comparison to the other sources of error. When presenting the sediment velocities in Section 4.3, the cross-correlation based measurement smoothed by sliding average of length three is adopted, whose mean absolute errors are estimated as 6 mm/s in the in-plane directions and 10 mm/s in the out-of-plane directions for all the trajectories with $y \geq 5\text{ mm}$.

4.2.2 Carrier phase velocity

In order to compute the carrier phase velocity, the sediment particles were first eliminated from the acquired raw images by implementing the image processing technique named “MFS+mask”, which has been elaborated in Section 3.5. The filtered images were then directly fed to Davis 10 for stereoscopic PIV processing, with a time separation of $dt = 1\text{ ms}$ and multi-pass vector calculation using interrogation window sizes decreasing from 96×96 to 64×64 (50% overlap). The final pass (64×64) determines the spatial resolution of the computed carrier phase velocities and corresponds to 1.58 mm , approximately the same as the local light sheet thickness. A smaller interrogation window (32×32) can also output reasonable velocity vectors with a slightly higher number of spurious vectors, however the in-plane resolution is constrained by the local light sheet thickness and should be at least the same as that to ensure a well-defined measurement volume according to Raffel et al. [116]. A sub-millimeter light sheet thickness is difficult to maintain in the current application mainly due to bed reflections and multi-scatterings from the sediment particles especially near the bed. A maximum reconstruction error of 1.0 pixel is

allowed and only velocity vectors satisfying this criteria are computed. The overall percentage of detected spurious vectors in each instantaneous velocity field are typically within 5%. At each location, velocities are computed between each pair of cameras, and the pair generating the least uncertainties are exclusively used for the local velocity measurement (see Section 3.5). The resultant uncertainties associated with the carrier phase measurements have been carefully quantified in Section 3.5, and it has been shown that under the concentration of interest ($C \leq 1\%$), a mean absolute error of 0.2 pixels in the x - and y - directions and 0.3 pixels in the z - direction can be achieved, corresponding to measurement errors of 5 mm/s and 7.5 mm/s respectively. In the future, in order to further increase the spatial resolution, shake-the-box based particle tracking method can be implemented to the tracer particles. The tracer identification algorithm proposed in Section 3.4 can be used for tracer particle identification and the resolved carrier phase by stereoscopic PIV processing can be used as a reliable predictor in 3D particle tracking.

4.2.3 Statistics calculation

The coordinate system consistently used when reporting the measured quantities is shown in Figure 4.11, in which x - is the streamwise direction, y - is the normal-to-bed direction and z - is the spanwise direction. $z = 0 \text{ mm}$ corresponds to the light sheet center, which is in the middle of the test section; and $y = 0 \text{ mm}$ corresponds to the static bed height before experiment starts. The homogeneity of flow in both x - and z - directions were validated in the work of Knowles [70]. The

instantaneous velocities decomposed in the x -, y - and z - directions are denoted as U , V and W respectively, with subscript “ f ” referring to flow properties and “ p ” the sediment particle properties. An overbar, “ $-$ ”, is used to indicate phase averaged quantities, which is defined as:

$$\overline{\Psi}_f(y|\varphi) = \frac{1}{N} \sum_{i=1}^N \frac{1}{\Delta x \Delta t} \int \int \Psi_{f,i}(x, y, t|\varphi) dx dt \quad (4.5)$$

for an instantaneous flow variable under field representation, $\Psi_f(x, y, t)$. In the above equation, $\varphi = 0^\circ \sim 170^\circ$ indicates the phase angle being averaged, $\Psi_{f,i}$ denotes the flow field quantity acquired at the i th realization from an ensemble of $N = 84$ independent realizations, $\Delta t = 37.5 \text{ ms}$ is the time duration of each time-resolved measurement at each phase, and $\Delta x = 31 \text{ mm}$ is the overall width of the measurement region. To compute the average of a sediment variable, $\Psi_p(x_p, y_p, t)$, which exists only at discrete points identified as a sediment particle, a binning method is used to search and average all the identified particles contained within each horizontal bin $y - \Delta y/2 \leq y_p < y + \Delta y/2$. The vertical phase averaged profile of a quantity associated with sediment phase can be written as,

$$\overline{\Psi}_p(y|\varphi) = \frac{1}{N_p} \sum_{i=1}^N \sum_{j=1}^{N_{\Delta t}} \sum_{k=1}^{N_{ij}(y)} \Psi_{p,ijk}(y|\varphi) \quad (4.6)$$

where $N_{\Delta t} = 75$ is the total number of time-resolved images (total time steps) acquired at each phase per realization, $N_{ij}(y)$ represents the number of particles found within the bin located at height y , at the j th time step and in the i th realization,

and $N_p = \sum_{i=1}^N \sum_{j=1}^{N_{\Delta t}} \sum_{k=1}^{N_{ij}(y)} 1$. The binning height, Δy , increases from 1 to 2 mm with the elevation (y) to contain enough particles in each bin for converged statistics ($N_p > 1000$ for all bins and $N_p > 10,000$ in most bins). Since each individual sediment particle directly interacts with its local ambient flow, the statistics of a fluid quantity that are sampled only at particle's instantaneous locations (x_p, y_p) should also be studied. We refer to such a quantity as “particle-conditioned” and its instantaneous representation is denoted as $\Psi_f|_p(x_p, y_p, t)$ or $\Psi_f|_p$, whose statistics will be shown later to provide insight into the coupled dynamics of the particle and fluid motions. Its value is computed by interpolating the fluid quantity $\Psi_f(x, y, t)$, which is available on a regular Cartesian grid in the current work, to each desired particle location (x_p, y_p). The interpolated fluid quantity represents a volume-averaged one in the neighborhood of a particle and the volume of averaging depends on the interrogation window size used in the stereoscopic PIV process, which is set to be roughly the same as the light sheet thickness, resulting in a cube with sides that are six particle diameters in length. The phase average of a particle-conditioned fluid quantity, denoted as $\overline{\Psi_f|_p}$, can be defined in the same way as shown in Equation 4.6. The fluctuating component of an instantaneous quantity (Ψ_f or Ψ_p) is denoted by the corresponding lower case letter and can be expressed as $\psi = \Psi - \overline{\Psi}$. For a particle-conditioned fluid quantity, the fluctuating component is defined as $\psi_{f|p} = \Psi_f|_p - \overline{\Psi_f}$. The variance or root mean square of the fluctuating component is denoted by ψ' . Higher order statistics can be computed in the same way as expressed in Equations 4.5~4.6.

4.3 Results and discussion

4.3.1 Flow configurations

Although phase-locked time-resolved measurements were conducted for full stroke cycles, the measured kinematics can be equivalently mapped to phases within the first half of a cycle through a straightforward coordinate transformation due to flow temporal symmetry, as pointed out in Section 4.1.2. As shown in Figure 4.11, the free stream velocity during the first half-cycle accelerates from zero in the positive x -direction until reaching the maximum nominal velocity of 1 m/s , and then decelerates back to zero. Only the results at three phases are reported in this thesis, which corresponds to the three moments near flow reversal as shown in the shaded region: 1) 170° , just before the external flow ceases, 2) 0° , right when the bulk flow is momentarily at rest and 3) 10° , shortly after the flow direction reverses. The time evolution of statistics should be compared in the sequence of $170^\circ \rightarrow 0^\circ \rightarrow 10^\circ$, which will be consistently associated with a different color in all of the figures presented in this section (red \rightarrow green \rightarrow blue).

Some important parameters characterizing the fluid and sediment particle properties and the flow conditions are shown in Tables 4.1 & 4.2 respectively. The particle response time, τ_p , is computed as the time required for a single sediment particle immersed in an initially stationary fluid and released from rest to accelerate to $1 - e^{-1} \approx 63\%$ of its terminal velocity. The achieved terminal velocity is used as the particle settling velocity, W_s . The ordinary differential equation used to

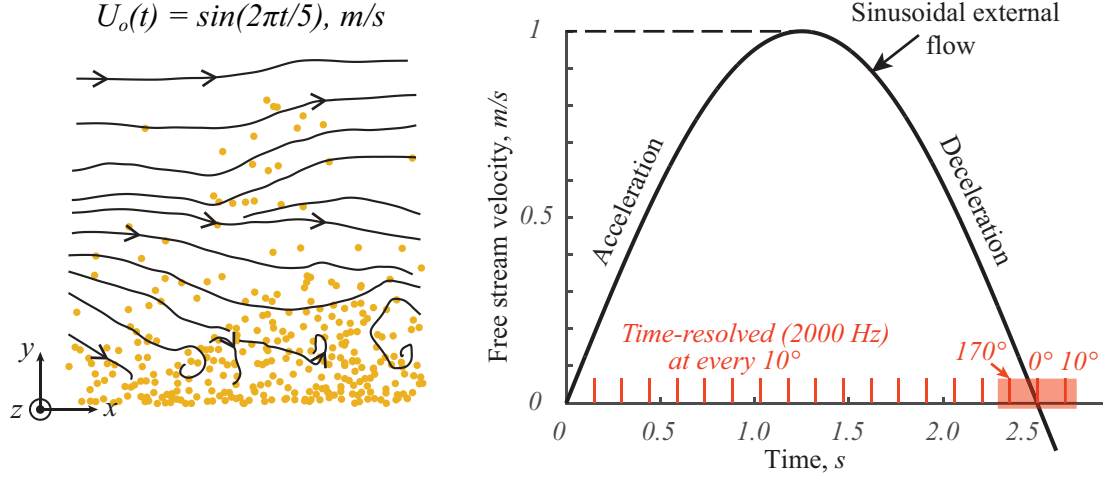


Figure 4.11: The flow configurations.

calculate the particle's instantaneous velocity, $V_p(t)$, is written as the following,

$$\frac{dV_p}{dt} = \frac{\rho_p - \rho_f}{\rho_p} g - \frac{\rho_f}{2\rho_p} \frac{dV_p}{dt} - \frac{3}{4} \frac{C_d \rho_f V_p^2}{\rho_p d} \quad (4.7)$$

$$C_d = \frac{24}{Re} (1 + 0.15 Re^{0.687}) \quad (4.8)$$

in which the buoyant, added mass, and quasi-steady drag forces are considered. The Shields parameter, θ , is estimated based upon the external flow peak velocity, $U_{o,p}$, with an empirical equation proposed by Swart [117],

$$\theta = \frac{f_w U_{o,p}^2}{2(s-1)gd} \quad (4.9)$$

$$f_w = \exp \left[5.213 \left(\frac{2.5d}{l_{se}} \right)^{0.194} - 5.977 \right] \quad (4.10)$$

where f_w is the wave friction factor and l_{se} is the semi-excursion length. Based upon the definitions introduced in Section 1.2, the other parameters in Tables 4.1 & 4.2 can be computed accordingly.

Fluid density, ρ_f	$998 \text{ kg} \cdot \text{m}^{-3}$
Fluid kinematic viscosity, ν	$9.6 \times 10^{-7} \text{ m}^2 \cdot \text{s}^{-1}$
Particle mean diameter, d	$240 \mu\text{m}$
Particle density, ρ_p	$2500 \text{ kg} \cdot \text{m}^{-3}$
Specific gravity, $s = \rho_s/\rho_f$	2.5
Particle settling velocity, W_s	3.06 cm/s
Particle response time, τ_p	5.64 ms
Particle Reynolds number, $Re_p = u_{\tau,p}d/\nu$	17.0
Wall Stokes number, $St_w = \tau_p u_{\tau,p}^2/\nu$	27.1

Table 4.1: Fluid and sediment particle parameters

External flow oscillation period, T	5 s
External flow peak velocity, $U_{o,p}$	1 m/s
External flow peak acceleration, $a_{o,p}$	1.26 m/s^2
Semi-excursion length, l_{se}	0.80 m
Bulk Reynolds number, $Re = U_{o,p}H/\nu$	300,000
Shields parameter, θ	1.31
Fall parameter, R_p	14.85
Sleath parameter, S	0.085
Bottom shear stress, $\tau_{b,p}$	4.61 Pa
Bottom friction velocity, $u_{\tau,p} = \sqrt{\tau_{b,p}/\rho_f}$	6.80 cm/s

Table 4.2: Flow condition parameters

4.3.2 Sediment concentration

Figure 4.12 shows the vertical profiles of the phase-averaged volumetric concentration in the dilute region ($C < 1\%$ and $y > 2 \text{ mm}$) at the three phases (170° , 0° and 10°) near flow reversal. A log-log scale is used in the plot such that any power law relations exhibited in the concentration distribution ($C = y^\alpha$) are manifested as straight lines and the slope represents this power, α . The concentration profiles are qualitatively the same among these three phases. In the upper dilute region, $y > 11 \text{ mm}$, the concentration decreases with height from the bed in a power law

fashion; then in the middle dilute region, $4\text{ mm} < y < 11\text{ mm}$, the curve rolls off to a steeper slope; and in the narrow lower dilute region, $2\text{ mm} < y < 4\text{ mm}$, the power law relation seems to be recovered with a noticeably smaller magnitude exponent. A decrease of concentration is observed from phase 170° to 10° at every elevation within the height demonstrated in the figure, indicating a net transport of sediment particles towards the bed (deposition) during flow reversal. Straight lines are fitted to the concentration profiles, shown as the dashed lines in the figure, both in the upper region ($y > 11\text{ mm}$) and in the lower region ($2\text{ mm} < y < 4\text{ mm}$) and their associated powers (α) are computed. From phase 170° to 10° , in the upper region ($y > 11\text{ mm}$), the absolute value of the power, $|\alpha|$, decreases from 3.47 to 2.46 indicating that the change of concentration with height becomes milder (tending toward a more uniform distribution) as the flow is reversing; on the contrast, the fitted $|\alpha|$ in the lower region ($2\text{ mm} < y < 4\text{ mm}$) is increased as one goes from 170° to 10° ($|\alpha| = 0.37 \rightarrow 1.0$, indicative of strengthening stratification of the sediment in this region). The reversed changes in $|\alpha|$ over the three reversal phases in the upper and lower regions implies different sediment particle suspension mechanisms in these two regions.

4.3.3 Mean velocities

Figure 4.13 demonstrates the phase-averaged velocity profiles (decomposed in x -, y - and z - directions) of the sediment particles (solid dots symbols) and the carrier phase (solid lines) at the three reversal phases, 170° , 0° and 10° . In the

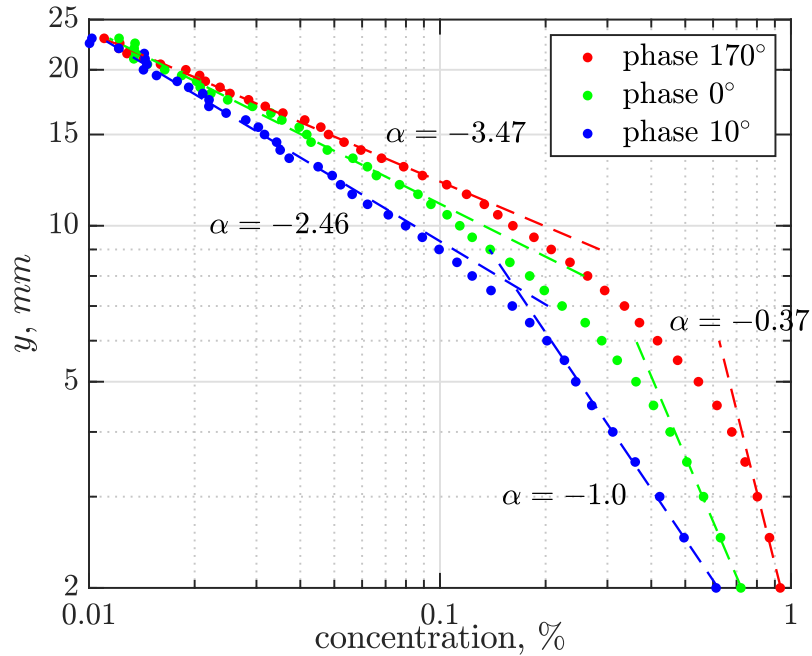


Figure 4.12: The mean concentration profiles at the three phases near flow reversal, at 170° , 0° and 10° .

streamwise direction (left plot), the carrier phase velocity profiles show the same features as those reported in a typical oscillatory turbulent boundary layer flow with non-mobile walls (Jonsson and Carlsen [118]). The flow near the bed reverses direction before the external flow does in response to the adverse pressure gradient slowing the flow, indicating that the near bed flow leads in phase. In the outer region, the flow velocity should closely match the oscillatory velocities prescribed at the corresponding phases, i.e. $U_{o,\varphi} = U_{o,p} \sin(\varphi) \text{ m/s}$, where $\varphi = 170^\circ, 0^\circ$ or 10° , however, the upper region of the mean profiles ($y = 33 \text{ mm}$) shows a distinct offset from 0 m/s expected for $\varphi = 0^\circ$, as well as for phases 170° and 10° . This is consistent with the boundary layer extending beyond the current measurement region and resulting from the characteristic “overshoot” commonly observed in oscillatory boundary layer flows. If measurements were made in higher elevations, it

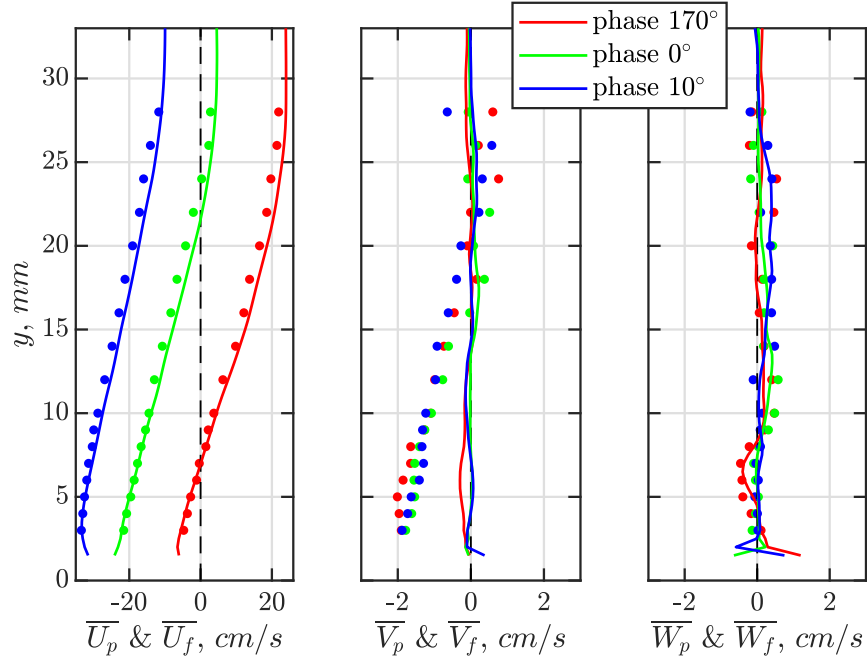


Figure 4.13: The mean velocity profiles of the sediment particles (dot symbols) and the carrier phase (solid lines) near flow reversal, at 170° , 0° and 10° .

is expected that these profiles will converge back to the corresponding prescribed velocities ($U_{o,\varphi}$). A small thus detectable difference in the streamwise mean velocity between the sediment particles and the carrier phase is shown in the figure. With such small relative velocity differences, the streamwise velocities of the two phases are speculated to be roughly in phase with each other at an all elevations. More quantitative and conclusive discussions on the phase shift should use the complete set of the acquired data at every 10° and will not be conducted in this thesis.

The normal-to-bed ($\overline{V_f}$) and spanwise ($\overline{W_f}$) phase-averaged carrier phase velocity profiles are shown in the middle and right plot of Figure 4.13. The fact that they are close to zero (within the uncertainty limits) provides convincing evidence on the homogeneity achieved in the flow in the spanwise and streamwise directions. The spanwise homogeneity can be directly inferred from the near-zero mean span-

wise velocities observed for both the sediment particles and the carrier phase at every elevation and at all three phase angles (\overline{W}_f and \overline{W}_p). The streamwise homogeneity can be validated by evaluating the averaged continuity equations satisfied by the carrier phase within the measurement region, which is written as below,

$$\frac{\partial \overline{U}_f}{\partial x} + \frac{\partial \overline{V}_f}{\partial y} + \frac{\partial \overline{W}_f}{\partial z} = 0 \quad (4.11)$$

where the Boussinesq approximation is used to neglect the effect of sediment concentration on the compressibility of the carrier phase flow, which is only valid for sufficiently low concentrations ($C < 1\%$) and is a common practice used in sediment transport models with dilute suspensions (Cantero et al. [119]). It should be noted that this doesn't justify the neglect of concentration terms in the mass equations for the sediment phase or in the momentum equations for both phases. The homogeneity of the streamwise carrier phase velocity in the streamwise direction (i.e. $\partial \overline{U}_f / \partial x \approx 0$) can be easily confirmed as a result of the last two terms being negligibly small due to $\overline{V}_f(y, t) \approx 0$ and spanwise homogeneity.

The sediment vertical (normal-to-bed) velocity profile (\overline{V}_p) shows an interesting behavior: for $y > 18 \text{ mm}$, there is a negligible mean vertical velocity observed for all three phase angles; while for $y < 18 \text{ mm}$, the vertical sediment velocity profiles for all three phase angles show a distinct downward velocity that increases approaching the bed. There is not a noticeable trend in the evolution of these profiles from $\varphi = 170^\circ$ to $\varphi = 0^\circ$, which implies that the turbulent fluctuations, which are responsible for particle suspension, are not likely to evolve much through these three phase angles.

More clues on this will be shown later with higher order statistics.

4.3.4 Sediment flux

The vertical profiles of the streamwise and normal-to-bed phase averaged sediment flux, defined as $\overline{C U_p}$ and $\overline{C V_p}$ respectively, are demonstrated in Figure 4.14. Since the sediment flux is basically the multiplication of the corresponding curves shown in Figures 4.12 and 4.13, it can be affected by the shape of either of these two curves. A general trend of the sediment flux in both directions for all the three phases is the rapid increase in the magnitude approaching the bed, which is a result of the rapid increase of concentration near the bed. An abrupt change in the streamwise sediment flux profile is observed as the flow evolves from phase 170° to the other two phases (0° and 10°). At phase 170° , sediment particles are transported in the same direction as the external flow (positive x) at heights $y > 7.5 \text{ mm}$ and in the reversed direction for $y < 7.5 \text{ mm}$, which is a result of the change in the mean flow directions (U_p). At the exact moment when the external flow ceases (phase 0°), significant sediment flux still exists near the bed ($y < 15 \text{ mm}$) and the flux is in the reversed direction (negative x). As the flow evolves from phase 0° to 10° , the streamwise sediment flux profile shows little changes due to the decreased concentration and increased streamwise velocity balancing out with each other. The sediment flux in the normal-to-bed direction is sometimes also termed as “settling flux”. In Figure 4.14 (right), the drastic increase of the settling flux as one approaches the bed is a direct result of both the increase concentration and the increased mean

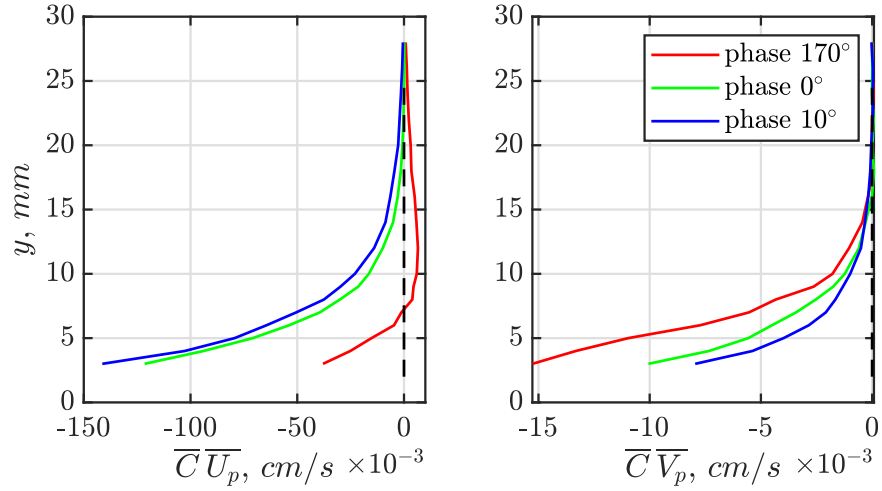


Figure 4.14: The streamwise (left) and normal-to-bed (right) mean sediment flux profile near flow reversal, at 170° , 0° and 10° .

drifting velocity in the vertical direction (\overline{V}_p). It is also shown that, as the flow evolves from phase 170° to 10° , the magnitude of the settling flux decreases at all elevations, which is mainly caused by the decreased concentrations in the flow, i.e. fewer number of particles are traveling towards the bed with similar mean drift velocities.

4.3.5 Slip velocities

Two types of particle conditioned velocity difference are defined, $\overline{U_f|_p} - \overline{U}_p$ and $\overline{U_f|_p} - \overline{U}_f$, both of which were commonly used to reveal different aspects of particle-related flow properties (Kiger and Pan [65], Berk and Coletti [68]). The former one, referred to as “particle conditioned slip velocity” following Kiger and Pan [65] represents the statistics characterizing the instantaneous local flow seen by each sediment particle. In contrast, $\overline{U_f|_p} - \overline{U}_f$ acts as an indicator of whether the sediment particles are oversampled in certain fluid regions with faster/slower

velocities in comparison to the fluid mean and will be referred to as “oversampling fluid velocity bias”. If the particles were randomly located, then the conditional average of fluid velocity, $\overline{U_f|_p}$, should show no difference from the unconditioned one, $\overline{U_f}$. The two types of particle conditioned velocity differences are decomposed in three directions ($x-$, $y-$ and $z-$) and plotted in Figure 4.15. It is here noted in advance that there is no detectable differences in these vertical profiles among the three phase angles presented, so the following discussion will focus on the features in common to all three.

In the streamwise direction, a small ($\sim 0.4 \text{ cm/s}$), uniform and consistently negative particle conditioned slip velocities ($\overline{U_f|_p} - \overline{U_p}$) can be found at all elevations within the measurement region, as shown in the left plot of Figure 4.15. This implies that the sediment particles closely follow the phase-averaged temporal variations in the flow in the streamwise direction. The exceedingly small horizontal particle-conditioned slip velocity has been verified by various experimental works both in oscillatory sheet flows (Dick and Sleath [120]) and in steady turbulent channel flows (Kiger and Pan [65]). Contrary results were found in the work of Berk and Coletti [68], who studied steady turbulent boundary layer flows with air-solid phases and found this term (under similar particle Stokes number, St_p , and particle Reynolds number, Re_p) is only negligibly small in outer regions and sharply increases as approaching to the wall and dominates over the “oversampling fluid velocity bias” term ($\overline{U_f|_p} - \overline{U_f}$) in the near wall region. This discrepancy is most likely due to their much larger particle-to-fluid density ratio. For the oversampling fluid velocity bias term ($\overline{U_f|_p} - \overline{U_f}$), negative values that grow away from the bed are observed, which

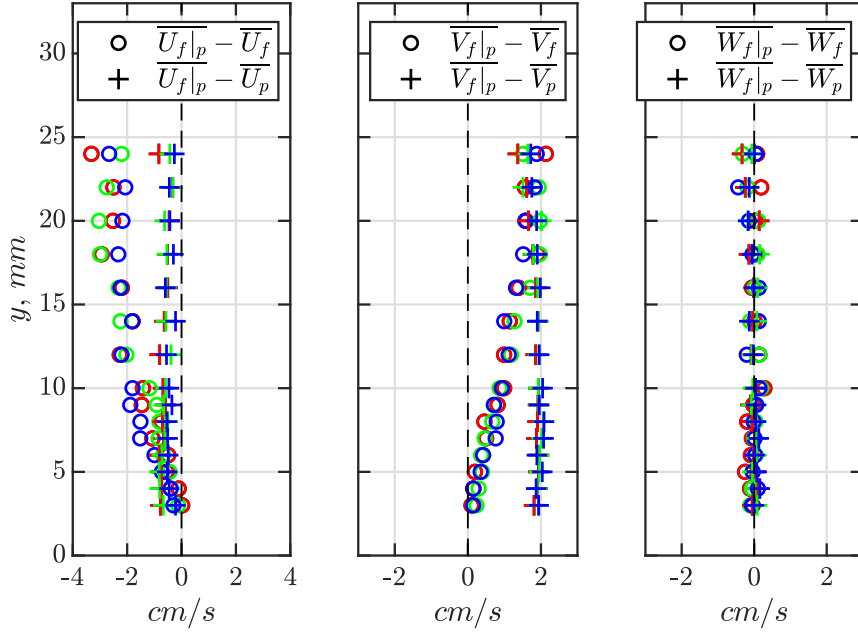


Figure 4.15: The particle-conditioned slip velocity profiles (+) and the oversampling of fluid regions faster/slower than the mean (\circ), decomposed in streamwise (left), normal-to-bed (middle) and spanwise (right) directions at the three reversal phases, 170° (red), 0° (green) and 10° (blue).

indicates that the particles favor low-speed (or more negative) regions and that this oversampling is stronger away from the bed. Qualitatively similar behavior were also reported in both works of Kiger and Pan [65] and Berk and Coletti [68]. In Figure 4.15, it is shown that for $y > 10 \text{ mm}$, a more or less constant value of $\overline{U_f|_p} - \overline{U_f}$ is observed, equivalent to approximately 30% of the bottom friction velocity ($u_{\tau,p}$, Table 4.2), which is also within the same order of magnitudes as reported by Kiger and Pan [65] and Berk and Coletti [68]. It should be noted that in the present work, the mean flow has already reversed the direction at certain elevations (see Figure 4.13), so the consistently negative values of $\overline{U_f|_p} - \overline{U_f}$ term, could also mean a preferential sampling of high-speed flow regions in the reversed direction, as is the case for $y > 10 \text{ mm}$ at phase 10° and $10 < y < 20 \text{ mm}$ at phase 0° .

In the normal-to-bed direction, as shown in the middle plot of Figure 4.15, the particle-conditioned slip velocity ($\overline{V_f|_p} - \overline{V_p}$) shows constant values throughout the measurement range, which is around 2 cm/s accounting for about 65% of the particle settling velocity (W_s). This means that each sediment particle statistically experiences an upward moving flow with a velocity of 2 cm/s , which provides drag forces and is responsible for the suspension of sediment particles. The fact that the measured particle-conditioned slip velocity is smaller than the still-fluid particle settling velocity is also observed in the work of Kiger and Pan [65]. Preferential sampling of fluid velocities at particle locations also exists with the normal-to-bed velocity component, demonstrated by the profiles of the term $\overline{V_f|_p} - \overline{V_f}$. It is shown that the sediment particles favor to locate in the upward moving regions in the flow, with stronger oversampling away from the bed. The variation of $\overline{U_f|_p} - \overline{U_f}$ and $\overline{V_f|_p} - \overline{V_f}$ with height seems to show a consistent pattern, by combining these two profiles, it can be inferred that for the particles away from the bed, they tend to appear in flow regions where ejection of slow moving fluid (“ejection events”) occurs and this preferential sampling decays near the bed. This agrees with findings by Kiger and Pan [65] and Berk and Coletti [68], in both of which quadrant analysis was conducted to confirm the ejection events. In the spanwise direction, the particles seem to be able to closely follow the ambient flow and don’t show a preferential residence in terms of the spanwise velocity.

Quadrant analysis was performed to provide further evidence on the oversampling of sediment particles at locations with ejection events ($u_f < 0$ and $v_f > 0$) in the flow, as shown in Figure 4.16 at phase 0° . Qualitatively similar behavior

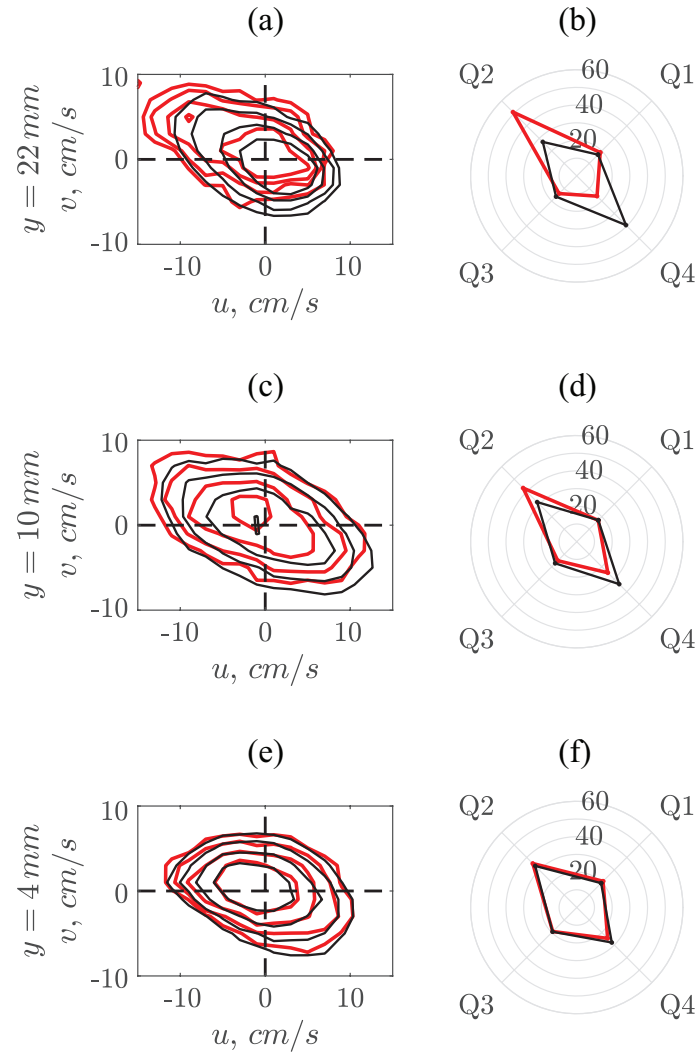


Figure 4.16: At phase 0° , joint probability density functions of streamwise and vertical velocity fluctuations for the fluid (black lines) and particle-conditioned fluid (red lines), at three different elevations, (a) $y = 22\text{ mm}$, (c) $y = 10\text{ mm}$ and (e) $y = 4\text{ mm}$, with contours at levels of 0.001, 0.002, 0.004 and 0.007. (b), (d) and (f) shows the percentage of unconditioned (black lines) and particle-conditioned (red lines) fluid events in each quadrant at the same three elevations.

can be observed at the other two phase angles. Figure 4.16 (a), (c) and (e) illustrate the joint probability density functions of the streamwise and normal-to-bed velocity fluctuations for particle-conditioned fluid (red lines), which is superimposed on the unconditioned fluid results (black lines) for comparison. The comparison is conducted at three different elevations from the static bed, corresponding to three distinct values of $\overline{U_f|_p} - \overline{U_f}$ and $\overline{V_f|_p} - \overline{V_f}$ observed in Figure 4.15. The inclined and elongated shape of these contour lines (especially for $y = 10\text{ mm}$ and $y = 22\text{ mm}$) indicates the prevalence of flow events contributing to the negative Reynolds shear stresses, as will be confirmed in Section 4.3.6 where second order statistics are investigated. It is also observed that as y increases, the contours of the particle-conditioned fluid velocity distribution demonstrates an increased shift towards the second quadrant (Q2, ejection events) direction away from the unconditioned one. At $y = 4\text{ mm}$, the contour lines almost overlap with each other indicating a very weak preferential sampling of particle residence near the bed; whereas further away from the bed ($y = 10\text{ mm}$ and $y = 22\text{ mm}$), the shifted contour lines highlights the tendency of sediment particles to over-sample events in the second quadrant Q2 ($u_f < 0$ and $v_f > 0$) and under-sample those in the fourth quadrant Q4 ($u_f > 0$ and $v_f < 0$, referred to as sweeps). Figure 4.16 (b), (d) and (f) computes the percentage of flow events belonging to each of the four quadrants as shown in (a), (c) and (e) respectively, for the particle-conditioned (red lines) and unconditioned fluid (black lines). This again shows an increased preferential sampling of ejection events (Q2) over sweeps (Q4) at larger distance from the bed. The particles don't seem to show a significantly biased sampling in the first and third quadrant at the three elevations

shown in the figure. Comparisons can be also made between the contours at the three elevations and there seems to be an increased inclined angle of the contours with increased distance from the bed, which is also observed in steady turbulent channel flows (Kiger and Pan [65]). For the contour lines at $y = 4\text{ mm}$ at phase 10° (not shown), an almost zero inclined angle is observed, i.e. the fluid velocity distribution is almost symmetric about the horizontal axis, which should result in a small Reynolds shear stress as will be consistently shown in Figure 4.19.

4.3.6 Second order statistics

The vertical profiles of the velocity fluctuation intensities for the sediment particles (dot symbols) and the carrier phase (solid lines) decomposed into x -, y - and z - directions are illustrated in Figure 4.17. The fluid velocity fluctuations show a maximum at around 10 mm above the bed, with decreasing magnitudes toward the bed and outer regions of the flow. The maximum fluctuations achieved in the streamwise direction are approximately 50% higher than the values obtained in the other two directions. For $y < 15\text{ mm}$, the evolution of the velocity fluctuations from phase 170° to 0° show a slowly decreasing trend in all directions. The sediment velocity fluctuations can roughly follow the trend observed for the corresponding fluid profiles. For $y > 15\text{ mm}$, the sediment velocity fluctuations seem to show consistently higher values than the corresponding fluid velocity fluctuations; and for $y < 15\text{ mm}$, no meaningful difference in velocity fluctuations between phases can be discerned. The higher particulate velocity fluctuations relative to the carrier

fluid in the outer region has also been observed in a smooth-wall open channel flow (Baker and Coletti [121]). It is worth noting that the achieved maximum velocity fluctuation during flow reversal approximately equals the empirical friction velocity computed during peak flow ($u_{\tau,p}$, Table 4.2), which indicates that the turbulent intensities encountered during flow reversal remains comparable to that achieved during peak flow. One possible cause of these peak turbulent fluctuation levels might be attributed to the adverse pressure gradient peaking during flow reversal, which induces additional instabilities in the boundary layer flow.

Figure 4.18 compares the fluid velocity fluctuation intensities for the unconditioned flow (solid lines) and those only sampled at particle locations (particle-conditioned, +). A consistent pattern is observed for all three velocity components at all phase angles: for $y > 15 \text{ mm}$, the particles favor the high velocity fluctuation regions; whereas for $y < 12 \text{ mm}$, the particles are over-sampled in slightly lower velocity fluctuation regions. The preferential sampling of sediment particles in flow regions with high turbulent fluctuations can partly explain the larger velocity fluctuations demonstrated by the sediment particles than by the fluid at $y > 15 \text{ mm}$, as pointed out in Figure 4.17.

The normal-to-bed profiles of the Reynolds shear stress for the sediment particles (dot symbols) and the carrier phase (solid lines) are illustrated in Figure 4.19. Significant correlations only exist between the streamwise and normal-to-bed velocity fluctuations. The near-zero correlation values shown by the other two Reynolds shear stress components, $\overline{v\overline{w}}$ and $\overline{u\overline{w}}$, are again an indication of flow homogeneity in the spanwise direction. The fluid Reynolds shear stress, $\overline{u_f v_f}$, achieves maxima at

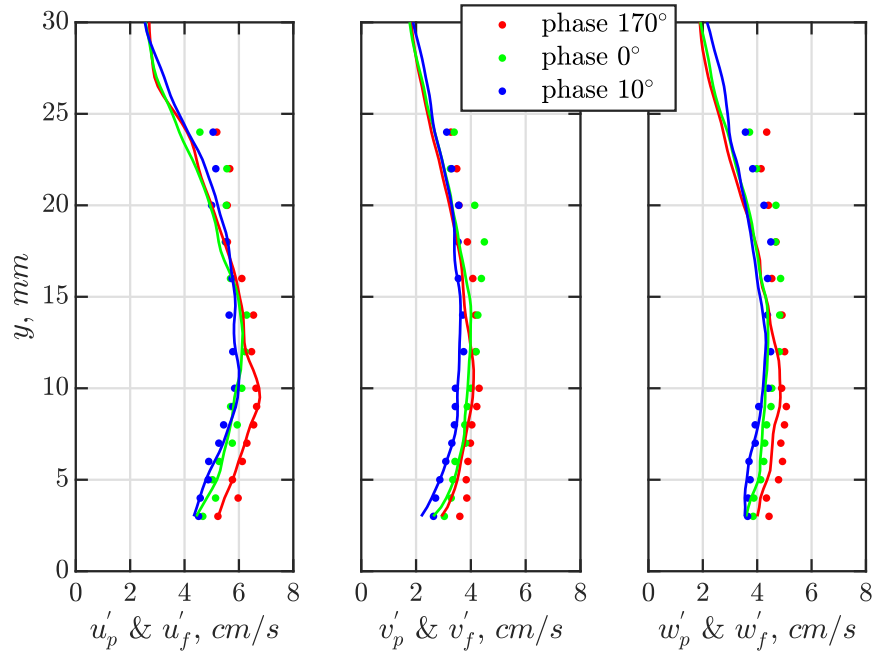


Figure 4.17: The normal-to-bed profiles of the root-mean-square of velocity fluctuations for the sediment particles (dot symbols) and the carrier phase (solid lines) near flow reversal, at phases 170° , 0° and 10° .

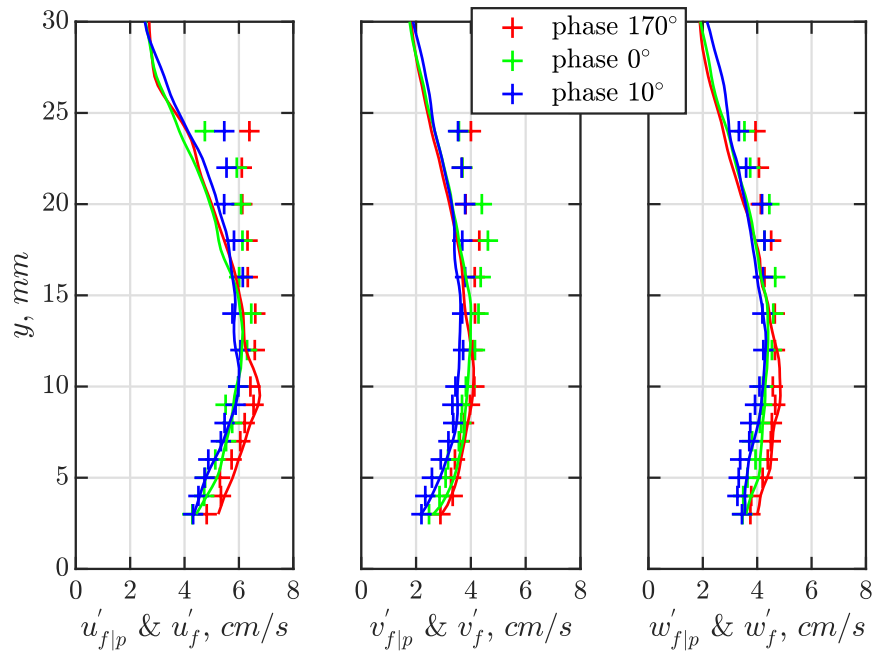


Figure 4.18: The normal-to-bed profiles of the root-mean-square of velocity fluctuations for particle-conditioned carrier phase (+) and unconditioned carrier phase (solid lines) near flow reversal, at phases 170° , 0° and 10° .

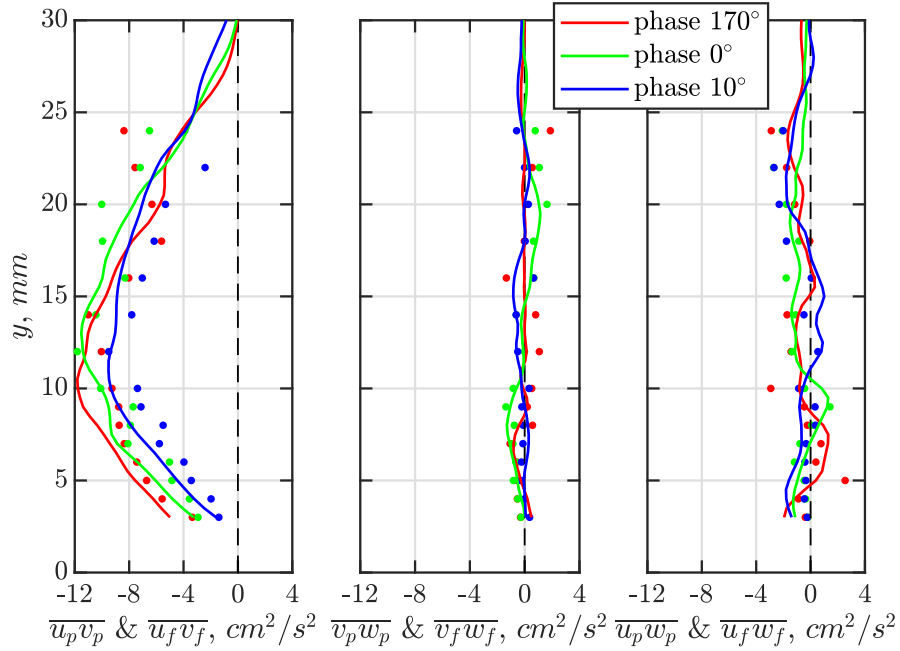


Figure 4.19: The Reynolds stress profiles of the sediment particles (dot symbols) and the carrier phase (solid lines) near flow reversal, at phases 170° , 0° and 10° .

$y = 10 \sim 13 \text{ mm}$ for the three phase angles and decreases as approaching to the bed or the outer region. As the flow evolves from phase 170° to 0° , a noticeable decrease in the Reynolds shear stress is observed for $y < 10 \text{ mm}$, indicating a decrease of turbulence production near the bed, which is consistent with the decreased turbulent kinetic energy observed in Figure 4.17. The Reynolds shear stress of the sediment phase, $\overline{u_p v_p}$, is comparable to that of the fluid phase, which is also observed by Kiger and Pan [65] in a steady channel flow.

The particle-fluid velocity cross-correlation coefficients of the streamwise ($R_{u,fp}$), normal-to-bed ($R_{v,fp}$) and spanwise ($R_{w,fp}$) components, computed at phase 0° , are demonstrated in Figure 4.20. The other two phase angles show similar coefficient values and are thus omitted here. The coefficient in the streamwise direction is defined as $R_{u,fp} = \overline{u_{f|p} u_p} / u'_{f|p} u'_p$, with the other directions defined in the same way

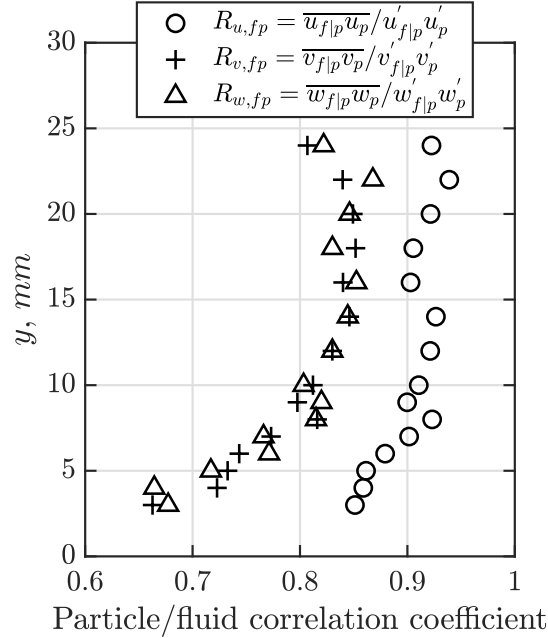


Figure 4.20: Particle-fluid cross-correlation coefficients (normalized by the the RMS velocity fluctuations of the particles and fluid) of the streamwise (\circ), normal-to-bed ($+$) and spanwise (Δ) velocity components, at phase 0° .

as shown in the legend of Figure 4.20. The coefficient examines the correlation of the velocity signals exhibited by the particles and their instantaneous surrounding fluid. A large coefficient value indicates that sediment particles can quickly adapt their motions to the local flow and vice versa. Apparently the coefficient should strongly depend upon the local particle Stokes number. A similar trend is observed for all velocity components of R_{fp} in Figure 4.20, with nearly constant and relatively high velocity correlations for $y > 10 \text{ mm}$ and monotonically decreased correlations toward the bed for $y < 10 \text{ mm}$. The decrease in correlation near the bed indicates that the particles lose their abilities to closely follow the fluid motions, which can be explained by the decreased fluid time scales and a corresponding increase of particle Stokes number. The correlation coefficients of the normal-to-bed ($R_{v,fp}$) and spanwise ($R_{w,fp}$) components have similar values and both are smaller than the

streamwise ($R_{u,fp}$) values, which implies the existence of higher frequency velocity fluctuations in the normal-to-bed and spanwise directions. Qualitatively similar cross-correlation coefficient profiles have also been observed in a steady channel flow (Kiger and Pan [65]).

Chapter 5: Summary

In this thesis, a whole field, phase-locked time-resolved, particle-resolved and concurrent measurement of both the fluid and the sediment phase within the dilute regime ($C \leq 1\%$) in a sinusoidal oscillatory sheet flow ($U_{o,p} = 1 \text{ m/s}$, and $T = 5 \text{ s}$) has been conducted. The measurement was realized by a novel multi-camera PIV and PTV imaging technique, which is recently developed and specifically suitable for multiphase flow imaging. In this measurement, the instantaneous 3D positions of individual sediment particles located close to the light sheet center ($\sim \pm 0.5 \text{ mm}$) were reconstructed and their temporal trajectories were computed over successive frames. For the carrier phase measurement, stereoscopic PIV (SPIV) technique was simultaneously implemented, in which 3D fluid velocity vectors were computed on the 2D plane coinciding with the resolved sediment particles. The resultant spatial resolution (interrogation window size) for the SPIV measurement is about six times of the particle diameter or twice of average particle spacing under the highest concentration of our interest ($C = 1\%$ corresponding to an average particle spacing of $\lambda_p = 3.7 d$). To the author's best knowledge, two-phase measurements at such detailed level under sheet flow conditions have never been reported before by other researchers. The direct contribution of the current study is at least twofold,

which will be discussed in the following.

I. Advancement of measurement technique. In sheet flow measurements, the existence of the sediment bed, the requirement of making measurements away from the side walls and the measurement goals set by this thesis (whole field, particle-resolved and concurrent measurements of both phases for $C \leq 1\%$) combined define an extremely challenging measurement problem. When reconstructing the sediment particle locations, the difficulty mainly originates from the obscuration among particles towards increased concentration. In order to alleviate the obscuration problem, a multi-camera single-plane (MCSP) method was developed. The essence of this technique is 1) to utilize a thin illuminating light sheet to constrain the measurement thickness and alleviate the obscuration between particles, and 2) to make the full use of the particles' image characteristics to reduce the ambiguities when creating stereoscopic correspondences. Through the use of a static sediment/gel suspension test cell, it was demonstrated that up to optical densities of close to $\mathcal{O}(1)$, the MCSP method is capable of reliably reconstructing particle positions and providing concentration measurements with an accuracy of 2% up to a volume fraction of $C \approx 0.8\%$. In terms of the concentration measurement range, the MCSP method exceeds the previous single camera method (Knowles and Kiger [74]) by one order of magnitude. The work has been accepted for publication in *Experiments in Fluids*.

For the carrier phase measurement, the challenge originates from the separation of signals from each phase, which is complicated by the huge disparities in the image intensities of the sediment particles and the tracer particles (due to their different sizes) and the much higher target sediment concentration ($C = 1\%$). In

order to achieve balanced signals for both phases, the Apertured Filter method was developed, in which fluorescent tracer particles in conjunction with conventional band-pass optical filter with a round hole (with a diameter much smaller than the camera aperture size) drilled at the center were used. The apertured filter method was proved to be able to produce adequate image quality of both phases allowing for a reliable extraction of each phase independently. The PIV cross-talk errors were evaluated and less than 0.3 pixels of mean absolute errors were achieved under the highest concentration of our interest ($C = 1\%$). This work has been submitted to the 20th International Symposium on Applications of Laser and Imaging Techniques conference for abstract review and is intended to be published in Experiments in Fluids in the near future.

The newly developed measurement technique can be generalized and utilized in a much broader range of multiphase flow applications, such as droplets in air, bubbles in water etc., if particle-resolved and concurrent measurements are desired. In volumetric velocimetry techniques, the biggest motivation for researchers to keep adding additional cameras for particle 3D reconstruction and tracking is to reduce the ambiguities in establishing stereoscopic correspondences (matching the particles in different cameras that belong to the same physical particle in 3D space). The MCSP method offers a new perspective to reduce the matching ambiguities without adding more cameras. In this method, before particle matching, particle image characteristics are examined to screen out the candidate particles that are located relatively far from the light sheet center. The reduced number of candidate particles will alleviate the problem of matching ambiguity. The strongest limitation of the

MCSP method is that it requires the particle image characteristics to correlate with its spatial location, which is often hard to be satisfied, such as tracer particles under volumetric illuminations. In multiphase flow PIV measurement, balanced image intensities of the discrete phase and the carrier phase (tracer particles) are typically difficult to be achieved in a single camera, due to their disparities in sizes. In past studies, two-phase measurements were either conducted under very dilute particle concentrations ($C < 10^{-4}$) or realized by assigning cameras (with different camera settings) exclusively for the measurement of each phase. The latter option is not practical for volumetric imaging due to the increased number of cameras required. The apertured filter method offers a solution for independent control of the image intensities of the discrete phase and the carrier phase in each single camera, which optimizes the image quality of both phases and is able to achieve comparable measurement capability and accuracy that could only be previously achieved by assigning cameras dedicated to the measurement of each phase separately.

II. Particle-turbulence interaction. This thesis aims at extending the current knowledge base on particle-turbulence interaction occurred within the suspension layer under oscillatory sheet flow conditions. Data analysis was focused upon three phase angles (170° , 0° and 10°), during which the external flow is reversing the direction and experiencing a maximum adverse pressure gradient. Some important findings presented in this thesis are summarized below.

1) In the phase-averaged concentration profiles, power law relations are observed in both the upper dilute regime ($y > 11\text{ mm}$) and the lower dilute regime ($2 < y < 4\text{ mm}$) with decreased exponent magnitude approaching the bed. A re-

versed change in the exponent over the three phase angles is found in these two regions. This is indicative of different sediment particle suspension mechanisms occurred in these two regions.

2) In the phase-averaged streamwise velocity profiles, the velocity difference between the sediment and the fluid is within 8% of the maximum velocity for all three phase angles; for $y < 18\text{ mm}$, the sediment vertical velocity profile show a distinct downward velocity that increases approaching the bed for all three phase angles, which indicates a net settling of sediment particles towards the bed during flow reversal.

3) Significant sediment flux in the streamwise direction is observed near the bed during flow reversal due to the phase lead of the boundary layer flow relative to the free stream velocity. Abrupt changes in the streamwise sediment flux profiles is observed from phase 170° to 0° ; on the contrary, little change is detected from phase 0° to 10° . For the vertical sediment flux, a decreased settling flux is observed from as phases evolve from 170° to 10° , which is mainly due to the decrease in the concentration.

4) The particle conditioned slip velocity shows negligible values in the streamwise direction ($\overline{U_f|_p} - \overline{U_p} \approx 0$) and an almost constant value throughout the measurement height in the normal-to-bed direction ($\overline{V_f|_p} - \overline{V_p} \approx 2\text{ cm/s} = 65\% \times W_s$).

5) In second order statistics, the maximum turbulent fluctuation in the streamwise direction is 50% higher than that in the other two directions. For $y > 15\text{ mm}$, the turbulent kinetic energy of the sediment phase is slightly higher that of the fluid. For $y < 10\text{ mm}$, a decrease in the turbulent kinetic energy and Reynolds shear stress

is observed as phases evolve from 170° to 10° .

6) Strong preferential sampling of sediment particles in flow regions with ejection events (Q2) and high turbulent fluctuations is demonstrated for $y > 11 \text{ mm}$, while the over-sampling diminishes towards the bed.

7) The particle velocity and their ambient fluid velocity show a strong correlation ($R_{u,fp} \approx 0.92$, $R_{v,fp} \approx R_{w,fp} \approx 0.85$) for $y > 11 \text{ mm}$ and the correlation becomes weaker as approaching the bed.

The complete data set for the full cycle measurement will be processed and analyzed in the future for a comprehensive study. The work is intended to publish in Physical Review Fluids or Journal of Fluid Mechanics.

Bibliography

- [1] Daniel Schanz, Sebastian Gesemann, and Andreas Schröder. Shake-the-box: Lagrangian particle tracking at high particle image densities. *Experiments in Fluids*, 57(5):70, Apr 2016. ISSN 1432-1114. doi: 10.1007/s00348-016-2157-1.
- [2] Eckart Meiburg and Ben Kneller. Turbidity currents and their deposits. *Annual Review of Fluid Mechanics*, 42(1):135–156, 2010. doi: 10.1146/annurev-fluid-121108-145618. URL <https://doi.org/10.1146/annurev-fluid-121108-145618>.
- [3] Laurent Amoudry. *Two-phase modeling of granular sediment for sheet flows and scour*. PhD thesis, Cornell University, 2007.
- [4] Zhen Cheng, Tian-Jian Hsu, and Joseph Calantoni. Sedfoam: A multi-dimensional eulerian two-phase model for sediment transport and its application to momentary bed failure. *Coastal Engineering*, 119:32 – 50, 2017. ISSN 0378-3839. doi: <https://doi.org/10.1016/j.coastaleng.2016.08.007>. URL <http://www.sciencedirect.com/science/article/pii/S0378383916301958>.
- [5] Eugen Meyer-Peter and R Müller. Formulas for bed-load transport. In *IAHSR 2nd meeting, Stockholm, appendix 2*. IAHR, 1948.
- [6] Kenneth C Wilson. Bed-load transport at high shear stress. *Journal of the hydraulics division*, 92(6):49–59, 1966.
- [7] Jan S Ribberink. Bed-load transport for steady flows and unsteady oscillatory flows. *Coastal Engineering*, 34(1-2):59–82, 1998.
- [8] S. Balachandar and John K. Eaton. Turbulent dispersed multiphase flow. *Annual Review of Fluid Mechanics*, 42(1):111–133, 2010. doi: 10.1146/annurev.fluid.010908.165243. URL <https://doi.org/10.1146/annurev.fluid.010908.165243>.
- [9] Jim Ferry and S. Balachandar. A fast eulerian method for disperse two-phase flow. *International Journal of Multiphase Flow*, 27(7):1199 – 1226, 2001. ISSN 0301-9322. doi: [https://doi.org/10.1016/S0301-9322\(00\)00069-0](https://doi.org/10.1016/S0301-9322(00)00069-0). URL <http://www.sciencedirect.com/science/article/pii/S0301932200000690>.

- [10] Zhen Cheng, Xiao Yu, Tian-Jian Hsu, Celalettin E Ozdemir, and S Balachandar. On the transport modes of fine sediment in the wave boundary layer due to resuspension/deposition: A turbulence-resolving numerical investigation. *Journal of Geophysical Research: Oceans*, 120(3):1918–1936, 2015.
- [11] Zhen Cheng, Xiao Yu, Tian-Jian Hsu, and S Balachandar. A numerical investigation of fine sediment resuspension in the wave boundary layer—uncertainties in particle inertia and hindered settling. *Computers & geosciences*, 83:176–192, 2015.
- [12] Ralph Alger Bagnold. *An approach to the sediment transport problem from general physics*. US government printing office, 1966.
- [13] Leo C Van Rijn. Sediment transport, part i: bed load transport. *Journal of hydraulic engineering*, 110(10):1431–1456, 1984.
- [14] G.R. Lesser, J.A. Roelvink, J.A.T.M. van Kester, and G.S. Stelling. Development and validation of a three-dimensional morphological model. *Coastal Engineering*, 51(8):883 – 915, 2004. ISSN 0378-3839. doi: <https://doi.org/10.1016/j.coastaleng.2004.07.014>. URL <http://www.sciencedirect.com/science/article/pii/S0378383904000870>. Coastal Morphodynamic Modeling.
- [15] Kjell Hagatun and Karl J. Eidsvik. Oscillating turbulent boundary layer with suspended sediments. *Journal of Geophysical Research: Oceans*, 91(C11):13045–13055, 1986. doi: 10.1029/JC091iC11p13045. URL <https://agupubs.onlinelibrary.wiley.com/doi/abs/10.1029/JC091iC11p13045>.
- [16] Yong Zhang, Donald J.P. Swift, Shejun Fan, Alan Wm. Niedoroda, and Christopher W. Reed. Two-dimensional numerical modeling of storm deposition on the northern california shelf. *Marine Geology*, 154(1):155 – 167, 1999. ISSN 0025-3227. doi: [https://doi.org/10.1016/S0025-3227\(98\)00110-8](https://doi.org/10.1016/S0025-3227(98)00110-8). URL <http://www.sciencedirect.com/science/article/pii/S0025322798001108>.
- [17] Courtney K Harris and Patricia L Wiberg. A two-dimensional, time-dependent model of suspended sediment transport and bed reworking for continental shelves. *Computers & Geosciences*, 27(6):675–690, 2001.
- [18] Wim-Paul Breugem. A second-order accurate immersed boundary method for fully resolved simulations of particle-laden flows. *Journal of Computational Physics*, 231(13):4469 – 4498, 2012. ISSN 0021-9991. doi: <https://doi.org/10.1016/j.jcp.2012.02.026>. URL <http://www.sciencedirect.com/science/article/pii/S0021999112001374>.
- [19] Markus Uhlmann. An immersed boundary method with direct forcing for the simulation of particulate flows. *Journal of Computational Physics*, 209(2):448 – 476, 2005. ISSN 0021-9991. doi: <https://doi.org/10.1016/j.jcp>.

2005.03.017. URL <http://www.sciencedirect.com/science/article/pii/S0021999105001385>.

- [20] Francesco Picano, Wim-Paul Breugem, and Luca Brandt. Turbulent channel flow of dense suspensions of neutrally buoyant spheres. *Journal of Fluid Mechanics*, 764:463–487, 2015. doi: 10.1017/jfm.2014.704.
- [21] J.C. Brändle de Motta, P. Costa, J.J. Derksen, C. Peng, L.-P. Wang, W.-P. Breugem, J.L. Estivalezes, S. Vincent, E. Climent, P. Fede, P. Barbaresco, and N. Renon. Assessment of numerical methods for fully resolved simulations of particle-laden turbulent flows. *Computers & Fluids*, 179:1 – 14, 2019. ISSN 0045-7930. doi: <https://doi.org/10.1016/j.compfluid.2018.10.016>. URL <http://www.sciencedirect.com/science/article/pii/S0045793018307709>.
- [22] Cheng Peng, Orlando M. Ayala, and Lian-Ping Wang. A direct numerical investigation of two-way interactions in a particle-laden turbulent channel flow. *Journal of Fluid Mechanics*, 875:1096–1144, 2019. doi: 10.1017/jfm.2019.509.
- [23] Zhen Cheng, Julien Chauchat, Tian-Jian Hsu, and Joseph Calantoni. Eddy interaction model for turbulent suspension in reynolds-averaged euler–lagrange simulations of steady sheet flow. *Advances in Water Resources*, 111:435 – 451, 2018. ISSN 0309-1708. doi: <https://doi.org/10.1016/j.advwatres.2017.11.019>. URL <http://www.sciencedirect.com/science/article/pii/S0309170817303858>.
- [24] ZY Zhou, SB Kuang, KW Chu, and AB2726154 Yu. Discrete particle simulation of particle–fluid flow: model formulations and their applicability. *Journal of Fluid Mechanics*, 661:482–510, 2010.
- [25] T Bo Anderson and Roy Jackson. Fluid mechanical description of fluidized beds. equations of motion. *Industrial & Engineering Chemistry Fundamentals*, 6(4):527–539, 1967.
- [26] Justin R. Finn, Ming Li, and Sourabh V. Apte. Particle based modelling and simulation of natural sand dynamics in the wave bottom boundary layer. *Journal of Fluid Mechanics*, 796:340–385, 2016. doi: 10.1017/jfm.2016.246.
- [27] Martin R Maxey and James J Riley. Equation of motion for a small rigid sphere in a nonuniform flow. *The Physics of Fluids*, 26(4):883–889, 1983.
- [28] Luca Brandt and Filippo Coletti. Particle-laden turbulence: Progress and perspectives. *Annual Review of Fluid Mechanics*, 54, 2021.
- [29] Niels G Deen, Martin van Sint Annaland, and JAM Kuipers. Multi-scale modeling of dispersed gas–liquid two-phase flow. *Chemical engineering science*, 59(8-9):1853–1861, 2004.

- [30] E Delnoij, FA Lammers, JAM Kuipers, and Willibrordus Petrus Maria van Swaaij. Dynamic simulation of dispersed gas-liquid two-phase flow using a discrete bubble model. *Chemical engineering science*, 52(9):1429–1458, 1997.
- [31] Jidong Zhao and Tong Shan. Coupled cfd–dem simulation of fluid–particle interaction in geomechanics. *Powder technology*, 239:248–258, 2013.
- [32] Mark W Schmeeckle. Numerical simulation of turbulence and sediment transport of medium sand. *Journal of Geophysical Research: Earth Surface*, 119(6):1240–1262, 2014.
- [33] Yashar Rafati, Tian-Jian Hsu, Zhen Cheng, Xiao Yu, and Joseph Calantoni. Armoring and exposure effects on the wave-driven sediment transport. *Continental Shelf Research*, 211:104291, 2020.
- [34] Huabin Shi and Xiping Yu. An effective euler–lagrange model for suspended sediment transport by open channel flows. *International Journal of Sediment Research*, 30(4):361–370, 2015.
- [35] Johannes GM Kuerten. Point-particle dns and les of particle-laden turbulent flow—a state-of-the-art review. *Flow, turbulence and combustion*, 97(3):689–713, 2016.
- [36] L. Amoudry, T.-J. Hsu, and P. L.-F. Liu. Two-phase model for sand transport in sheet flow regime. *Journal of Geophysical Research: Oceans*, 113(C3), 2008. doi: 10.1029/2007JC004179. URL <https://agupubs.onlinelibrary.wiley.com/doi/abs/10.1029/2007JC004179>.
- [37] Zhen Cheng, Tian-Jian Hsu, and Julien Chauchat. An eulerian two-phase model for steady sheet flow using large-eddy simulation methodology. *Advances in Water Resources*, 111:205 – 223, 2018. ISSN 0309-1708. doi: <https://doi.org/10.1016/j.advwatres.2017.11.016>. URL <http://www.sciencedirect.com/science/article/pii/S0309170817308564>.
- [38] D A Drew. Mathematical modeling of two-phase flow. *Annual Review of Fluid Mechanics*, 15(1):261–291, 1983. doi: 10.1146/annurev.fl.15.010183.001401. URL <https://doi.org/10.1146/annurev.fl.15.010183.001401>.
- [39] Donald A. Drew and Richard T. Lahey. Application of general constitutive principles to the derivation of multidimensional two-phase flow equations. *International Journal of Multiphase Flow*, 5(4):243 – 264, 1979. ISSN 0301-9322. doi: [https://doi.org/10.1016/0301-9322\(79\)90024-7](https://doi.org/10.1016/0301-9322(79)90024-7). URL <http://www.sciencedirect.com/science/article/pii/0301932279900247>.
- [40] DZ Zhang and A Prosperetti. Momentum and energy equations for disperse two-phase flows and their closure for dilute suspensions. *International journal of multiphase flow*, 23(3):425–453, 1997.

- [41] R Jackson. Locally averaged equations of motion for a mixture of identical spherical particles and a newtonian fluid. *Chemical Engineering Science*, 52 (15):2457–2469, 1997.
- [42] Christopher E. Brennen. *Fundamentals of Multiphase Flow*. Cambridge University Press, 2005. doi: 10.1017/CBO9780511807169.
- [43] Jose M Gonzalez-Ondina, Luigi Fraccarollo, and Philip L-F Liu. Two-level, two-phase model for intense, turbulent sediment transport. *Journal of Fluid Mechanics*, 839:198–238, 2018.
- [44] Tian-Jian Hsu, James T Jenkins, and Philip L-F Liu. On two-phase sediment transport: Dilute flow. *Journal of Geophysical Research: Oceans*, 108(C3), 2003.
- [45] Tian-Jian Hsu, James T Jenkins, and Philip L-F Liu. On two-phase sediment transport: sheet flow of massive particles. *Proceedings of the Royal Society of London. Series A: Mathematical, Physical and Engineering Sciences*, 460 (2048):2223–2250, 2004.
- [46] L. Amoudry, T.-J. Hsu, and P. L.-F. Liu. Schmidt number and near-bed boundary condition effects on a two-phase dilute sediment transport model. *Journal of Geophysical Research: Oceans*, 110(C9), 2005. doi: 10.1029/2004JC002798. URL <https://agupubs.onlinelibrary.wiley.com/doi/abs/10.1029/2004JC002798>.
- [47] Laurent O. Amoudry. Extension of $k\text{-}\omega$ turbulence closure to two-phase sediment transport modelling: Application to oscillatory sheet flows. *Advances in Water Resources*, 72:110 – 121, 2014. ISSN 0309-1708. doi: <https://doi.org/10.1016/j.advwatres.2014.07.006>. URL <http://www.sciencedirect.com/science/article/pii/S0309170814001407>. THESIS (Two-phase modelling for Sediment dynamics).
- [48] Xiao Yu, Tian-Jian Hsu, James T. Jenkins, and Philip L.-F. Liu. Predictions of vertical sediment flux in oscillatory flows using a two-phase, sheet-flow model. *Advances in Water Resources*, 48:2 – 17, 2012. ISSN 0309-1708. doi: <https://doi.org/10.1016/j.advwatres.2012.05.012>. URL <http://www.sciencedirect.com/science/article/pii/S0309170812001492>. Two-Phase Modeling of Sediment Dynamics.
- [49] L.O. Amoudry and P.L.-F. Liu. Two-dimensional, two-phase granular sediment transport model with applications to scouring downstream of an apron. *Coastal Engineering*, 56(7):693 – 702, 2009. ISSN 0378-3839. doi: <https://doi.org/10.1016/j.coastaleng.2009.01.006>. URL <http://www.sciencedirect.com/science/article/pii/S037838390900012X>.
- [50] Jianmin Ding and Dimitri Gidaspow. A bubbling fluidization model using kinetic theory of granular flow. *AIChE journal*, 36(4):523–538, 1990.

- [51] JF Richardson and WN Zaki. The sedimentation of a suspension of uniform spheres under conditions of viscous flow. *Chemical Engineering Science*, 3(2): 65–73, 1954.
- [52] Thibaud Revil-Baudard, Julien Chauchat, David Hurther, and Pierre-Alain Barraud. Investigation of sheet-flow processes based on novel acoustic high-resolution velocity and concentration measurements. *Journal of Fluid Mechanics*, 767:1–30, 2015. doi: 10.1017/jfm.2015.23.
- [53] Jan S. Ribberink and Abdullah A. Al-Salem. Sheet flow and suspension of sand in oscillatory boundary layers. *Coastal Engineering*, 25(3):205 – 225, 1995. ISSN 0378-3839. doi: [https://doi.org/10.1016/0378-3839\(95\)00003-T](https://doi.org/10.1016/0378-3839(95)00003-T). URL <http://www.sciencedirect.com/science/article/pii/S037838399500003T>.
- [54] Tom O’Donoghue and Scott Wright. Concentrations in oscillatory sheet flow for well sorted and graded sands. *Coastal Engineering*, 50(3):117 – 138, 2004. ISSN 0378-3839. doi: <https://doi.org/10.1016/j.coastaleng.2003.09.004>. URL <http://www.sciencedirect.com/science/article/pii/S0378383903001017>.
- [55] Tom O’Donoghue and Scott Wright. Flow tunnel measurements of velocities and sand flux in oscillatory sheet flow for well-sorted and graded sands. *Coastal Engineering*, 51(11):1163 – 1184, 2004. ISSN 0378-3839. doi: <https://doi.org/10.1016/j.coastaleng.2004.08.001>. URL <http://www.sciencedirect.com/science/article/pii/S0378383904001139>.
- [56] Xin Chen, Yong Li, Xiaojing Niu, Daoyi Chen, and Xiping Yu. A two-phase approach to wave-induced sediment transport under sheet flow conditions. *Coastal Engineering*, 58(11):1072 – 1088, 2011. ISSN 0378-3839. doi: <https://doi.org/10.1016/j.coastaleng.2011.06.003>. URL <http://www.sciencedirect.com/science/article/pii/S0378383911001001>.
- [57] Ming Li, Shunqi Pan, and Brian A. O’Connor. A two-phase numerical model for sediment transport prediction under oscillatory sheet flows. *Coastal Engineering*, 55(12):1159 – 1173, 2008. ISSN 0378-3839. doi: <https://doi.org/10.1016/j.coastaleng.2008.05.003>. URL <http://www.sciencedirect.com/science/article/pii/S0378383908001002>.
- [58] Jan J Bosman, Elsbeth TJM van der Velden, and Cornelis H Hulsbergen. Sediment concentration measurement by transverse suction. *Coastal Engineering*, 11(4):353–370, 1987.
- [59] DE Stock, JT Jurewicz, CT Crowe, and JE Eschbach. Measurement of both gas and particle velocity in turbulent two-phase flow. 1975.

- [60] M Muste, VC Patel, and RN Parthasarathy. Discriminator laser doppler velocimetry for measurement of liquid and particle velocities in sediment-laden flows. *Experiments in fluids*, 22(1):45–56, 1996.
- [61] Hervé Capart and Luigi Fraccarollo. Transport layer structure in intense bed-load. *Geophysical Research Letters*, 38(20), 2011. doi: 10.1029/2011GL049408. URL <https://agupubs.onlinelibrary.wiley.com/doi/abs/10.1029/2011GL049408>.
- [62] Benoit Spinewine, Hervé Capart, Luigi Fraccarollo, and Michele Larcher. Laser stripe measurements of near-wall solid fraction in channel flows of liquid-granular mixtures. *Experiments in fluids*, 50(6):1507–1525, 2011.
- [63] Yi Hui Tee, Diogo C Barros, and Ellen K Longmire. Motion of finite-size spheres released in a turbulent boundary layer. *International Journal of Multiphase Flow*, 133:103462, 2020.
- [64] M Muste, K Yu, I Fujita, and R Ettema. Two-phase versus mixed-flow perspective on suspended sediment transport in turbulent channel flows. *Water resources research*, 41(10), 2005.
- [65] KT Kiger and C Pan. Suspension and turbulence modification effects of solid particulates on a horizontal turbulent channel flow. *Journal of Turbulence*, 3(1):019, 2002.
- [66] Tomohiko Tanaka and John K Eaton. Sub-kolmogorov resolution partial image velocimetry measurements of particle-laden forced turbulence. *Journal of Fluid Mechanics*, 643:177–206, 2010.
- [67] Alec J Petersen, Lucia Baker, and Filippo Coletti. Experimental study of inertial particles clustering and settling in homogeneous turbulence. *Journal of Fluid Mechanics*, 864:925–970, 2019.
- [68] Tim Berk and Filippo Coletti. Transport of inertial particles in high-reynolds-number turbulent boundary layers. *Journal of Fluid Mechanics*, 903, 2020.
- [69] S. Salon, V. Armenio, and A. Crise. A numerical investigation of the stokes boundary layer in the turbulent regime. *Journal of Fluid Mechanics*, 570: 253–296, 2007. doi: 10.1017/S0022112006003053.
- [70] Philip Leland Knowles. *Sediment suspension events from ripple beds in oscillatory flow: Experiments*. PhD thesis, University of Maryland, College Park, 2009.
- [71] H. G. Maas, A. Gruen, and D. Papantoniou. Particle tracking velocimetry in three-dimensional flows. *Experiments in Fluids*, 15(2):133–146, Jul 1993. ISSN 1432-1114. doi: 10.1007/BF00190953.

- [72] D. A. Khalitov and E. K. Longmire. Simultaneous two-phase piv by two-parameter phase discrimination. *Experiments in Fluids*, 32(2):252–268, Feb 2002. ISSN 1432-1114. doi: 10.1007/s003480100356.
- [73] B. Spinewine, H. Capart, M. Larcher, and Y. Zech. Three-dimensional voronoi imaging methods for the measurement of near-wall particulate flows. *Experiments in Fluids*, 34(2):227, Feb 2003. ISSN 1432-1114. doi: 10.1007/s00348-002-0550-4.
- [74] Philip L. Knowles and Ken T. Kiger. Quantification of dispersed phase concentration using light sheet imaging methods. *Experiments in Fluids*, 52(3):697–708, Mar 2012. ISSN 1432-1114. doi: 10.1007/s00348-011-1100-8.
- [75] R. J. Adrian. Twenty years of particle image velocimetry. *Experiments in Fluids*, 39(2):159–169, Aug 2005. ISSN 1432-1114. doi: 10.1007/s00348-005-0991-7.
- [76] Bernhard Wieneke. Iterative reconstruction of volumetric particle distribution. *Measurement Science and Technology*, 24(2):024008, 2013.
- [77] Daniel Schanz, Sebastian Gesemann, Andreas Schröder, Bernhard Wieneke, and Matteo Novara. Non-uniform optical transfer functions in particle imaging: calibration and application to tomographic reconstruction. *Measurement Science and Technology*, 24(2):024009, 2013.
- [78] A V Mikheev and V M Zubtsov. Enhanced particle-tracking velocimetry (eptv) with a combined two-component pair-matching algorithm. *Measurement Science and Technology*, 19(8):085401, 2008.
- [79] Nicholas D Cardwell, Pavlos P Vlachos, and Karen A Thole. A multi-parametric particle-pairing algorithm for particle tracking in single and multiphase flows. *Measurement Science and Technology*, 22(10):105406, 2011.
- [80] Koichi Nishino, Nobuhide Kasagi, and Masaru Hirata. Three-dimensional particle tracking velocimetry based on automated digital image processing. *Journal of fluids engineering*, 111(4):384–391, 1989.
- [81] N. A. Malik, Th. Dracos, and D. A. Papantoniou. Particle tracking velocimetry in three-dimensional flows. *Experiments in Fluids*, 15(4):279–294, Sep 1993. ISSN 1432-1114. doi: 10.1007/BF00223406.
- [82] Nicholas T. Ouellette, Haitao Xu, and Eberhard Bodenschatz. A quantitative study of three-dimensional lagrangian particle tracking algorithms. *Experiments in Fluids*, 40(2):301–313, Feb 2006. ISSN 1432-1114. doi: 10.1007/s00348-005-0068-7.
- [83] Christian Cierpka, Benjamin Lütke, and Christian J. Kähler. Higher order multi-frame particle tracking velocimetry. *Experiments in Fluids*, 54(5):1533, May 2013. ISSN 1432-1114. doi: 10.1007/s00348-013-1533-3.

- [84] K. Okamoto, Y. A. Hassan, and W. D. Schmidl. New tracking algorithm for particle image velocimetry. *Experiments in Fluids*, 19(5):342–347, Sep 1995. ISSN 1432-1114. doi: 10.1007/BF00203419.
- [85] Kazuo Ohmi and Hang-Yu Li. Particle-tracking velocimetry with new algorithms. *Measurement Science and Technology*, 11(6):603, 2000.
- [86] M. Ishikawa, Y. Murai, A. Wada, M. Iguchi, K. Okamoto, and F. Yamamoto. A novel algorithm for particle tracking velocimetry using the velocity gradient tensor. *Experiments in Fluids*, 29(6):519–531, Dec 2000. ISSN 1432-1114. doi: 10.1007/s003480000120.
- [87] Yang Zhang, Yuan Wang, and Pan Jia. Improving the delaunay tessellation particle tracking algorithm in the three-dimensional field. *Measurement*, 49: 1 – 14, 2014. ISSN 0263-2241. doi: <https://doi.org/10.1016/j.measurement.2013.10.039>.
- [88] Yutong Cui, Yang Zhang, Pan Jia, Yuan Wang, Jingcong Huang, Junlei Cui, and Wing T. Lai. Three-dimensional particle tracking velocimetry algorithm based on tetrahedron vote. *Experiments in Fluids*, 59(2):31, Jan 2018. ISSN 1432-1114. doi: 10.1007/s00348-017-2485-9.
- [89] Tobias Böhm, Philippe Frey, Christophe Ducottet, Christophe Ancey, Magali Jodeau, and Jean-Luc Reboud. Two-dimensional motion of a set of particles in a free surface flow with image processing. *Experiments in Fluids*, 41(1): 1–11, Jul 2006. ISSN 1432-1114. doi: 10.1007/s00348-006-0134-9.
- [90] Virginie Hergault, Philippe Frey, François Métivier, Cécile Barat, Christophe Ducottet, Tobias Böhm, and Christophe Ancey. Image processing for the study of bedload transport of two-size spherical particles in a supercritical flow. *Experiments in Fluids*, 49(5):1095–1107, Nov 2010. ISSN 1432-1114. doi: 10.1007/s00348-010-0856-6.
- [91] C. Poelma, J. Westerweel, and G. Ooms. Turbulence statistics from optical whole-field measurements in particle-laden turbulence. *Experiments in Fluids*, 40(3):347–363, Mar 2006. ISSN 1432-1114. doi: 10.1007/s00348-005-0072-y.
- [92] Lichuan Gui, Ralph Lindken, and Wolfgang Merzkirch. Phase-separated piv measurements of the flow around systems of bubbles rising in water. In *ASME FEDSM*, volume 97, pages 22–26. Citeseer, 1997.
- [93] KT Kiger and C Pan. Piv technique for the simultaneous measurement of dilute two-phase flows. *Journal of fluids engineering*, 122(4):811–818, 2000.
- [94] E. Delnoij, J. Westerweel, N.G. Deen, J.A.M. Kuipers, and W.P.M. van Swaaij. Ensemble correlation piv applied to bubble plumes rising in a bubble column. *Chemical Engineering Science*, 54(21):5159 – 5171, 1999. ISSN 0009-2509. doi: [https://doi.org/10.1016/S0009-2509\(99\)00233-X](https://doi.org/10.1016/S0009-2509(99)00233-X).

- [95] Niels G Deen, Jerry Westerweel, and Erik Delnoij. Two-phase piv in bubbly flows: Status and trends. *Chemical engineering & technology*, 25(1):97–101, 2002.
- [96] Dong-Guan Seol and Scott A. Socolofsky. Vector post-processing algorithm for phase discrimination of two-phase piv. *Experiments in Fluids*, 45(2):223–239, Aug 2008. ISSN 1432-1114. doi: 10.1007/s00348-008-0473-9.
- [97] B. Wieneke. Stereo-piv using self-calibration on particle images. *Experiments in Fluids*, 39(2):267–280, Aug 2005. ISSN 1432-1114. doi: 10.1007/s00348-005-0962-z.
- [98] Jan S Ribberink and Abdullah A Al-Salem. Sediment transport in oscillatory boundary layers in cases of rippled beds and sheet flow. *Journal of Geophysical Research: Oceans*, 99(C6):12707–12727, 1994.
- [99] Kiyoshi Horikawa, Akira Watanabe, and Sadakazu Katori. Sediment transport under sheet flow condition. In *Coastal Engineering 1982*, pages 1335–1352. 1982.
- [100] EA Cowen and SG Monismith. A hybrid digital particle tracking velocimetry technique. *Experiments in fluids*, 22(3):199–211, 1997.
- [101] RD Keane, RJa Adrian, and Yuanhui Zhang. Super-resolution particle imaging velocimetry. *Measurement Science and Technology*, 6(6):754, 1995.
- [102] Gianluca Blois, Julio M Barros, and Kenneth T Christensen. A microscopic particle image velocimetry method for studying the dynamics of immiscible liquid–liquid interactions in a porous micromodel. *Microfluidics and Nanofluidics*, 18(5-6):1391–1406, 2015.
- [103] Mehdi Elhimer, Olivier Praud, Moise Marchal, Sébastien Cazin, and Rudy Bazile. Simultaneous piv/ptv velocimetry technique in a turbulent particle-laden flow. *Journal of Visualization*, 20(2):289–304, 2017.
- [104] Yoshimichi Hagiwara, Toru Murata, Mitsuru Tanaka, and Takumi Fukawa. Turbulence modification by the clusters of settling particles in turbulent water flow in a horizontal duct. *Powder technology*, 125(2-3):158–167, 2002.
- [105] R Lindken and W Merzkirch. A novel piv technique for measurements in multiphase flows and its application to two-phase bubbly flows. *Experiments in fluids*, 33(6):814–825, 2002.
- [106] R Lindken and W Merzkirch. Velocity measurements of liquid and gaseous phase for a system of bubbles rising in water. *Experiments in fluids*, 29(1):S194–S201, 2000.

- [107] Xiangqun Song, Liping Shen, Yuichi Murai, and Fujio Yamamoto. Separation of particle-bubble images in multiphase flow. In *International Workshop on PIV'99- Santa Barbara, 3 rd, Santa Barbara, CA*, pages 15–20, 1999.
- [108] Jarmo Ilonen, Roman Juránek, Tuomas Eerola, Lasse Lensu, Markéta Dubská, Pavel Zemčík, and Heikki Kälviäinen. Comparison of bubble detectors and size distribution estimators. *Pattern Recognition Letters*, 101:60–66, 2018.
- [109] Igor Poletaev, Mikhail P Tokarev, and Konstantin S Pervunin. Bubble patterns recognition using neural networks: Application to the analysis of a two-phase bubbly jet. *International Journal of Multiphase Flow*, 126:103194, 2020.
- [110] Xinzhi Xue and Joseph Katz. Formation of compound droplets during fragmentation of turbulent buoyant oil jet in water. *Journal of Fluid Mechanics*, 878:98–112, 2019.
- [111] Bernhard Wieneke. Piv uncertainty quantification from correlation statistics. *Measurement Science and Technology*, 26(7):074002, 2015.
- [112] Andrea Sciacchitano and Bernhard Wieneke. Piv uncertainty propagation. *Measurement Science and Technology*, 27(8):084006, 2016.
- [113] Francisco Pedocchi, J Ezequiel Martin, and Marcelo H García. Inexpensive fluorescent particles for large-scale experiments using particle image velocimetry. *Experiments in Fluids*, 45(1):183–186, 2008.
- [114] Nathan Washuta. *Air entrainment in the turbulent ship hull boundary layer*. PhD thesis, University of Maryland, College Park, 2016.
- [115] Nicholas T Ouellette, PJJ O'Malley, and Jerry P Gollub. Transport of finite-sized particles in chaotic flow. *Physical review letters*, 101(17):174504, 2008.
- [116] Markus Raffel, Christian E Willert, Jürgen Kompenhans, et al. *Particle image velocimetry: a practical guide*, volume 2. Springer, 1998.
- [117] Dirk Hermanus Swart. Offshore sediment transport and equilibrium beach profiles. 1974.
- [118] Ivar G Jonsson and Niels A Carlsen. Experimental and theoretical investigations in an oscillatory turbulent boundary layer. *Journal of Hydraulic Research*, 14(1):45–60, 1976.
- [119] Mariano I Cantero, S Balachandar, and Marcelo H Garcia. An eulerian–eulerian model for gravity currents driven by inertial particles. *International Journal of Multiphase Flow*, 34(5):484–501, 2008.
- [120] JE Dick and John FA Sleath. Velocities and concentrations in oscillatory flow over beds of sediment. *Journal of Fluid Mechanics*, 233:165–196, 1991.

- [121] Lucia J Baker and Filippo Coletti. Particle–fluid–wall interaction of inertial spherical particles in a turbulent boundary layer. *Journal of Fluid Mechanics*, 908, 2021.